Aramid Nanofiber Composites for Energy Storage Applications

by

Siu on Tung

A dissertation submitted in partial fulfillment
of the requirements for the degree of
Doctor of Philosophy
(Macromolecular Science and Engineering)
The University of Michigan
2017

Doctoral Committee:

Professor Nicholas A. Kotov, Co-Chair
Professor Levi T. Thompson, Co-Chair
Professor Mark A. Barteau
Professor Richard Laine

Siu on Tung

situng@umich.edu

ORCID iD: 0000-0003-3998-4185

2017

Dedication

To my mother, I am nothing without you.

To my father, grandfather and grandmother, you'll always be in my heart.

I hope I've made you proud.

Acknowledgements

I would like to thank my advisors Prof. Nick Kotov and Prof. Levi Thompson for believing in my abilities and giving me an opportunity to pursue my PhD studies at University of Michigan. Their support and guidance has better me as a researcher and individual.

I would also like to acknowledge my dissertation committee for their continued support, and the Kotov and Thompson research group. I would like to thank Dr. Peter Ho, Dr. Joonghwan Bahng, Dr. Huanan Zhang, Dr. Bongjun Yeom, Dr. Terry Shyu, Dr. Xingyi Yang, Dr. Krista Hawthorne, Dr, Jon Kucharyson, Dr. Abdul Djire, Dr. Tapiwa Mushove, Sydney Fisher, Jeejay Chen, and Yixuan Chen for their help throughout my PhD. Your comments and thoughtful discussions everyday help shaped my research and dissertation.

I would also like to thank every high school, undergraduate, and master student that has worked with me: Stanley Wang, Hallie Byles, Peter Caintic, Devon Beck, Haowen Chen, Anna Fowler, Soroush Labaf, Samantha Rahmani, Joe Costa, and Cameryn Boyd. Their hard-work, dedication and creativity have helped advance the research in this dissertation.

I am grateful for the support from my funding sources at the National Science Foundation, U.S. Army Tank Automotive Research Development and Engineering Center, and Joint Center for Energy Storage Research.

I also want to thank my family, especially my mother. She has been my rock through the tough years of losing my father, my grandfather and 3 months ago, my grandmother. Her sacrifice and love throughout my life has given me chances to take risks and pursue all that

I love and enjoy. I am forever indebted to you. Finally, I want to thank my longtime girlfriend, Winnie. Only you have kept me sane through these 5 tough years. I love you!

Table of Contents

List of Figures

List of Tables

List of Abbreviations

A	Electrode Area (cm^2)
ACN	Acetonitrile
AEM	Anion Exchange Membrane
ANF	Aramid Nanofiber
CV	Cyclic Voltammetry
D_0	Diffusion Coefficient
DI Water	De-Ionized Water
DMC	Dimethyl Carbonate
DMSO	Dimethyl Sulfoxide
DSC	Differential Scanning Calorimetry
E_{ICM}	Young's Modulus of Ionic Conducting Membrane
EC	Ethylene Carbonate
EIS	Electrochemical Impedance Spectroscopy
EV	Electric Vehicle
F	Faraday's Constant
FTIR	Fourier Transformed Infrared Spectroscopy
G_{ICM}	Shear Modulus of Ionic Conducting Membrane
HEV	Hybrid Electric Vehicle
HF	Hydrofluoric Acid
ICM	Ion Conducting Membrane
IEM	Ion Exchange Membrane
KOH	Potassium Hydroxide
LBL	Layer-by-layer
LIB	Lithium Ion Battery
$LiPF_6$	Lithium Hexafluorophosphate

LMPB	Lithium Metal Polymer Battery
MIP	Mercury Intrusion Porosimetry
n	Number of Electron Transferred
NAqRFB	Non-Aqueous Redox Flow Battery
NMP	N-Methyl-2-pyrrolidone
PC	Propylene Carbonate
PDDA	Polydiallyldimethylammonium Chloride
PE	Polyethylene
PEO	Polyethylene Oxide
PIM	Polymer with Intrinsic Porosity
PP	Polypropylene
PSS	Polystyrene Sulfonate
PTFE	Polytetrafluoroethylene
PVdF	Polyvinylidene Fluoride
RFB	Redox Flow Battery
SEM	Scanning Electron Microscopy
SOC	State Of Charge
SWV	Square Wave Voltammetry
$TBABF_4$	Tetrabutylammonium Tetrafluoroborate
$TEABF_4$	Tetraethylammonium Tetrafluoroborate
TEM	Transmission Electron Microscopy
TGA	Thermal Gravimetric Analysis
t_p	Pulse Width in Square Wave Voltammetry
TPD	Temperature Programmed Desorption
$V(acac)_3$	Vanadium Acetylacetonate
$VO(acac)_2$	Vanadyl Acetylacetonate
XRD	X-Ray Diffraction
Δi_p	Peak Current
Ω_{ICM}	Resistance of Ionic Conducting Membrane

Abstract

Lithium ion batteries and non-aqueous redox flow batteries represent two of the most important energy storage technologies to efficient electric vehicles and power grid, which are essential to decreasing U.S. dependence on fossil fuel and sustainable economic growth. Many of the developmental roadblocks for these batteries are related to the separator, an electrically insulating layer between the cathode and anode. Lithium dendrite growth has limited the performance and threatened the safety of lithium ion batteries by piercing the separator and causing internal shorts. In non-aqueous redox flow batteries, active material crossover through microporous separators and the general lack of a suitable ion conducting membrane has led to low operating efficiencies and rapid capacity fade. Developing new separators for these batteries involve the combination of different and sometimes seemingly contradictory properties, such as high ionic conductivity, mechanical stability, thermal stability, chemical stability, and selective permeability. In this dissertation, I present work on composites made from Kevlar-drived aramid nanofibers (ANF) through rational design and fabrication techniques. For lithium ion batteries, a dendrite suppressing layer-by-layer composite of ANF and polyethylene oxide is present with goals of high ionic conductivity, improved safety and thermal stability. For non-aqueous redox flow batteries, a nanoporous ANF separator with surface polyelectrolyte modification is used to achieve high coulombic efficiencies and cycle life in practical flow cells. Finally, manufacturability of ANF based separators is addressed through a prototype machine for continuous ANF separator production and a novel separator coated on anode

assembly. In combination, these studies serve as a foundation for addressing the challenges in separator engineering for lithium ion batteries and redox flow batteries.

Chapter 1

Introduction

1.1 Energy Storage Overview

The EPA has reported that by 2100, if global action is taken, we can avoid an estimated 12,000 deaths annually associated with extreme temperatures in 49 major U.S. cities, the loss of 7.9M U.S. acres lost to wildfires, and $11B U.S. agricultural losses, among other damages, all associated with global climate change.[1] Increases in energy efficiency and decrease of U.S. dependence on fossil fuels are essential for sustainable economic growth of this country and reduction of greenhouse gas emissions worldwide. In line with these concerns, there has been a strong interest to reduce greenhouse gas emissions, to reduce U.S. dependence on fossil fuels, and to increase energy efficiency. Electrochemical energy storage is a promising solution towards these goals through its application in grid integration of renewable energy sources and the benefits of electric vehicle adoption.

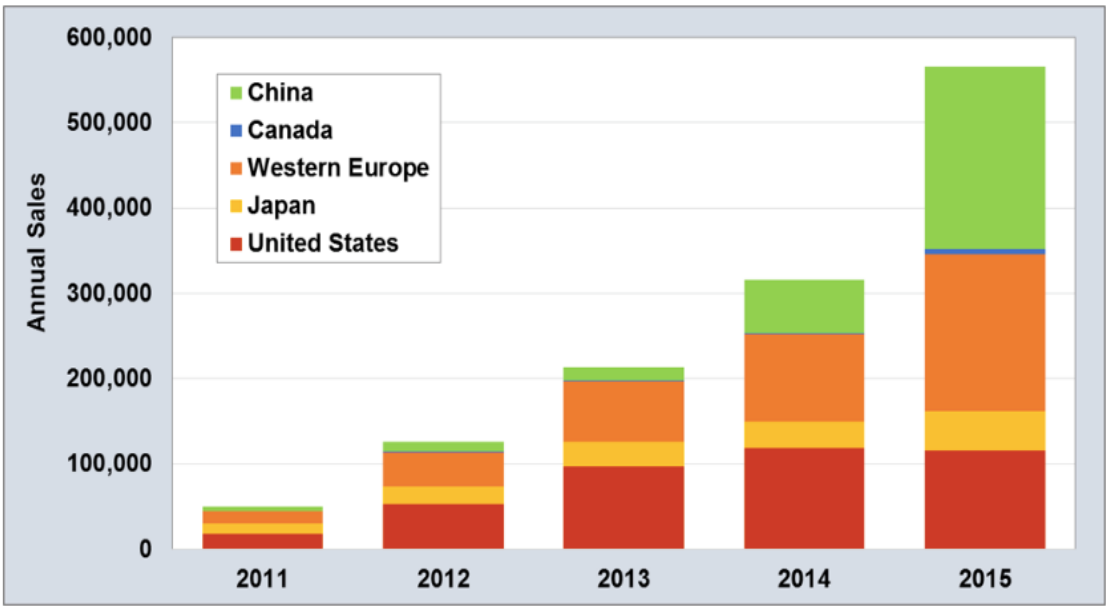

Figure 1-1 Global plug-in light vehicles sales. [2]

In 2013, the transportation sector accounted for 28% of the total primary energy (natural gas, coal, gasoline etc.) consumption while 39% was used for energy generation.[3] Electric vehicles (EVs) and hybrid electric vehicles (HEVs) represent a more efficient approach to transportation with the use of lithium-ion batteries (LIB) instead of traditional, less efficient gasoline/diesel engines.[4] In recent years, the sale of EVs and HEVs are shown exponential growth, pointing to the start of wider acceptance and the adoption by the consumers. (Figure 1-1) On the other hand, grid scale energy storage can enable load-leveling for more efficient operation of power plants (Figure 1-2) and better implementation of intermittent renewable sources such as solar, wind and tidal power.[5] While LIBs are an excellent option for automotive applications thanks to their high energy density and efficiency, their cost is too high for grid scale energy storage.[6] Among the lower cost options, redox flow batteries (RFBs) have attracted much attention because of their long lifetimes and decoupled energy/power density.

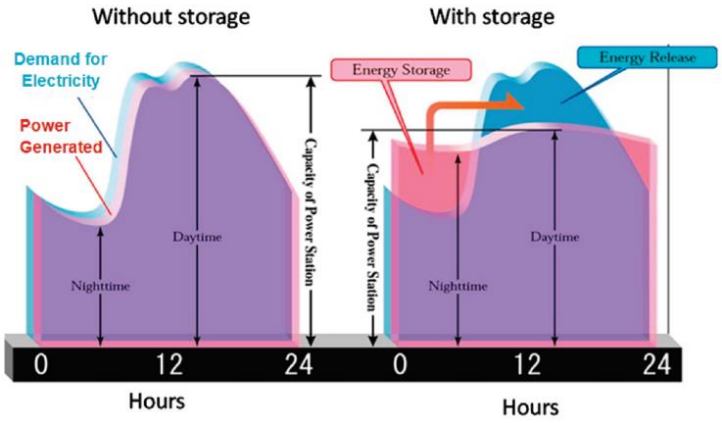

Figure 1-2 Schematic of balancing generation and demand via load leveling[5]

While both LIBs and RFBs consist of the same four basic components (cathode, separator, electrolytes and anode) of a battery, their developmental challenges are markedly different. One of the major differences between LIBs and RFBs is in where and how energy is stored. In LIBs, energy is stored in solids such as lithium metal oxides, lithium metal, and carbon.[7] On the other hand, in RFBs, energy is stored as molecules in solutions that are constantly pumped through porous electrodes.[8] This major difference leads to different material requirements and the design used in these batteries. The follow sections will discuss some of the challenges and current state-of-the-art materials used in both LIBs and RFBs.

1.2 Challenges in Lithium Ion Batteries

Since the commercialization of the lithium ion battery in 1990 by Sony, much effort has been focused on developing new energy dense active materials for cathodes and anodes. The progress on both cathode and anode materials has been impressive when comparing current state of the art materials with those used in Sony's original LIB. High-voltage nickel manganese cobalt oxide cathode materials have shown promise for stable cycling at more than 200mAh/g[9–12] compared to Sony's original cathode material, lithium cobalt

oxide at 155mAh/g.[13] The progress in anode materials has been even more significant in the discovery of silicon anodes with capacities approaching 4000mAh/g[14–16] compared to those of carbon anodes at 400mA/g[7]. However, as we progress towards more energy dense batteries that exceed targets of 750Wh/L and 350Wh/kg[17], battery safety becomes an increasingly important topic.

In a typical LIB, the polyolefin-based separator and liquid electrolyte represent two key components responsible for battery safety. The growth of lithium dendrites from the anode during cycling penetrates the separator and can initialize a thermal runaway event. During thermal runaway, the separator melts at temperatures above 150˚C causing a complete internal short and instantaneous release of the energy stored in the battery. The heat generated from the release of energy along with the flammable liquid electrolyte serving as fuel leads to the eventual battery fire and explosion.[18,19] Therefore, there has been a push for more thermally stable separators[20], and potentially a complete transition to non-flammable solid electrolytes.[21]

Traditional polyolefin separators are used for their low cost and easy processibility[22], however, the low melting point nature of polyolefins such as polypropylene (PP) and polyethylene (PE) makes them prone to catastrophic failure during thermal events. Multi-layer structure PE-PP separators have been proposed and commercialized with a thermal shutdown mechanism. This mechanism is based on the difference in melting point between PP (165˚C) and PE (120-130˚C), where the PE layer will melt and fill the pores of the PP layer and therefore shutting down the battery and hence the thermal runaway event.[23] However, studies have shown battery temperatures during thermal runaway overshoot the

melting point of both PE and PP before the shutdown layer can come into effect, resulting in thermal runaway.[24]

In order to overcome the low melting point nature of the polyolefins, more thermally stable materials such as polytetrafluoroethylene (PTFE), PVDF, polyacrylonitrile and cellulose have been made into fibers for non-woven separators predominantly using techniques such as electrospinning.[20,25–28] Despite being thermally stable, the non-woven separators suffer from large pore sizes and therefore are prone to dendrite penetration. The larger pore sizes in these separators are determined by the diameter of the fibers used, which is in turn limited by electrospinning technique used to fabricate the fibers.[29] It is because of this limitation that many have used to these non-woven separators as scaffolds to form gel polymer membranes, where the ion-conducting gel impregnated inside the large pores would provide some dendrite suppression capability.[30,31] Ceramic nanoparticles such as silica and alumina have also been incorporated into the gels to provide better mechanical strength with the polymer gel domains.[32,33] While these gel polymer electrolytes have improved mechanical strength, the dendrite problem still persists. Another potential solution to this problem lies with solid electrolytes, where the mechanical strength that comes with ceramic based materials is especially attractive.

Solid ceramic electrolytes have long been lithium ion superconductor considered as potential replacements for the liquid electrolytes used in the conventional lithium ion battery.[34,35] Two of the major advantages to ceramic electrolytes are their non-flammability and high strength for dendrite suppression.[4] However, the low ionic conductivity observed under room temperature ($\sim 10^{-6}$ S/cm) and sputtering-based processing technique such as that for LIPON,[36] have limited their use to niche electronics with low power requirements.

More recently, garnet type solid oxide conductors have exhibited ionic conductivity as high as 10^{-3} S/cm, making them promising candidates for the high power applications.[37] However, dendrite suppression capabilities of these solid oxide electrolytes have come into question as dendrite growth through the grain boundaries has been reported.[38,39] Chemically stability against lithium metal has also been reported as a major concern as many have observed irreversible phase changes and loss of conductivity.[34] Last but not least, the brittle nature of any solid ceramic electrolytes remains a question mark on whether they can be processed in conventional roll-to-roll manufacturing and will ultimately determine their wide-spread adoption.

1.3 Challenges in Non-Aqueous Redox Flow Batteries

The proof of concept for a redox flow battery (RFB) was proposed in 1976 by Lawrence Thaller at NASA.[40] However, it was not until recently that RFBs have re-gained interest as a potential grid scale storage solution.[5,6] Commercial demonstration RFB systems have been implemented in Japan and the US in recent years[41,42], with the vanadium/vanadyl based chemistry being the most widely used.[8] While aqueous-based systems present a low cost and relatively environmentally benign grid scale storage solution, there is an ever growing demand for an increased energy density in RFBs. Energy density is a function of the electrons transferred, voltage window and concentration of active species (equation 1). By moving to a non-aqueous solvent, the voltage constraint of 1.23V from the use of water

$$\boldsymbol{E \propto nV_{Cell}C_{Active}} \quad (1)$$

can be removed, thereby increasing the voltage window and thus energy density of RFBs. Voltage windows for organic solvents, such as acetonitrile, have been reported to be close

to 5V which represents a potential four-fold increase in energy density compared to aqueous based systems.[43] Figure 1-3 below compares the voltage window observed for a aqueous vanadium system and that in a non-aqueous vanadium acetylacetonate [V(acac)3] system. The increase from 1.4 to 2.2 V represents a potential 58% increase in energy density given a similar concentration of active material used. [44]

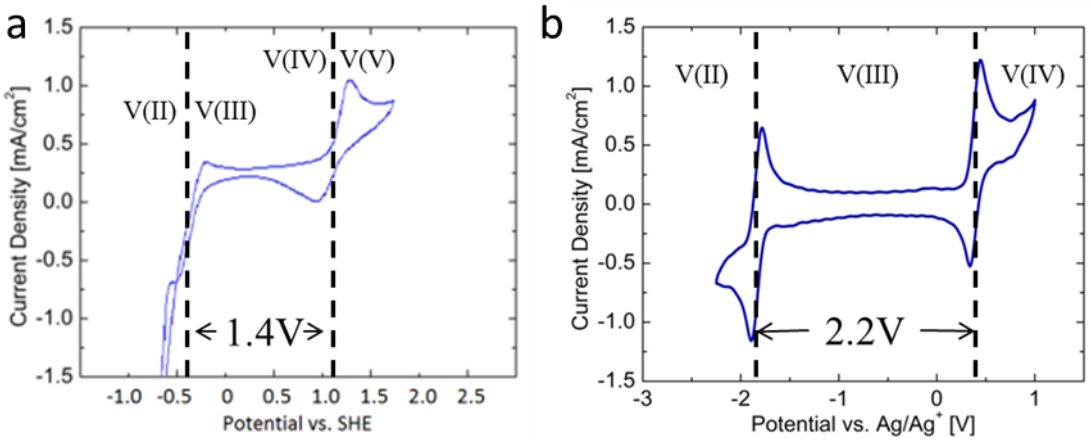

Figure 1-3(a) 0.01M $VOSO_4$ and 2M H_2SO_4 in ultrapure H_2O (b) 0.01M $V(acac)_3$ and 0.1M $TBABF_4$ in acetonitrile.[44]

Despite the promise of non-aqueous RFBs, the transition to organic solvents comes with a complication of challenges such as limited solubility of active materials, instability of active materials and ion conducting membrane, and active material crossover. These challenges directly affect the energy density, longevity and operating efficiency of RFBs and have to sufficiently address before an operation non-aqueous RFB can be achieved.

Among the active materials considered, metal coordinated complexes (MCCs), with acetylacetonate ligand based MCCs in particular, are one of the most studied classes of materials. Vanadium acetylacetonate, among the many possible metal centers, has stood out as the most promising compound due to its two well separated and reversible redox

reactions observed with cyclic voltammetry.[45] However, rapid degradation observed during $V(acac)_3$ charge/discharge experiments has cast doubt on the perceived reversibility on these redox reactions.[46] The limited solubility of $V(acac)_3$ at 0.6M has also made it hard to compete with its aqueous counterpart, V/VO_2 at 2.5M.[47] In response to this limited solubility, Suttil et al. conducted a systematic study on modifying the acetylacetonate ligand that resulted in 450% enhancement in solubility.[48] Furthermore, many also viewed the ligand as charge storing opportunity in addition to the metal center and proceeded to develop non-innocent ligands that exhibited multi-electron transfer capabilities.[49,50] These innovations have continued to make a competitive case for MCC-based RFBs, however, many researchers have raised concerns over the high molecular weight (>300g/mol) of MCCs and questioned their theoretical energy density limits.

More recently, a focus on developing low molecular weight organic materials has gained momentum out of concern for the higher molecular weight of MCCs. Some of the initial organic materials investigated were TEMPO based materials[51,52], where its stable nitroxyl radical has used for a wide range of applications.[53–56] Materials originally designed as stable redox shuttles for lithium ion batteries overcharge protection, such as 1,4 dimethoxy benzene and its derivatives, have also been extensively investigated for its use in non-aqueous RFBs. [57–61] Additionally, design strategies for these novel organic active materials has also been evolving and leveraging the capabilities of DFT simulation. [62,63]

The emerging focus on lower molecular weight materials has in turn highlighted another challenge in the non-aqueous RFB development: active material crossover. While crossover was a concern in aqueous redox flow batteries,[64,65] the complete lack of a suitable membrane for non-aqueous RFBs is, by contrast, much more glaring concern. Active

material crossover is a process where materials on the catholyte side permeate through the separator and reach the anolyte side, or vice versa. This process can cause self-discharge, low efficiencies, and irreversible capacity fade.[66] Early non-aqueous RFB studies used ion exchange membranes used in aqueous RFBs, such as Nafion and Neosepta AHA. However, these membrane were not designed to function in organic solvents and have exhibited side reactions from material incompatibility[46] and low ionic conductivities.[67] While in recent years, some innovative membrane solutions have been reported for non-aqueous RFBs[68,69], the glaring need to prevent active material crossover and novel membrane materials remains.

1.4 Aramid Nanofibers

Aramid nanofibers were recently reported by Ming et al. in 2011[70] and are unique in several ways as a polymeric nanoscale building blocks including nanometer scale fiber diameter, high strength and high thermal stability.

Many polymeric nanofibers have been reported previously and are typically produced by electrospinning,[71] drawing,[72] template synthesis,[73] phase separation[74] and self-assembly[75]. Electrospinning is likely the most widely used production method due to the simplicity of the setup and overall fiber uniformity. However, as elucidated in section 1.2, electrospinning, along with most other methods (drawing, template synthesis etc.) is limited to producing fiber diameters from tens of nanometers to tens of micrometers. This limitation also applies to the pore sizes in the solid nanofiber mats formed using these nanofibers. While these size scales are appropriate for many applications, many of the battery challenges such as dendrite suppression and crossover prevention can benefit from fiber diameters of a few nanometers.

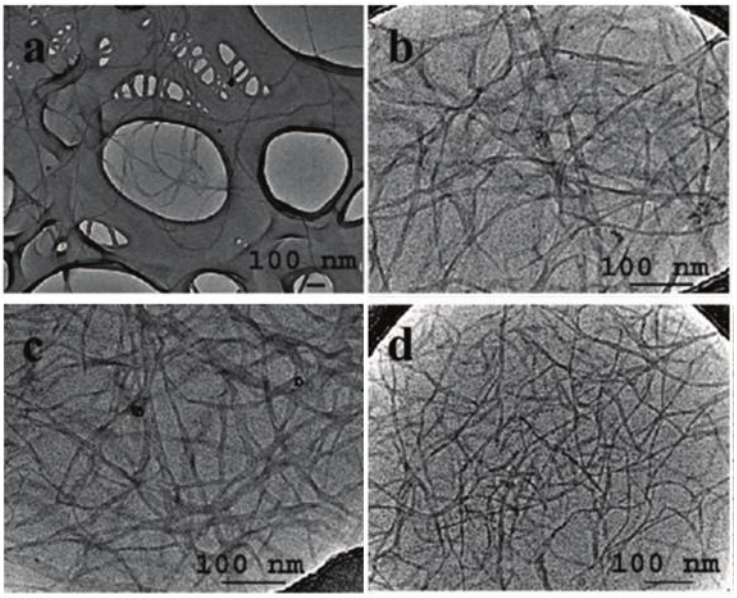

Figure 1-4 TEM images of ANFs in DMSO solution with different water to DMSO volume ratios: (a) 0, (b) 1/200, (c) 1/100, and (d) 1/40. [70]

Aramid nanofibers are formed from the controlled dissolution of standard macroscale aramid polymer known as Kevlar^{TM}. These nanofibers have exhibited fibers diameters as small as 3nm (figure 3), a size range normally reserved for carbon nanotubes (CNT). Layer-by-layer composites made from these fibers also exhibit high mechanical strength and thermal stability, which are attractive properties for applications in energy storage. Additionally, the insulating nature of aramid nanofibers is unique compared to the CNT materials available at this fiber diameter. Considering the properties listed above, aramid nanofibers stands out as novel nanoscale building block for developing composite separators/membrane for LIBs and RFBs.

1.5 Research Goals and Thesis Layout

The overall goal of the research presented in this dissertation is to investigate the potential of aramid nanofibers in energy storage applications and to develop design strategies to

address the challenges in separator/membranes engineering. Three main separator/membrane based objectives are central to this research:

1. Develop a dendrite suppression composite material using aramid nanofibers for safer and more efficient lithium ion batteries
2. Develop a separator/membrane using aramid nanofibers that lowers active material crossover for efficient and long lasting non-aqueous redox flow batteries
3. Demonstrate the manufacturability and scalability of aramid nanofiber based composites for energy storage applications

This dissertation is divided into six chapters as outlined below:

Chapter 1: Introduction

The motivation and application of energy storage is discussed. The current state-of-the-art and developmental challenges for lithium ion battery and redox flow battery separators/membrane are also presented.

Chapter 2: Dendrite Suppressing Composite Ion Conductor from Aramid Nanofibers

Dendrite growth threatens the safety of batteries by piercing the ion-transporting separators between the cathode and anode. Finding a dendrite-suppressing material that combines high modulus and high ionic conductance has long been considered a major technological and materials science challenge. Here we demonstrate that these properties can be attained in a composite made from Kevlar-derived aramid nanofibers assembled in a layer-by-layer manner with poly(ethylene oxide). Successful suppression of hard copper dendrites by the composite ion conductor at extreme discharge conditions is demonstrated, thereby providing an innovative approach for the materials engineering of solid ion conductors.

Chapter 3: Nanoporous Aramid Nanofiber Separators for Redox Flow Batteries

Active material crossover through separator/membranes is a major roadblock to more efficient and longer lasting redox flow batteries. This challenge is especially relevant for non-aqueous redox flow batteries where there is a complete lack of suitable membranes. This chapter investigates the application of a nanoporous aramid nanofiber separator fabricated using a spin-assisted layer-by-layer method. Separation of the active material is based on size selectivity through the nano-sized pores, which promises higher ionic conductivity than ion conducting membranes based on charge selectivity. A layer-by-layer surface coating is also reported that enhances material separation with minimal impact on ionic conductivity.

Chapter 4: High Performance Pillared Vanadium Oxide Cathode for Lithium Ion Batteries

Layered oxides, such as lithium cobalt oxide, are commonly used as cathode materials in lithium ion batteries, however repeated lithium insertion and extraction can cause stress and mechanical fracture, leading to capacity fade. In this chapter, the chemical intercalation of pillaring agents (e.g., Al_{13} Keggin ions) between layers in V_2O_5 xerogels is reported. The hypothesis driving this research is that the pillars will stabilize the crystal structure, reduce strain-induced fracture and improve the high rate capacity and cycle life performance. The electrochemical, thermal, and mechanical properties of unpillared and pillared vanadium oxide materials are compared.

Chapter 5: Scale Up of ANF Separators for Lithium Ion Batteries

Manufacturability of the dendrite-asuppressing ANF separator is a key factor in achieve meaningful impact on lithium ion battery safety. However, the layer-by-layer method reported in chapter 2 is not conducive to scale-up efforts ands typical roll-to-roll manufacture methods in industry. The doctor blading method is investigated as possible scale-up method for fabricating continuous rolls ANF separators. Challenges and strategies to attain high porosity and battery performances with ANF separators are discussed. A prototype continuous coating machine is designed and fabricated to demonstrate the scale-up potential of the doctor blading process.

Chapter 6: Conclusion and Future Work

This chapter summarizes key findings from the research and identifies the major impact made for the energy storage landscape. The limitations of the research will be discussed. Based on the limitations, future research directions are also suggested.

References

1. Sutter, J. D. EPA boss: Climate change could kill thousands. *CNN* (2015).
2. Deparment of Energy. Office of Energy Efficiency and Renewable Energy. (2017). Available at: www.energy.gov.
3. Energy Information Administration. *Annual Energy Review*. (2014).
4. Armand, M. & Tarascon, J. M. Building better batteries. *Nature* **451,** 652–657 (2008).
5. Yang, Z. *et al.* Electrochemical Energy Storage for Green Grid. *Chemical Reviews* **111,** 3577–3613 (2011).
6. Dunn, B., Kamath, H. & Tarascon, J. M. Electrical energy storage for the grid: a battery of choices. *Science* **334,** 928–35 (2011).
7. Tarascon, J. M. & Armand, M. Issues and challenges facing rechargeable lithium batteries. *Nature* **414,** 359–367 (2001).
8. Weber, A. Z. *et al.* Redox flow batteries: A review. *Journal of Applied Electrochemistry* **41,** 1137–1164 (2011).
9. Mohanty, D. *et al.* Modification of Ni-Rich FCG NMC and NCA Cathodes by Atomic Layer Deposition: Preventing Surface Phase Transitions for High-Voltage Lithium-Ion Batteries. *Scientific reports* **6,** 26532 (2016).
10. Liang, C. *et al.* Unraveling the Origin of Instability in Ni-Rich $LiNi_{1-2x}C_{ox}M_{nx}O_2$ (NCM) Cathode Materials. *The Journal of Physical Chemistry C* **120,** 6383–6393 (2016).
11. Lin, F. *et al.* Metal segregation in hierarchically structured cathode materials for high-energy lithium batteries. *Nature Energy* **1,** 15004 (2016).

12. Hu, M., Pang, X. & Zhou, Z. Recent progress in high-voltage lithium ion batteries. *Journal of Power Sources* **237,** 229–242 (2013).

13. Whittingham, M. S. Lithium Batteries and Cathode Materials. *Chemical Reviews* **104,** 4271–4302 (2004).

14. Li, Y. *et al.* Growth of conformal graphene cages on micrometre-sized silicon particles as stable battery anodes. *Nature Energy* **1,** 15029 (2016).

15. Hayner, C. M., Zhao, X. & Kung, H. H. Materials for Rechargeable Lithium-Ion Batteries. *Annual Review of Chemical and Biomolecular Engineering* **3,** 445–471 (2012).

16. Chan, C. K. *et al.* High-performance lithium battery anodes using silicon nanowires. *Nature Nanotechnology* **3,** 31–35 (2008).

17. Howell, D., Cunningham, B., Duong, T. & Faguy, P. *Overview of the DOE VTO Advanced Battery R&D Program*. (2016).

18. Wang, Q. *et al.* Thermal runaway caused fire and explosion of lithium ion battery. *Journal of Power Sources* **208,** 210–224 (2012).

19. Jhu, C. Y., Wang, Y. W., Shu, C. M., Chang, J. C. & Wu, H. C. Thermal explosion hazards on 18650 lithium ion batteries with a VSP2 adiabatic calorimeter. *Journal of Hazardous Materials* **192,** 99–107 (2011).

20. Zhang, S. S. A review on the separators of liquid electrolyte Li-ion batteries. *Journal of Power Sources* **164,** 351–364 (2007).

21. Minami, T., Hayashi, A. & Tatsumisago, M. Recent progress of glass and glass-ceramics as solid electrolytes for lithium secondary batteries. *Solid State Ionics* **177,** 2715–2720 (2006).

22. Arora, P. & Zhang, Z. J. Battery separators. *Chemical reviews* **104,** 4419–62 (2004).

23. Balakrishnan, P. G., Ramesh, R. & Prem Kumar, T. Safety mechanisms in lithium-ion batteries. *Journal of Power Sources* **155,** 401–414 (2006).

24. Roth, E. P., Doughty, D. H. & Pile, D. L. Effects of separator breakdown on abuse response of 18650 Li-ion cells. *Journal of Power Sources* **174,** 579–583 (2007).

25. Lee, H. *et al.* A review of recent developments in membrane separators for rechargeable lithium-ion batteries. *Energy & Environmental Science* **7,** 3857–3886 (2014).

26. Lin, J., Ding, B., Yu, J. & Hsieh, Y. Direct Fabrication of Highly Nanoporous Polystyrene Fibers via Electrospinning. *ACS applied materials & interfaces* **2,** 521–528 (2010).

27. Zhang, J. *et al.* Renewable and superior thermal-resistant cellulose-based composite nonwoven as lithium-ion battery separator. *ACS applied materials & interfaces* **5,** 128–34 (2013).

28. Cho, T.-H. *et al.* Battery performances and thermal stability of polyacrylonitrile nano-fiber-based nonwoven separators for Li-ion battery. *Journal of Power Sources* **181,** 155–160 (2008).

29. Huang, X. Separator technologies for lithium-ion batteries. *Journal of Solid State Electrochemistry* **15,** 649–662 (2011).

30. Cheng, C. L., Wan, C. C. & Wang, Y. Y. Microporous PVdF-HFP based gel polymer electrolytes reinforced by PEGDMA network. *Electrochemistry Communications* **6,** 531–535 (2004).

31. Zhao, J. *et al.* A sustainable and rigid-flexible coupling cellulose-supported

poly(propylene carbonate) polymer electrolyte towards 5V high voltage lithium batteries. *Electrochimica Acta* **188,** 23–30 (2016).

32. Kim, S. H., Choi, K. H., Cho, S. J., Kil, E. H. & Lee, S. Y. Mechanically compliant and lithium dendrite growth-suppressing composite polymer electrolytes for flexible lithium-ion batteries. *Journal of Materials Chemistry A* **1,** 4949 (2013).

33. Gayet, F. *et al.* Unique Combination of Mechanical Strength, Thermal Stability, and High Ion Conduction in PMMA−Silica Nanocomposites Containing High Loadings of Ionic Liquid. *Chemistry of Materials* **21,** 5575–5577 (2009).

34. Thangadurai, V. & Weppner, W. Recent progress in solid oxide and lithium ion conducting electrolytes research. *Ionics* **12,** 81–92 (2006).

35. Knauth, P. Inorganic solid Li ion conductors: An overview. *Solid State Ionics* **180,** 911–916 (2009).

36. Hamon, Y. *et al.* Influence of sputtering conditions on ionic conductivity of LiPON thin films. *Solid State Ionics* **177,** 257–261 (2006).

37. Thangadurai, V., Narayanan, S. & Pinzaru, D. Garnet-type solid-state fast Li ion conductors for Li batteries: critical review. *Chemical Society Reviews* **43,** 4714 (2014).

38. Ren, Y., Shen, Y., Lin, Y. & Nan, C.W. Direct observation of lithium dendrites inside garnet-type lithium-ion solid electrolyte. *Electrochemistry Communications* **57,** 27–30 (2015).

39. Sudo, R. *et al.* Interface behavior between garnet-type lithium-conducting solid electrolyte and lithium metal. *Solid State Ionics* **262,** 151–154 (2014).

40. Thaller, H. L. Electrically Rechargeable Redox Flow Cell. (1976).

41. Skyllas-Kazacos, M., Chakrabarti, M. H., Hajimolana, S. A., Mjalli, F. S. & Saleem, M. Progress in Flow Battery Research and Development. *Journal of The Electrochemical Society* **158,** R55–R79 (2011).

42. Doughty, D. H., Butler, P. C., Akhil, A. A., Clark, N. H. & Boyes, J. D. Batteries for Large-Scale Stationary Electrical Energy Storage. *The Electrochemical Society Interface* **19,** 49–53 (2010).

43. Darling, R. M., Gallagher, K. G., Kowalski, J. A., Ha, S. & Brushett, F. R. Pathways to low-cost electrochemical energy storage: a comparison of aqueous and nonaqueous flow batteries. *Energy & Environmental Science* **7,** 3459–3477 (2014).

44. Shinkle, A. A. Non-Aqueous Single-Metal Redox Flow Batteries. (University of Michigan, Ann Arbor, 2013).

45. Liu, Q., Sleightholme, A. E. S., Shinkle, A. A., Li, Y. & Thompson, L. T. Non-aqueous vanadium acetylacetonate electrolyte for redox flow batteries. *Electrochemistry Communications* **11,** 2312–2315 (2009).

46. Shinkle, A. A., Sleightholme, A. E. S., Griffith, L. D., Thompson, L. T. & Monroe, C. W. Degradation mechanisms in the non-aqueous vanadium acetylacetonate redox flow battery. *Journal of Power Sources* **206,** 490–496 (2012).

47. Li, L. *et al.* A Stable Vanadium Redox-Flow Battery with High Energy Density for Large-Scale Energy Storage. *Advanced Energy Materials* **1,** 394–400 (2011).

48. Suttil, J. A. *et al.* Metal acetylacetonate complexes for high energy density non-aqueous redox flow batteries. *Journal of Materials Chemistry A* **3,** 7929–7938 (2015).

49. Cabrera, P. J. *et al.* Complexes Containing Redox Noninnocent Ligands for

Symmetric, Multielectron Transfer Nonaqueous Redox Flow Batteries. *The Journal of Physical Chemistry C* **119,** 15882–15889 (2015).

50. Cappillino, P. J. *et al.* Application of Redox Non-Innocent Ligands to Non-Aqueous Flow Battery Electrolytes. *Advanced Energy Materials* **4,** 1300566 (2014).

51. Wei, X. *et al.* TEMPO-Based Catholyte for High-Energy Density Nonaqueous Redox Flow Batteries. *Advanced Materials* **26,** 7649–7653 (2014).

52. Milshtein, J. D., Barton, J. L., Darling, R. M. & Brushett, F. R. 4-acetamido-2,2,6,6-tetramethylpiperidine-1-oxyl as a model organic redox active compound for nonaqueous flow batteries. *Journal of Power Sources* **327,** 151–159 (2016).

53. Liu, S. *et al.* TEMPO Functionalized Polymers: Synthesis and Applications. *Current Organic Chemistry* **20,** 1389–1403 (2016).

54. Abdellaoui, S., Knoche, K. L., Lim, K., Hickey, D. P. & Minteer, S. D. TEMPO as a Promising Electrocatalyst for the Electrochemical Oxidation of Hydrogen Peroxide in Bioelectronic Applications. *Journal of The Electrochemical Society* **163,** H3001–H3005 (2016).

55. Hickey, D. P. *et al.* Predicting Electrocatalytic Properties: Modeling Structure-Activity Relationships of Nitroxyl Radicals. *Journal of the American Chemical Society* **137,** 16179–86 (2015).

56. Nakahara, K., Oyaizu, K. & Nishide, H. Organic Radical Battery Approaching Practical Use. *Chemistry Letters* **40,** 222–227 (2011).

57. Brushett, F. R., Vaughey, J. T. & Jansen, A. N. An All-Organic Non-aqueous Lithium-Ion Redox Flow Battery. *Advanced Energy Materials* **2,** 1390–1396 (2012).

58. Kowalski, J. A., Su, L., Milshtein, J. D. & Brushett, F. R. Recent advances in

molecular engineering of redox active organic molecules for nonaqueous flow batteries. *Current Opinion in Chemical Engineering* **13,** 45–52 (2016).

59. Huang, J. *et al.* A subtractive approach to molecular engineering of dimethoxybenzene-based redox materials for non-aqueous flow batteries. *J. Mater. Chem. A* **3,** 14971–14976 (2015).

60. Kaur, A. P., Holubowitch, N. E., Ergun, S., Elliott, C. F. & Odom, S. A. A Highly Soluble Organic Catholyte for Non-Aqueous Redox Flow Batteries. *Energy Technology* **3,** 476–480 (2015).

61. Assary, R. S., Zhang, L., Huang, J. & Curtiss, L. A. Molecular Level Understanding of the Factors Affecting the Stability of Dimethoxy Benzene Catholyte Candidates From First Principles Investigations. *The Journal of Physical Chemistry C* (2016).

62. Sevov, C. S. *et al.* Evolutionary Design of Low Molecular Weight Organic Anolyte Materials for Applications in Nonaqueous Redox Flow Batteries. *Journal of the American Chemical Society* **137,** 14465–14472 (2015).

63. Sevov, C. S. *et al.* Physical Organic Approach to Persistent, Cyclable, Low-Potential Electrolytes for Flow Battery Applications. *Journal of the American Chemical Society* **139,** 2924–2927 (2017).

64. Luo, Q., Zhang, H., Chen, J., Qian, P. & Zhai, Y. Modification of Nafion membrane using interfacial polymerization for vanadium redox flow battery applications. *Journal of Membrane Science* **311,** 98–103 (2008).

65. Gu, S., Gong, K., Yan, E. Z. & Yan, Y. A multiple ion-exchange membrane design for redox flow batteries. *Energy & Environmental Science* **7,** 2986 (2014).

66. Shin, S. H., Yun, S. H. & Moon, S. H. A review of current developments in non-

aqueous redox flow batteries: characterization of their membranes for design perspective. *RSC Advances* **3,** 9095 (2013).

67. Su, L. *et al.* An Investigation of the Ionic Conductivity and Species Crossover of Lithiated Nafion 117 in Nonaqueous Electrolytes. *Journal of The Electrochemical Society* **163,** A5253–A5262 (2016).

68. Li, C. *et al.* Polysulfide-Blocking Microporous Polymer Membrane Tailored for Hybrid Li-Sulfur Flow Batteries. *Nano letters* **15,** 5724–5729 (2015).

69. Cho, E. & Won, J. Novel composite membrane coated with a poly(diallyldimethylammonium chloride)/urushi semi-interpenetrating polymer network for non-aqueous redox flow battery application. *Journal of Power Sources* **335,** 12–19 (2016).

70. Yang, M. *et al.* Dispersions of Aramid Nanofibers: A New Nanoscale Building Block. *ACS Nano* **5,** 6945–6954 (2011).

71. Greiner, A. & Wendorff, J. H. Electrospinning: A Fascinating Method for the Preparation of Ultrathin Fibers. *Angewandte Chemie International Edition* **46,** 5670–5703 (2007).

72. Ondarcuhu, T. & Joachim, C. Drawing a single nanofibre over hundreds of microns. *Europhysics Letters* **42,** 215–220 (1998).

73. Feng, L. *et al.* Super-Hydrophobic Surface of Aligned Polyacrylonitrile Nanofibers. *Angewandte Chemie* **114,** 1269–1271 (2002).

74. Zhang, R. & Ma, P. X. Poly(alpha-hydroxyl acids)/hydroxyapatite porous composites for bone-tissue engineering. I. Preparation and morphology. *Journal of biomedical materials research* **44,** 446–55 (1999).

75. Hartgerink, J. D. Self-Assembly and Mineralization of Peptide-Amphiphile Nanofibers. *Science* **294,** 1684–1688 (2001).

Chapter 2

Dendrite Suppressing Composite Ion Conductor from Aramid Nanofibers

2.1 Background and Approach

Increasing the capacity and discharge rate of batteries represents the key bottleneck preventing the full realization of many technologies, such as electrical vehicles, solar/wind energy conversion, flexible electronics, and health monitoring devices. Much attention had been paid to maximizing the energy and power densities of cathodes and anodes of lithium batteries,[1,2] especially using new forms of nanostructured materials[3,4] and thin polymer films.[4]Although many problems related to the stability of cathodes and anodes remain to be resolved, more attention needs to be paid to the ion-conducting membranes (ICMs) separating them. These membranes represent an equally crucial part of high capacity and high discharge rate batteries. The ICM is the key component responsible for safe operation of lithium ion and other batteries, which have been known to cause accidents in the past. Current ICMs are typically made from microporous polymer sheets impregnated with solutions of lithium salts in alkylcarbonates. These gel or liquid phases serve as the ion-conducting media enabling transport of ions but preventing transport of electrons between the electrodes. Shortcomings of such ICMs include flammability, fluid leakage, limited range in operating temperatures, and sporadic internal shorting leading to battery fires. Materials adequately addressing these shortcomings are difficult to find because the

properties required of ICMs impose seemingly contradictory requirements on the atomic structure of the ICM material. While lithium (or other) ions need to have high mobility to enable high ion conductivity (Ω_{ICM}), the remaining atomic framework needs to be rigid to give ICMs high stiffness (E_{ICM}) and shear modulus (G_{ICM}). At the same time, truly safe batteries would require ICMs that are both flexible and tough. However, Ashby plots[5] and other data[6,7] indicate that tolerance to high local strains is difficult to combine with high strength and stiffness[8]; similar incompatibilities also exist with several other combinations of mechanical and transport properties of materials[9]. Moreover, as the charge rate and power density of the batteries increase, the importance of having a reliable insulating barrier between the electrodes also increases dramatically. Besides having adequate mechanical and ion transport properties, we must also considerably improve temperature resilience of current ICMs because high ionic currents will inevitably result in higher energy dissipation in a smaller volume. *De facto* the new ICMs to be paired with new anodes and cathodes must combine the advantages of ion-conducting glasses[10] and polymers[11] in one material. Resolution of these challenges essentially equates to finding new approaches to the materials engineering of ICMs involving new processes to synthesize them as well as novel ICM components.

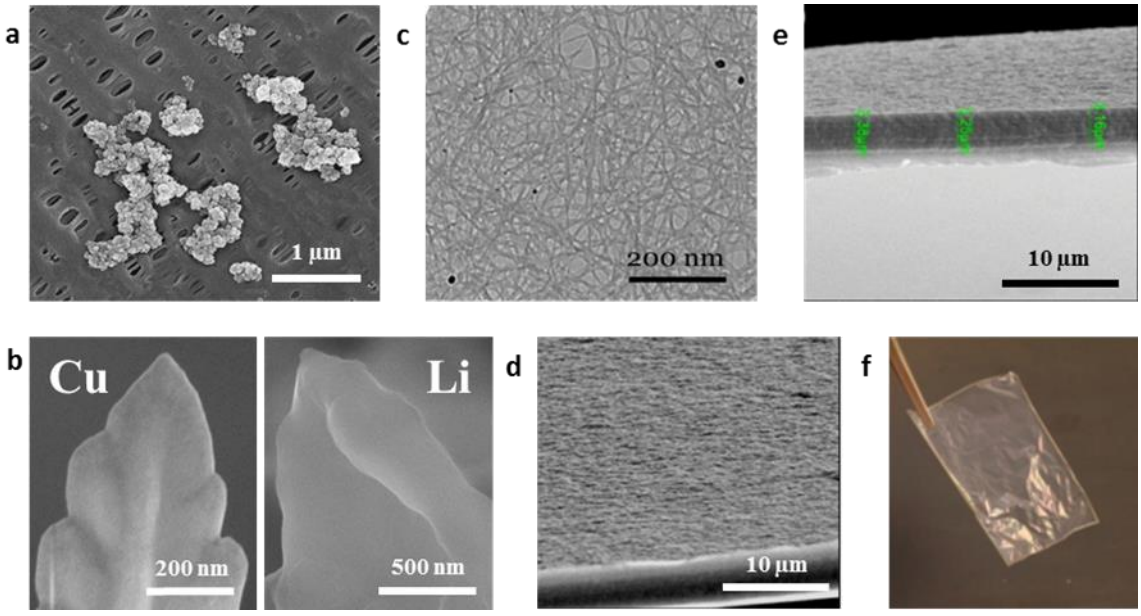

Figure 2-1(a) Top view SEM images of copper dendrite penetrating through CelgardTM ICM. (b) SEM image of the tip of a copper (right) and lithium (left) dendrite. (c) TEM image of ANF. (d) Top and (e) side

The safety problems of modern batteries are mainly related to dendrite growth and anode expansion in their charged state[12–16]. Piercing of porous polymer separators, for instance Celgard^{TM} 2400 (Figure 2-1a), by dendrites (Figure 2-1b) is the most common mechanism of spontaneous battery failure, which can also lead to short circuits and fires.[17] The growth of dendrites is also the key roadblock to develop batteries with lithium metal anodes, which can approach the theoretical limit for lithium-based storage devices with respect to capacity, power, and weight.[18,19]

Many different approaches have been proposed previously to prevent dendrite formation, including additives to the gel and liquid electrolyte or composite gel electrolytes with inorganic fillers,[20] however, the dendrite problem still persists in these cases. The variety of data suggest that improvement of the mechanical properties of the ICM such as E_{ICM} or G_{ICM} could dramatically inhibit their growth.[21] Sufficient compressive stress exerted on dendrite tips is expected to inhibit their growth.[22,23]

Multiple materials combinations and materials engineering approaches have been investigated in the past to make ICMs, but these presented problems of their own, eventually translating into alternative safety concerns and/or energy losses. Solid electrolytes based on Li-based ceramics represent one of the currently most advanced ion conductors available.[10,24,25] They combine high mechanical stiffness (E=80-100 GPa) and high ionic conductivity (Ω_{ICM} from 10^{-3} S/cm [10,24] to 1.2 x 10^{-2} S/cm).[25] These parameters make them exciting candidates for some high-power applications. However, their brittleness, reflecting the fundamental conflict between the two essential materials properties,[6] makes it difficult to incorporate Li-based ceramics into battery packs. Their brittleness also necessitates thicker ICMs with increased internal resistance leading to energy losses. Finding new versatile materials that make dendrite inhibition possible, and systematic studies of their dependence on different mechanical properties, is fundamentally important since dendrite growth is pervasive in virtually all electrochemical devices utilizing a range of metals and electrolytes.

In this chapter, a new composite that combines the key properties required for ICMs and effectively suppresses the growth of dendrites is described. The resulting membranes also exhibit low ohmic resistance and high mechanical flexibility, which are essential for battery safety. As a foundation of the new ICM, we decided to use aramid nanofibers (ANFs), whose preparation was described recently[26]. The macro-scale version of ANFs is Kevlar, one of the paragons of mechanical performance. ANFs with a length of 1 μm and an average diameter of 5-10 nm (Figure 2-1c) were made by dissolution of bulk Kevlar fibers in DMSO in the presence of KOH. Notably, the ANFs are insulating, differentiating them

from many other ultrastrong metallic and semiconducting nanomaterials (nanotubes, nanowires…) that cannot be used for ICMs.

2.2 Material and Methods

This section describes the techniques used in the work.

2.2.1 Preparation of (PEO/ANF)n nanocomposite ion conductors

Multilayers of PEO and ANFs are prepared following the by the classical LBL deposition process[27–31] with exception of the use of dimethyl sulfoxide (DMSO) as solvent for and rinsing solution for assembly steps involving ANFs. Note, at the same time, that the film preparation process used here is markedly different than the one used in the previous study by M. Yang *et al.*[26] by the use of partner electrolyte in ALL the deposition steps while M. Yang *et al.*[26] used ANF-on-ANF deposition.

Glass slides are pre-cleaned by piranha solution (1:4 30% H_2O_2 to 98% H_2SO_4) for 2 hours followed by extensive rinsing with DI water (18 MΩ) immediately prior to the LBL assembly. The glass slides are dipped in solutions of 0.01% PEO in DI water for 1 minute, rinsed in DI water for 1 minute, air dried and then dipped in 0.04% ANF dispersion in DMSO for 10 seconds. The rinsing step after deposition of ANF consisted of DMSO bath for 30 seconds followed by 1 minute rinse in DI water and air drying.

$(PEO/ANF)_n$ LBL composite are detached from glass slides as continuous membranes by immersing the slides in 0.1% HF for <3 minutes. Freestanding membranes are rinsed with DI water until the pH value at the membrane surface becomes neutral (pH 7), and then dried in vacuum oven at 80°C.

2.2.2 Ionic Conductivity Measurements

Free-standing $(PEO/ANF)_n$ membranes were sandwiched between two lithium metal electrodes and housed in a CR2032 coin battery cell. Impedance spectroscopy was taken using Autolab Potentiostat and Solartron 1260 freqency response analyzer. The resulting Nyquist plots are fitted to an equivalent circuit where ionic conductivity is then calculated.

2.2.3 Growth of Copper Dendrites

Smooth copper layers 1 µm thick deposited on silicon wafers by physical vapor deposition are used as working electrodes. LBL membranes are then deposited onto the copper layer using the procedure described in Section 1. The copper-Si wafer electrode is dipped into a 0.15 M copper chloride solution in anhydrous DMSO with 1 cm^2 of submerged surface area (Figure 2-2). 10.3 mA/cm^2 is applied to the electrode with a copper plate used as the counter electrode for 2 seconds. This corresponds to approximately 0.02 $Coulomb/cm^2$ charge transferred. The sample was then rinsed gently with DMSO and dried under vacuum overnight at room temperature. The sample was then sputtered with gold in preparation for SEM. For cross-sectional images, the sample was broken in half to expose a cross section after cooling by liquid nitrogen.

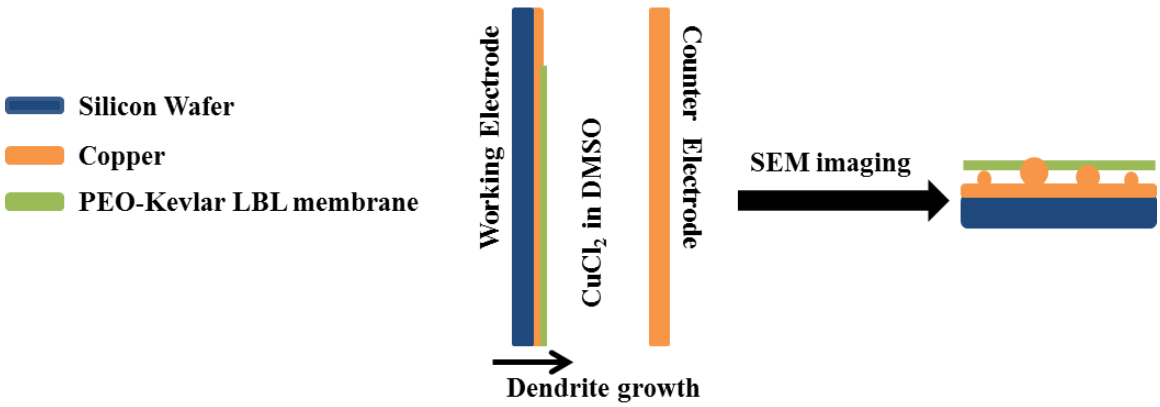

Figure 2-2 Illustration of the experimental setup used in dendrite growth experiments.

2.2.4 Preparation of $(ANF/ANF)_n$ film

The (ANF/ANF)n film used in FTIR experiments was obtained using the procedure describe by M. Yang et al[26]: A clean piece of glass slide was dipped into 1% poly(diallyldimethyammonium chloride) (PDDA) solution for 1 min and rinsed with DI water for 2 mins before air drying. The PDDA coated glass slide was then dipped into the 0.04% ANF dispersion for 1 min and rinsed with water for 2 mins before air drying. This sequence was repeated 100 times to obtain a free-standing $(ANF/ANF)_{100}$ film.

2.2.5 Preparation of $LiCoO_2$ coin cell

A slurry of 88% lithium cobalt oxide ($LiCoO_2$, SigmaAldrich), 6% SuperP Li Carbon, 6% PVdF was made using a planetary mixer and stirred repeatedly during the preparation process. The slurry was then cast onto an aluminum foil substrate using a doctor blade to form an electrode (blade height = 100 µm). The electrodes were dried in a vacuum oven overnight at 110^oC and then punched out using arc hole punch and transferred into an argon-filled glovebox. Mass loading was estimated to be 4.7mg/cm^2, electrode thickness was estimated to be 30µm with electrode density of 1.8g/cm^3. The electrodes were then assembled into standard CR2032 coin cells along with the $(PEO/ANF)_{200}$ electrolyte, 150µL 1M $LiPF_6$ in EC/DMC solution, lithium metal anode, stainless steel spacers and spring washers. For symmetric cells, lithium metal was used as both the cathode and anode. The cells were left in the glovebox overnight before being placed onto a Maccor battery tester for charge-discharge experiments. Cyclic voltammetry was also performed on the coin cells at 0.3mV/s from 3.2V to 4.5V. $LiCoO_2$ and NMP were purchased from Sigma Aldrich, SuperP Li was purchased from Timcal, PVDF was purchased from KYNAR®.

All powders were dried at 110 °C overnight before use, while NMP was dried over a bed of molecular sieves.

2.3 Results

This section describes the evaluation of the properties found in the $(ANF/PEO)_n$ nanocomposites.

2.3.1 Composite fabrication and mechanical properties

ANFs were combined in this work with poly(ethyleneoxide) (PEO) serving as a solid ion-conducting medium using layer-by-layer (LBL) assembly method[32]. In the past, composites made by LBL or other methods have shown exceptional mechanical performance[33] or ionic conductivity[34,35], but not the combination of the two nor any dendrite suppressing capabilities. The ability of LBL to produce thin, uniform, and nearly defect-free films is also of importance. Reduction of ICM thickness is needed to avoid high internal resistance inside the battery cells that leads both to heating, instability of operation, and energy losses.

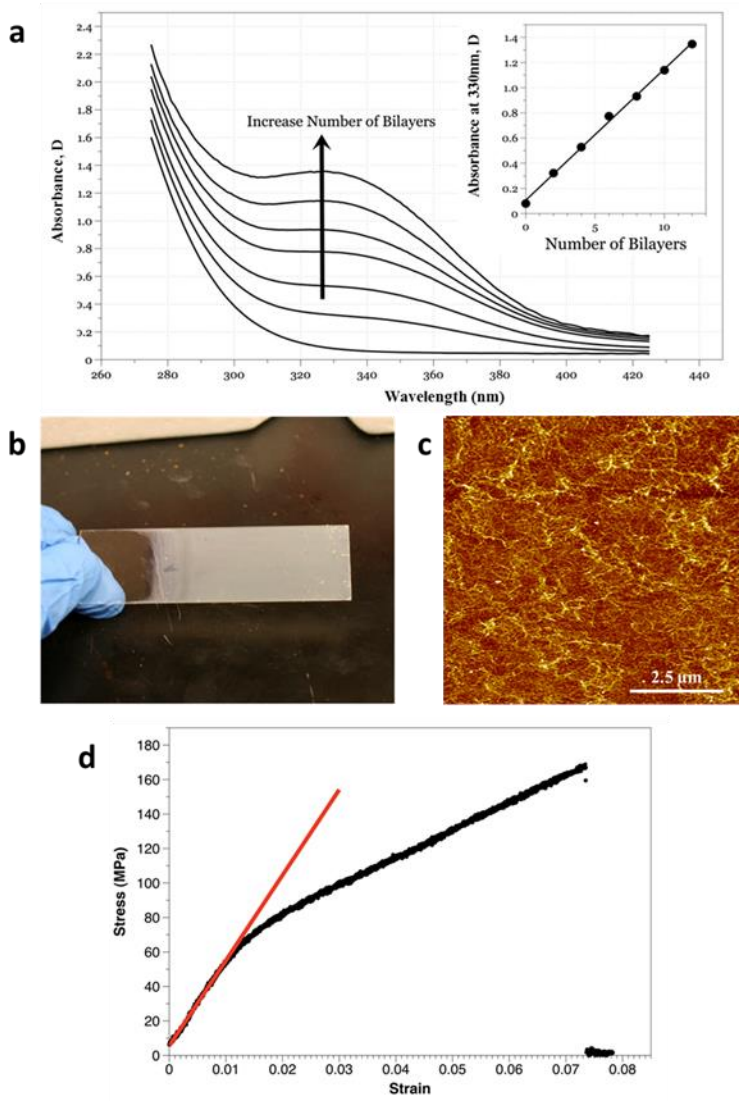

Figure 2-3 (a) UV-Vis spectra of $(PEO/ANF)_n$ LBL composite deposited on glass slide with different number of bilayers. Absorbance at 330 nm shows linear growth of the film; (b) Photograph of $(PEO/ANF)_n$ LBL film on glass slide. (c) AFM image of PEO-ANF nanofiber network. (d) Stress-strain curve of $(PEO/ANF)_{100;}$ ultimate strength is σ_{ICM}=169 MPa. The initial linear region yields Young's Modulus of E=4.95 GPa.

During the LBL process, the steady increase in the absorbance of the material at 330 nm indicates the linear growth of the $(PEO/ANF)_n$ film as the number of LBL deposition cycles, *n*, increases (Figure 2-3a). Free-standing LBL multilayers were obtained by chemical delamination of $(PEO/ANF)_n$ films (Figure 2-3b) after depositing 10-200 bilayers. Their smoothness, transparency, and interference coloration (rainbows) indicated

their uniform thickness and structural homogeneity, which can be also seen in SEM images (Figure 1d-f). AFM images of $(PEO/ANF)_5$ display a dense and uniform interconnecting network of thin nanoscale fibers (Figure 2-3c). Such morphology provides the structural prerequisites for high ion conductance, stiffness, and efficient distribution of local strains. The ultimate tensile strength, Young's modulus, and shear modulus were σ_{ICM} = 170±5 MPa, E_{ICM} = 5.0±0.05 GPa and G_{ICM} = 1.8±0.06 GPa, respectively (Figure 2-3d). Given PEO's value of E_{ICM} = 100 MPa, $(PEO/ANF)_n$ nanocomposites show a *ca.* 500x increase in elastic modulus. Impregnation with lithium triflate (often used in Li batteries as electrolyte) did not change the mechanical properties of the $(PEO/ANF)_{200}$ composite.

2.3.2 Ionic Conductivity

Crystallization of PEO is known to dramatically decrease the ionic conductivity of ICMs made by traditional casting or blending[11,36]. However, in the $(PEO/ANF)_n$ composite we do not observe crystalline phase even though the polymer is deposited at room temperature, with and without lithium triflate, before and after soaking in electrolyte. Under these conditions PEO crystallization should occur spontaneously but for $(PEO/ANF)_n$ composites crystallization is prohibited due to LBL deposition and the presence of the nanofibers. The amorphous nature of PEO in $(PEO/ANF)_n$ was confirmed by X-ray diffraction (XRD), which displayed a diffuse broad band for 2θ between 20° and 30° instead of the sharp peaks at 2θ = 19° and 2θ = 23° observed in crystalline PEO (Figure 2-4).

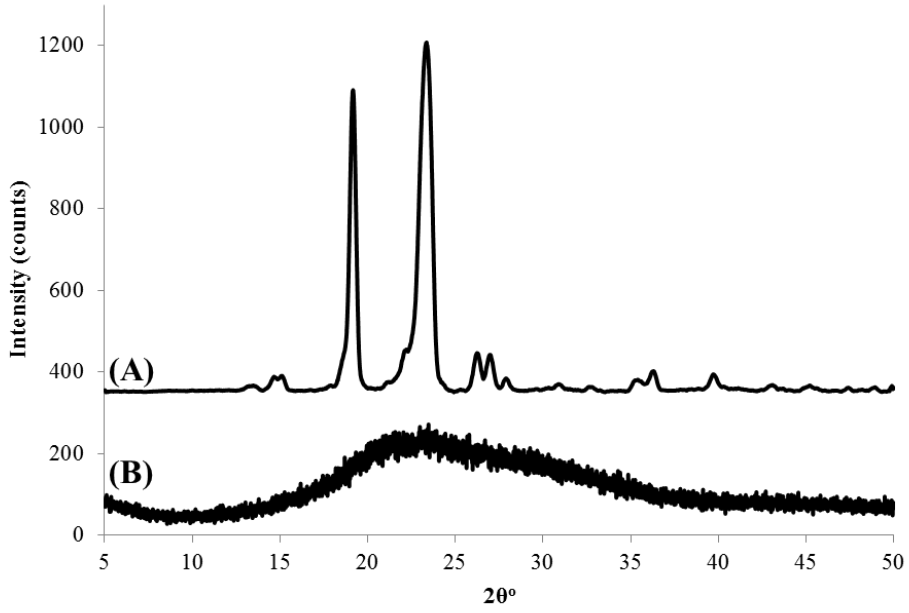

Figure 2-4 XRD pattern of (A) neat PEO and (B) $(PEO/ANF)_{200}$

Differential scanning calorimetry data (DSC) also support this conclusion (Figure *2-8*c). Neat PEO shows a sharp endotherm around 70 °C corresponding to the T_m of the crystalline polymer, which is completely absent in the DSC curve for $(PEO/ANF)_n$ (Figure *2-8*c). In FT-IR spectra of the composite, we observed a strong peak at 2860 cm^{-1} (Figure 2-5) assigned to intermolecular hydrogen bonds between PEO and ANF. These bonds are credited with the prevention of PEO crystallization as well as efficient LBL assembly,[31] consistent with previous findings for PEO-based ion conductors[36].

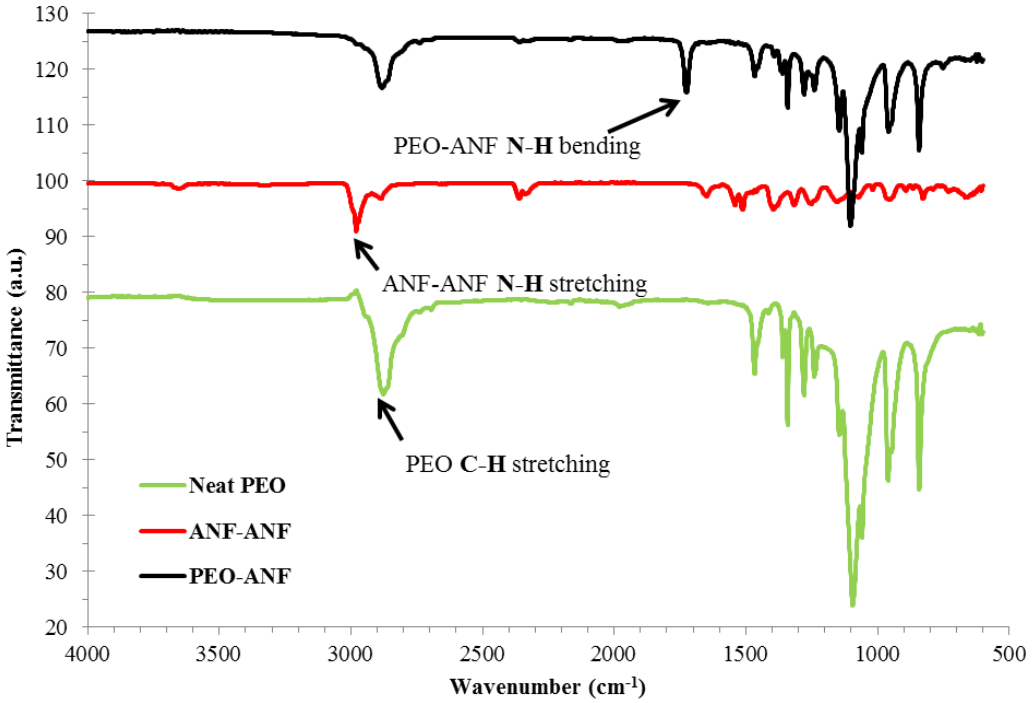

Figure 2-5 FT-IR spectra of (A) neat PEO, (B) $(ANF/ANF)_{100}$, and (C) $(PEO/ANF)_{200}$. A distinct peak at 1729 cm^{-1} found in PEO-ANF nanocomposite is assigned to bending vibration of N-H and represents strong hydrogen bonding between PEO and ANF.

In order to investigate ionic conductivity, free-standing $(PEO/ANF)_n$ membranes were sandwiched between two lithium metal electrodes and housed in a CR2032 coin battery cell. Without any additives or additional treatments the ionic conductivities of $(PEO/ANF)_{200}$ at 25 °C and 90 °C were $\Omega_{ICM,25°C}$ = 5.0x10^{-6} S/cm and $\Omega_{ICM,90°C}$ = 2.6x10^{-5} S/cm, respectively. The $(PEO/ANF)_{200}$ membrane was immersed in a 1M lithium triflate solution and 1M lithium bis(trifluoromethane)sulfonamide solution in a propylene carbonate (PC)/dimethyl carbonate (DMC) 1:1 v/v mixture, followed by overnight drying in a vacuum oven. The ionic conductivity of $(PEO/ANF)_{200}$ was subsequently found to be 5.5x10^{-5} S/cm and 2.5x10^{-5} S/cm respectively, comparable to that of some Li sulfide glasses[10,24]. EIS curves showed a depressed semicircle shape (Figure *2-6*), typical of solid electrolytes[20,25]. No change in ICM thickness or other indications of swelling or conversely PEO crystallization as a result of salt intercalation[36] were observed in this process. This

electrolyte incubation step was needed to impregnate initial concentrations of Li^+ ions and to avoid an initial "ramp up" period.

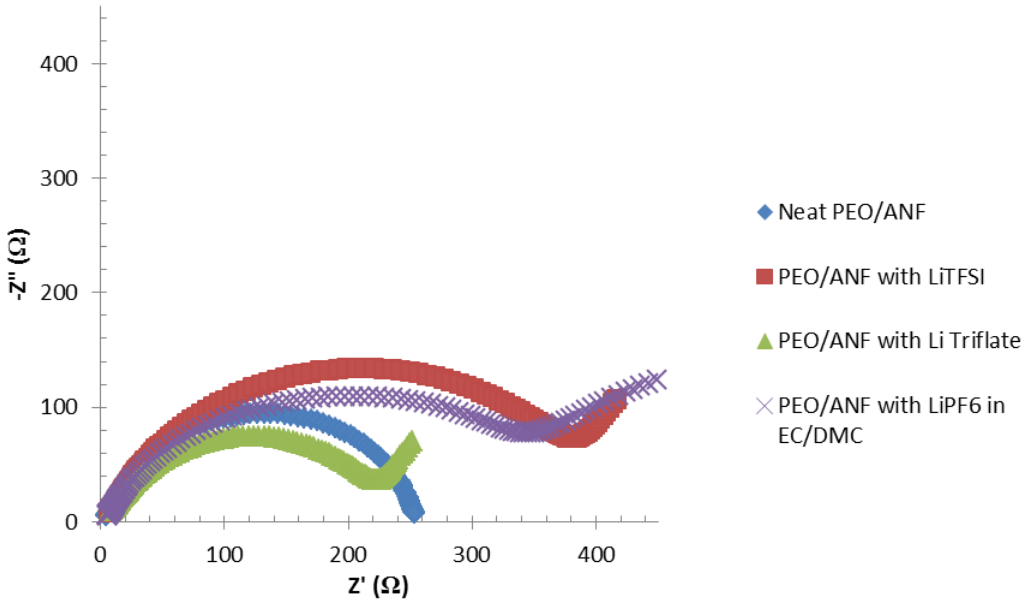

Figure *2-6* Electrochemical impedance spectra of (A, blue) Neat PEO/ANF (B, red) PEO/ANF with LiTFSI, (C, green) PEO/ANF with Li Triflate, and (D, purple) PEO/ANF with $LiPF_6$ in EC/DMC.

To better replicate actual battery conditions and mitigate contact resistance between the electrode and the solid $(PEO/ANF)_{200}$ membranes, 150 µL of a 1M lithium hexafluorophosphate solution in an ethylene carbonate (EC)/dimethyl carbonate (DMC) 1:1 v/v mixture was added to each side of the membrane as was used in other studies on compliant composite ICMs[20]**.** In this case the ionic conductivity of $(PEO/ANF)_{200}$ reached $\Omega_{ICM,25°C}$ = 1.7x10^{-4} S/cm. Note that this value reflects the low limit of ionic conductivity for $(PEO/ANF)_{200}$ under actual operating conditions in a battery because the temperature between electrodes is substantially higher than room temperature.

2.3.3 Dendrite Suppression

With respect to dendrite propagation, we must point out that careful investigation of lithium dendrite growth and suppression is well known to be complicated due to high reactivity of lithium metal with ambient air and water. Moreover, the fast oxidation of Li metal changes the shape, length, and mechanical properties of the dendrites, making the results inconclusive. Imaging of lithium dendrite growth using synchrotron-based X-ray tomography[19] and electrochemical liquid TEM holders can potentially be applied to this system[37], but we decided to look for a simpler method that can be applied consistently to many different LBL-made ICMs for many different types of batteries with standard equipment base. Therefore we decided to carry out the analogous study for copper dendrites, which can serve as convenient "*mechanical*" proxy for lithium dendrites as an experimental model under ambient conditions. The results obtained for copper are relevant for lithium because the Young's modulus of copper is E = 129.8 GPa, while that for lithium is E = 4.91 GPa. The theory of electrochemical dendrite growth[38] indicates that if local mechanical properties of ICM are sufficient to prevent mechanical stress copper dendrites, it will also suppress lithium dendrites, which are much softer. It is important to reiterate that copper is used here only as a mechanical study, we do not claim that copper and lithium are electrochemically similar.

To experimentally design successful dendrite-suppressing ICMs we need to consider the dimensions of dendrites and ion-conducting pores. In comparison, we observed that copper dendrites have growth zones with a size of 50-100 nm and tip diameters of 25 nm (Figure 2-1b, right), and so do dendrites from lithium.[19] We have also observed that lithium dendrites are approximately twice the size of copper dendrites (Figure 2-1b, left), making

copper dendrite suppressing more challenging than lithium while retaining the same fern-like shape. The similarity of shapes confirms the usefulness of the use of copper dendrites as the mechanical proxy of lithium dendrites because the congruency of the dendrite footprints on the membrane.

The dendrites propagate through ICMs via the path of least mechanical resistance. Importantly, typical polymeric ICMs are made as heterogeneous membranes to provide high ionic conductivities. Therefore, if a heterogeneous material has soft pores larger than d_{dendr}, those parts with low moduli determine the propagation of dendrites rather than the stiffer parts. If the heterogeneity of an ICM is smaller than d_{dendr}, the growth zone the dendrite experiences a resistance equivalent to the average modulus of the membrane.

Many ICMs are strongly heterogeneous at scales much greater than d_{dendr}. Celgard, for instance, is microscopically stiff with E = 1.1 GPa and a tensile strength of 11.1 MPa, but it contains large pores of ion-conducting gel with sizes of *ca.* 430 nm (Figure 2-1a). Consequently, the mechanical properties relevant to dendrite growth are those found in propylene carbonate and ethylene carbonate loaded with lithium salts. Being liquids, the electrolytes offer little to no resistance to block dendrite growth.

The scale of inhomogeneity and dendrite inhibition in $(PEO/ANF)_n$ is very different. $(PEO/ANF)_n$ exists as a film of tightly interconnected PEO and ANF networks. Pores in the film are 20 nm in diameter (Figure 2-1c,d) smaller than d_{dendr}. Therefore, the growing dendrites will experience the component-averaged (macroscopic) stiffness of $(PEO/ANF)_n$.

Investigation of dendrite growth was carried out under conditions of high current density (10.3 mA/cm^2), equivalent to a 6-7 C charge/discharge rate. Under such conditions, one

could fully charge a battery in less than 10 minutes, while the typical charging rate for batteries is *ca* 0.25 C. Copper electrodes coated with $(PEO/ANF)_{10}$, $(PEO/ANF)_{30}$, and $(PEO/ANF)_{50}$ were investigated by SEM (Figure *2-7*) after a total charge of Q = 0.006 mAh/cm^2 was transferred. Copper dendrites with an average size of 500 nm formed on the bare Cu electrode (Figure *2-7*a, e, i). Notably the shape of dendrites was strikingly similar to those formed by lithium.[19]

The size of the dendrites was markedly reduced to 100-200 nm after depositing $(PEO/ANF)_{10}$ (Figure *2-7*b, f, j), corresponding to a 160±2 nm coating on the electrode. Dendrite formation could no longer be detected for the electrode coated with $(PEO/ANF)_{30}$ (Figure *2-7*c, g, k), which corresponds to a film thickness of 486 nm. The dendrites were reduced to an evenly deposited layer at the interface ***underneath*** the ICM, which is exactly what is needed for high performance safe anodes. Deposition of $(PEO/ANF)_{50}$ films with a thickness of 810±5 nm results in complete inhibition of dendrite formation (Figure *2-7*d, h, l). We believe that $(PEO/ANF)_n$ films suppress the growth of dendritic deposits by exerting a compressive force on their growth points while being able to sustain the ionic flux through the membrane in accord with a previously elaborated theoretical mechanism[22].

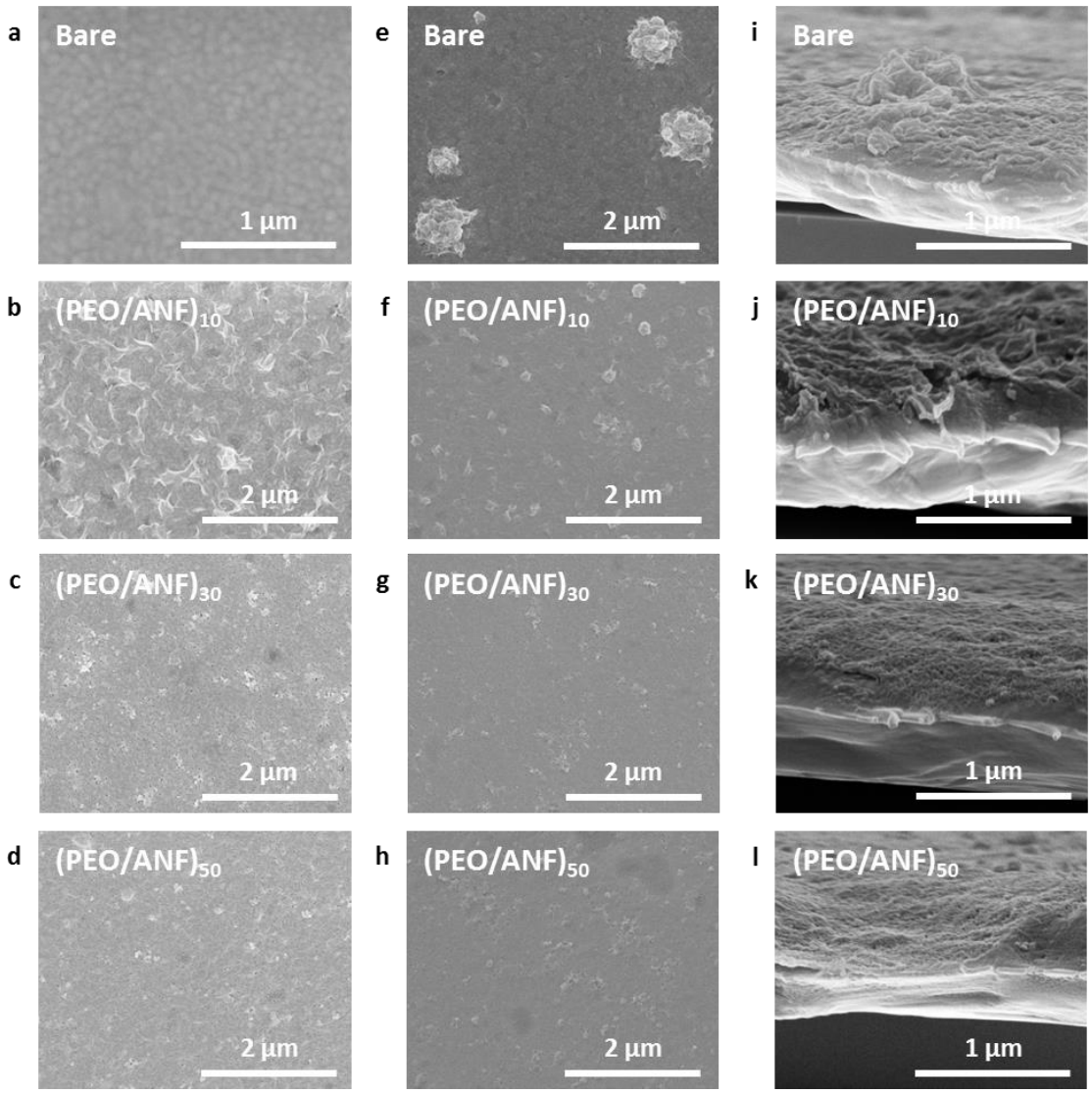

Figure *2-7* (a-d) SEM images of bare PVD copper electrode with (a) no coating; (b) $(PEO/ANF)_{10}$; (c) $(PEO/ANF)_{30}$; (d) $(PEO/ANF)_{50}$ prior to dendrite growth. (e-l) SEM images of the same electrodes after copper dendrite growth with current density of 10.3 mA/cm^2 on (e) bare copper electrode; copper electrode coated with (f) $(PEO/ANF)_{10}$; (g) $(PEO/ANF)_{30}$; and (h) $(PEO/ANF)_{50}$. (i), (j), (k), (l) are cross-sectional images of the same electrodes as in (e), (f), (g), (h) respectively. Total charge transferred = 0.02 C/cm^2.

2.3.4 Thermal Stability

Studies were conducted to comparatively investigate the thermal stability of $(PEO/ANF)_n$ nanocomposites. High temperature stability of ICMs is needed to the improve safety of current lithium batteries at elevated temperatures, exemplified by the conditions under the

hood of the car (120 °C) or in the case of a malfunctioning thermal management system. Higher temperature stability is a key parameter for high charge density, high discharge rate batteries.[39,40] In the hot solder iron test accepted in industry as standard, a 180 °C solder iron tip was placed on both a PEO-ANF film and a Celgard 2400 PE separator for 30 seconds. The Celgard 2400 PE burns with the formation of a hole. In contrast, the PEO-ANF film showed no damage (Figure *2-8*a), in accordance with the high temperature stability of Kevlar being translated into ANFs. In the high temperature oven test, both PEO-ANF and Celgard 2400 PE were kept at 200 °C for 10 minutes. The Celgard PE melted completely. The PEO-ANF remained flat, intact, and un-deformed (Figure *2-8*b), indicating that high-temperature shrinkage and deformation are minimal for $(PEO/ANF)_n$ ICMs. Thermal stability of the PEO-ANF nanocomposite investigated by DSC and TGA (Figure *2-8*c & d) demonstrated stability exceeding 400 °C, which is exceptional among polymeric ICMs and is, again, comparable to Li-based ceramics[10].

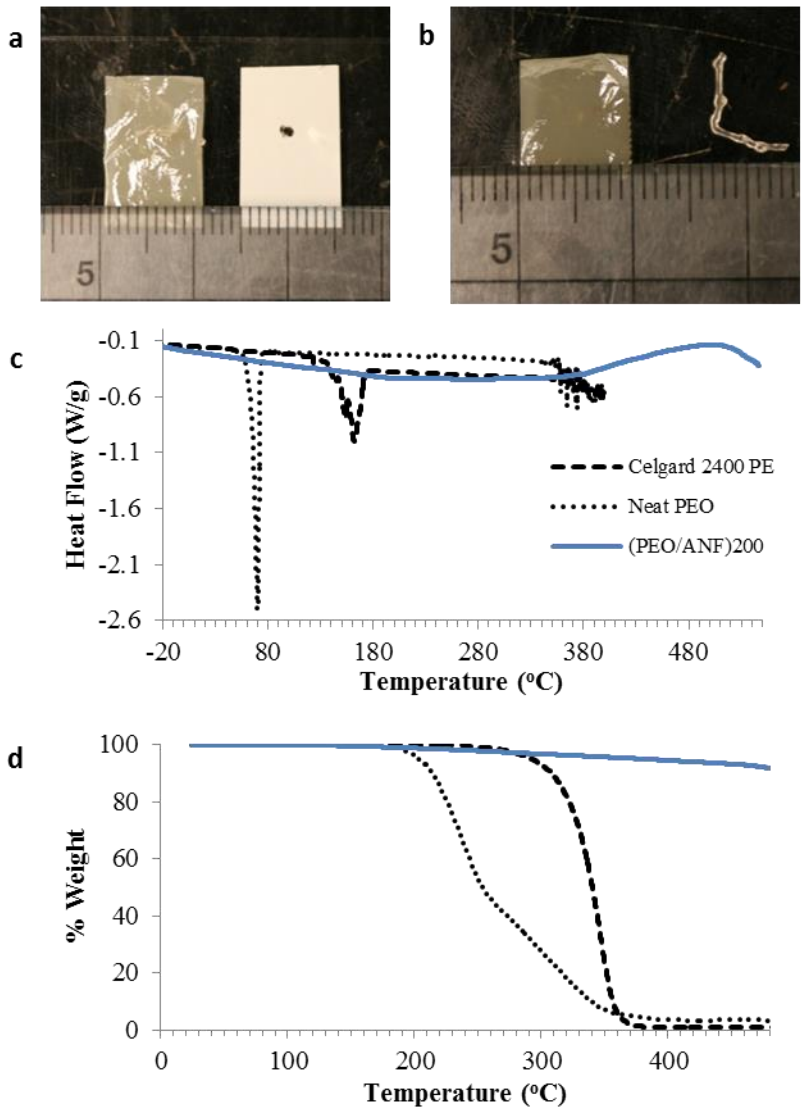

Figure *2-8* Thermal Stability Studies of $(PEO/ANF)_n$. (a) Hot solder iron test on $(PEO/ANF)_{200}$ and Celgard™ 2400 PE. (b) High temperature oven test on $(PEO/ANF)_{200}$ and Celgard™ 2400 PE (c) DSC and (d) TGA curves for $(PEO/ANF)_{200}$ (blue solid) neat PEO (black dotted), and Celgard™ 2400 PE (black dashed).

2.4 Discussion

The breakthrough of combining high ionic conductance and high modulus is illustrated in Figure *2-9*a, which summarizes mechanical and electrochemical properties of current ICMs and $(PEO/ANF)_n$. Detailed descriptions of the ICMs are listed in Appendix A. Commonly-used separators such as Celgard monolayer PP, PE, and trilayer PP/PE/PP have thicknesses

of 12 to 40 μm, and when infused with electrolyte give an internal resistance of R_I = 0.25 Ohm. However, the large pores providing the conductive pathways also allow uninhibited growth of dendrites because of the softness of the contained gel. Polymeric electrolytes containing inorganic or organic fillers – solid ICMs that are most closely related to $(PEO/ANF)_n$ composites -- are typically cast with thicknesses of 100 to 400 μm. They typically display R_I values as high as 2000 Ohm. The high strength and ionic conductivity of $(PEO/ANF)_n$ makes possible substantial reductions in ICM thicknesses and significantly decrease R_I by 2-3 orders of magnitude. A 500 nm $(PEO/ANF)_{30}$ ICM introduces R_I = 0.16 Ohm into the CR2032 battery cell. The ANF-based composites are competitive in all respects with the best Li-based ceramics (Figure *2-9*a) while also retaining flexibility and toughness. Utilization of the high-strength insulating nanofibers of ANF and the nanoscale porosity of their networks in LBL films allowed us to combine the advantages of glass and polymeric ion conductors.

To substantiate the practicality of $(PEO/ANF)_n$ ICMs and their chemical stability in contact with lithium metal, we assembled a battery cell using $(PEO/ANF)_{200,}$ lithium metal anode, and $LiCoO_2$ cathode. The cell was studied over 50 cycles at C/4 (39 mA/g, Figure *2-9*b). The battery exhibited a typical discharge capacity of over 130 mAh/g with a discharge efficiency as high as 98%. Although the battery parameters are limited by the stability of the $LiCoO_2$ cathode and the charge transfer kinetics at both cathode and anode, complicating evaluation at extreme charge rates, this test demonstrates that a film as thin as 3 μm can perform at least as well as 25 μm thick layer of Celgard and prevent rapid deterioration of the battery due to lithium metal dendrite growth. Repeated acquisition of cyclic voltammograms of the cell (Figure *2-10*) showed redox peaks at around 4.05V and

4.19V typical for $LiCoO_2$ cathode[41] without the appearance of any new redox peaks confirming chemical stability from the PEO/ANF film.

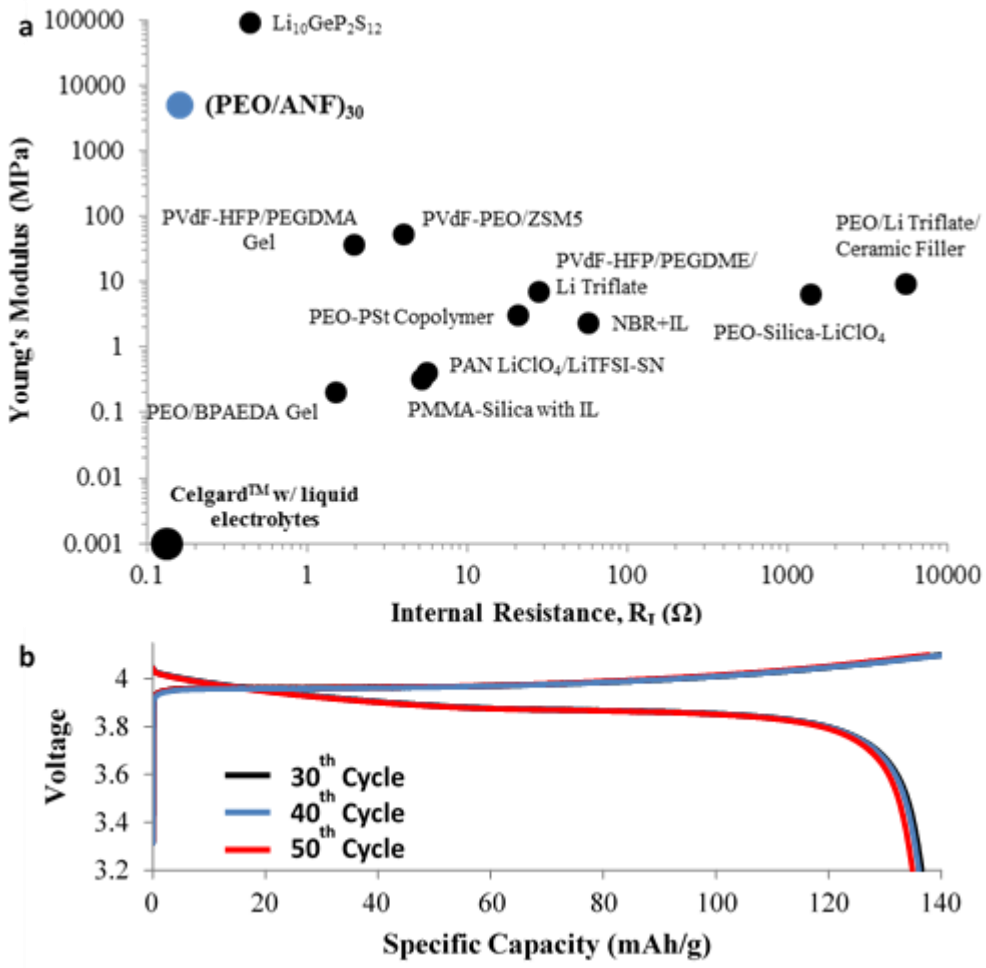

Figure *2-9* (a) Comparative evaluation of stiffness and internal resistance normalized to a standard CR2032 coin cell for $(PEO/ANF)_{200}$ and other ICMs. The corresponding references and the list of abbreviations are given in Appendix A (PEGDMA-polyethylene glycol dimethacrylate, PEGDME – poly(ethylene glycol)dimethyl ethers, NBR – nitrile rubber, IL – ionic liquids, BPAEDA – bisphenol A ethoxylate diacrylate, PSt – polystyrene, PAN – polyacrylonitrile, SN – succinonitrile, PMMA – poly(methyl methacrylate)); (b) Charge-discharge curve for the 30th, 40th, and 50th cycle of a CR2032 button cell consisting of a $LiCoO_2$ cathode, $(PEO/ANF)_{200}$ with 300µL 1M $LiPF_6$ in EC/DMC, and a lithium metal anode at C/4 charge/discharge rate.

$(PEO/ANF)_{200}$ were also assembled into symmetric Li/separator/Li coin cells to further exemplify suppression of lithium dendrites. Along with a control cell using Celgard 2400 as separator, the cells are subjected to $0.25mA/cm^2$ current density and the current direction

is reversed every 30 mins. Under these conditions stimulating the growth of dendrites, the control cell with Celgard 2400 showed a steady decrease in its voltage profile from the 1st cycle at 0.05V to the 2500th cycle at 0.02V (Figure 2-11A) indicating a so called "soft short" when ICM is slowly penetrated by lithium dendrites. As for the cell with $(PEO/ANF)_{200}$, the voltage profile was maintained at 0.03V starting from the 100th cycle to the 2500th cycle (Figure 2-11B). The steady voltage profile for cells with $(PEO/ANF)_{200}$ suggests that lithium dendrites are effectively suppressed.

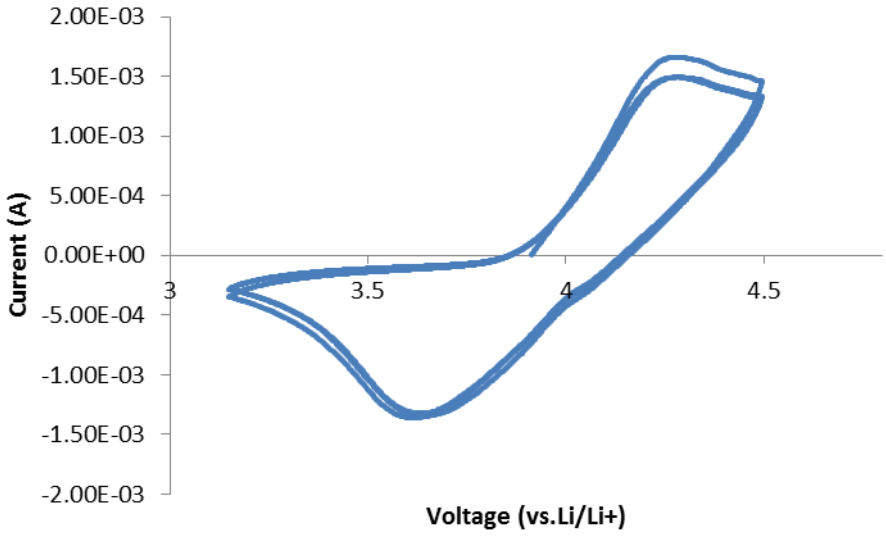

Figure *2-10* Cyclic voltammogram for a coin cell with PEO/ANF as membrane, $LiCoO_2$ cathode and lithium metal anode. Scan rate= 0.3mV/s from 3.2V to 4.5V.

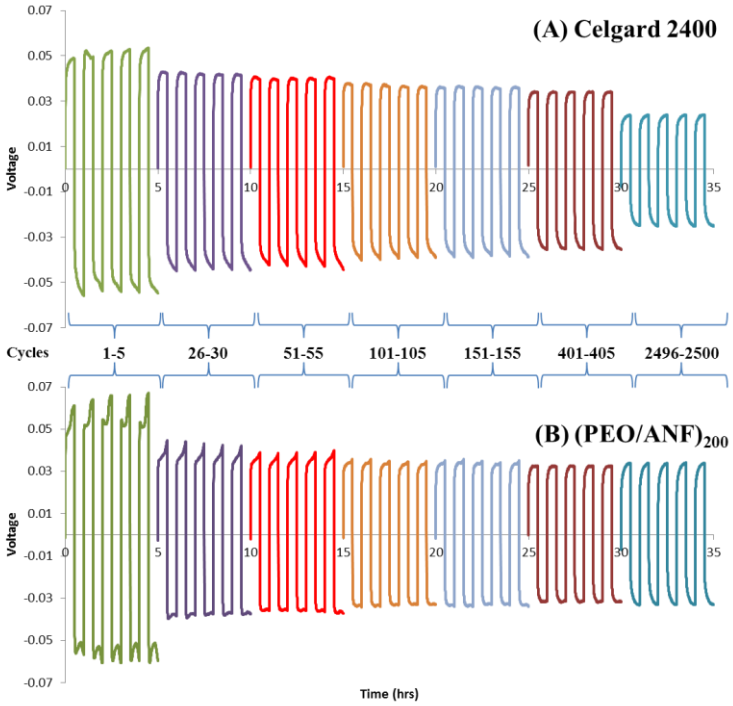

Figure 2-11 Li/separator/Li symmetric cells of (A) Celgard 2400 PE and (B) (PEO/ANF)200, where the cells are cycled at 0.25mA/cm^2 with the current direction changed every 30 minutes.

2.5 Conclusions

In conclusion, we have demonstrated that PEO and ANFs can be assembled into solid ICMs in which amorphous PEO produces ion-conducting channels smaller than d_{dendr}. Consequently, $(PEO/ANF)_n$ composite with n = 30-50 are capable of suppression of hard copper and soft lithium dendrites while displaying ionic conductivity as high as 1.7×10^{-4} S/cm. Resilience to harsh electrochemical and thermal conditions, as well as high flexibility and high ionic flux accompany the dendrite suppression capabilities, which is difficult to achieve in other classes of ion-conducting materials. Future studies related to metal crystallization under mechanical stress taking place under $(PEO/ANF)_n$ and dendrite suppression for other potential anode materials, such as sodium (*E=10 GPa)* and magnesium (*E=45 GPa)* are envisioned.

References

1. Scrosati, B. & Garche, J. Lithium batteries: Status, prospects and future. *Journal of Power Sources* **195,** 2419–2430 (2010).

2. Su , D. S. & Schlögl, R. Nanostructured Carbon and Carbon Nanocomposites for Electrochemical Energy Storage Applications. *ChemSusChem* **3,** 136–168 (2010).

3. Kovalenko, I. *et al.* A Major Constituent of Brown Algae for Use in High-Capacity Li-Ion Batteries. *Science* **334,** (2011).

4. Hyder, M. N. *et al.* Layer-by-Layer Assembled Polyaniline Nanofiber/Multiwall Carbon Nanotube Thin Film Electrodes for High-Power and High-Energy Storage Applications. *ACS Nano* **5,** 8552–8561 (2011).

5. Wegst, U. G. K. & Ashby, M. F. The mechanical efficiency of natural materials. *Philosophical Magazine* **84,** 2167–2186 (2004).

6. Ritchie, R. O. The conflicts between strength and toughness. *Nature Materials* **10,** 817–822 (2011).

7. Barthelat, F. Biomimetics for next generation materials. *Philosophical Transactions of the Royal Society of London A: Mathematical, Physical and Engineering Sciences* **365,** (2007).

8. Keten, S., Xu, Z., Ihle, B. & Buehler, M. J. Nanoconfinement controls stiffness, strength and mechanical toughness of β-sheet crystals in silk. *Nature Materials* **9,** 359–367 (2010).

9. Kim, Y. *et al.* Stretchable nanoparticle conductors with self-organized conductive

pathways. *Nature* **500,** 59–63 (2013).

10. Knauth, P. Inorganic solid Li ion conductors: An overview. *Solid State Ionics* **180,** 911–916 (2009).

11. Agrawal, R. C. *et al.* Solid polymer electrolytes: materials designing and all-solid-state battery applications: an overview. *Journal of Physics D: Applied Physics* **41,** 223001 (2008).

12. Chan, C. K. *et al.* High-performance lithium battery anodes using silicon nanowires. *Nature Nanotechnology* **3,** 31–35 (2008).

13. Bruce, P. G., Freunberger, S. a., Hardwick, L. J. & Tarascon, J.M. Li–O_2 and Li–S batteries with high energy storage. *Nature Materials* **11,** 172–172 (2011).

14. Tarascon, J. M. & Armand, M. Issues and challenges facing rechargeable lithium batteries. *Nature* **414,** 359–367 (2001).

15. Goodenough, J. B. & Kim, Y. Challenges for Rechargeable Li Batteries. *Chemistry of Materials* **22,** 587–603 (2010).

16. Vetter, J. *et al.* Ageing mechanisms in lithium-ion batteries. *Journal of Power Sources* **147,** 269–281 (2005).

17. Adam Heller. The GS Yuasa-Boeing 787 Li-ion battery: test it at a low temperature and keep it warm in flight. *The Electrochemical Society Interface* 1 (2013).

18. Armand, M. & Tarascon, J. M. Building better batteries. *Nature* **451,** 652–657 (2008).

19. Harry, K. J., Hallinan, D. T., Parkinson, D. Y., MacDowell, A. A. & Balsara, N. P.

Detection of subsurface structures underneath dendrites formed on cycled lithium metal electrodes. *Nature Materials* **13,** 69–73 (2013).

20. Kim, S. H., Choi, K. H., Cho, S. J., Kil, E. H. & Lee, S. Y. Mechanically compliant and lithium dendrite growth-suppressing composite polymer electrolytes for flexible lithium-ion batteries. *Journal of Materials Chemistry A* **1,** 4949 (2013).

21. Yamaki, J. *et al.* A consideration of the morphology of electrochemically deposited lithium in an organic electrolyte. *Journal of Power Sources* **74,** 219–227 (1998).

22. Monroe, C. & Newman, J. The Impact of Elastic Deformation on Deposition Kinetics at Lithium/Polymer Interfaces. *Journal of The Electrochemical Society* **152,** A396 (2005).

23. Stone, G. M. *et al.* Resolution of the Modulus versus Adhesion Dilemma in Solid Polymer Electrolytes for Rechargeable Lithium Metal Batteries. *Journal of the Electrochemical Society* **159,** A222–A227 (2012).

24. Minami, T., Hayashi, A. & Tatsumisago, M. Recent progress of glass and glass-ceramics as solid electrolytes for lithium secondary batteries. *Solid State Ionics* **177,** 2715–2720 (2006).

25. Kamaya, N. *et al.* A lithium superionic conductor. *Nature Materials* **10,** 682–686 (2011).

26. Yang, M. *et al.* Dispersions of Aramid Nanofibers : A New Nanoscale Building Block. *ACS Nano* 6945–6954 (2011).

27. Tang, Z., Wang, Y., Podsiadlo, P. & Kotov, N. A. Biomedical Applications of

Layer-by-Layer Assembly: From Biomimetics to Tissue Engineering. *Advanced Materials* **18,** 3203–3224 (2006).

28. Ariga, K. *et al.* Layer-by-layer assembly as a versatile bottom-up nanofabrication technique for exploratory research and realistic application. *Physical Chemistry Chemical Physics* **9,** 2319 (2007).

29. Hammond, P. T. Form and Function in Multilayer Assembly: New Applications at the Nanoscale. *Advanced Materials* **16,** 1271–1293 (2004).

30. Jiang, C. & Tsukruk, V. V. Freestanding Nanostructures via Layer-by-Layer Assembly. *Advanced Materials* **18,** 829–840 (2006).

31. Kharlampieva, E., Kozlovskaya, V. & Sukhishvili, S. A. Layer-by-Layer Hydrogen-Bonded Polymer Films: From Fundamentals to Applications. *Advanced Materials* **21,** 3053–3065 (2009).

32. Decher, G. Fuzzy Nanoassemblies: Toward Layered Polymeric Multicomposites. *Science* **277,** (1997).

33. Shim, B. S. *et al.* Multiparameter Structural Optimization of Single-Walled Carbon Nanotube Composites: Toward Record Strength, Stiffness, and Toughness. *ACS Nano* **3,** 1711–1722 (2009).

34. DeLongchamp, D. M. & Hammond, P. T. Fast Ion Conduction in Layer-By-Layer Polymer Films. *Chemistry of Materials* **15,** 1165–1173 (2003).

35. Lowman, G. M., Tokuhisa, H., Lutkenhaus, J. odie L. & Hammond, P. T. Novel Solid-State Polymer Electrolyte Consisting of a Porous Layer-by-Layer

Polyelectrolyte Thin Film and Oligoethylene Glycol. *Langmuir* **20,** 9791–9795 (2004).

36. Christie, A. M., Lilley, S. J., Staunton, E., Andreev, Y. G. & Bruce, P. G. Increasing the conductivity of crystalline polymer electrolytes. *Nature* **433,** 50–53 (2005).

37. Holtz, M. E. *et al.* Nanoscale Imaging of Lithium Ion Distribution During In Situ Operation of Battery Electrode and Electrolyte. *Nano Letters* **14,** 1453–1459 (2014).

38. Monroe, C. & Newman, J. Dendrite Growth in Lithium/Polymer Systems. *Journal of The Electrochemical Society* **150,** A1377 (2003).

39. Wang, Q. *et al.* Thermal runaway caused fire and explosion of lithium ion battery. *Journal of Power Sources* **208,** 210–224 (2012).

40. Cho, J., Kim, Y. J. & Park, B. Novel $LiCoO_2$ Cathode Material with Al2O3 Coating for a Li Ion Cell. *Chemistry of Materials* **12,** 3788–3791 (2000).

41. Roth, E. P., Doughty, D. H. & Pile, D. L. Effects of separator breakdown on abuse response of 18650 Li-ion cells. *Journal of Power Sources* **174,** 579–583 (2007).

Appendix A

Supporting Information

During the calculation of the internal resistance contribution by different electrolytes, the electrode area was taken to be the area of a typical electrode in a CR2032 coin cell (diameter=15.6mm). The elastic modulus (E), ionic conductivity, and thickness of electrolytes were taken from the citations list below.

Table A-1 Table of abbreviations used in Figure *2-9*a

Abbreviation	Description	Citation
$Li_{10}GeP_2S_{12}$	When calculating internal resistance for $Li_{10}GeP_2S_{12}$, the thickness was taken to be 100μm according to the citation (9)T. Inada et.al in the paper.	1
PVdF-HFP/PEGDME/Li Triflate	PEGDME stands for poly(ethylene glycol) dimethyl ethers.	2
PVdF-HFP/PEGDMA Gel	PEGDMA stands for polyethylene glycol dimethacrylate.	3
NBR+IL	NBR stands for nitrile rubber. IL stands for ionic liquid.	4
PMMA-Silica with IL	PMMA stands for poly(methyl methacrylate). IL stands for ionic liquid.	5
PEO/BPAEDA Gel	BPAEDA stands for bisphenol A ethoxylate diacrylate.	6
PEO-Silica-$LiClO_4$	PEO stands for polyethylene oxide	7
PEO-PSt Copolymer	PSt stands for polystyrene.	8
PAN $LiClO_4$/LiTFSI-SN	SN stands for succinonitrile. PAN stands for polyacrylonitrile.	9
PVdF-PEO/ZSM5	ZSM5 is a kind of microporous molecular sieve.	10
PEO/Li Triflate/Ceramic filler	Ceramic filler used is Li Nasicompound $[Li_{1.4}(Al_{0.4}Ge_{1.6})(PO_4)_3]$.	11
Celgard™ w/Liquid electrolytes		12

1. N. Kamaya, K. Homma, Y. Yamakawa, M. Hirayama, R. Kanno, M. Yonemura, T. Kamiyama, Y. Kato, S. Hama, K. Kawamoto, A. Mitsui, A lithium superionic conductor, *Nature materials* **10**, 682-686 (2011).

2. K. Abraham, Z. Jiang, B. Carroll, Highly conductive PEO-like polymer electrolytes, *Chemistry of Materials*, 1978-1988 (1997).

3. C. L. Cheng, C. C. Wan, Y. Y. Wang, Microporous PVdF-HFP based gel polymer electrolytes reinforced by PEGDMA network, *Electrochemistry Communications* **6**, 531-535 (2004).

4. M. Cho, H. Seo, J. Nam, H. Choi, J. Koo, Y. Lee, High ionic conductivity and mechanical strength of solid polymer electrolytes based on NBR/ionic liquid and its application to an electrochemical actuator, *Sensors and Actuators B: Chemical* **128**, 70-74 (2007).

5. F. Gayet, L. Viau, F. Leroux, F. Mabille, Unique Combination of Mechanical Strength, Thermal Stability, and High Ion Conduction in PMMA− Silica Nanocomposites Containing High Loadings of Ionic Liquid, *Chemistry of Materials*, 5575-5577 (2009).

6. Y. Kang, K. Cheong, K. Noh, C. Lee, D. Seung, A study of cross-linked PEO gel polymer electrolytes using bisphenol A ethoxylate diacrylate: ionic conductivity and mechanical properties, *Journal of Power Sources* **119-121**, 432-437 (2003).

7. J. Kweon, S. Noh, Thermal, thermomechanical, and electrochemical characterization of the organic–inorganic hybrids poly(ethylene oxide) (PEO)–silica and PEO–silica–LiClO4, *Journal of Applied Polymer Science* **81**, 2471-2479 (2001).

8. T. Niitani, M. Shimada, K. Kawamura, K. Dokko, Y. Rho, K. Kanamura, Synthesis of Li^+ Ion Conductive PEO-PSt Block Copolymer Electrolyte with Microphase Separation Structure, *Electrochemical and Solid-State Letters* **8**, A385 (2005).

9. M. Patel, K. Chandrappa, A. Bhattacharyya, Increasing ionic conductivity and mechanical strength of a plastic electrolyte by inclusion of a polymer, *Electrochimica Acta* **54**, 209-215 (2008).

10. J. Xi, X. Qiu, L. Chen, PVDF–PEO/ZSM-5 based composite microporous polymer electrolyte with novel pore configuration and ionic conductivity, *Solid State Ionics*, 709-713 (2006).

11. C. Leo, Studies on plasticized PEO–lithium triflate–ceramic filler composite electrolyte system, *Solid State Ionics* **148**, 159-171(2002).

12. Stallworth, P. E. *et al.* NMR, DSC and high pressure electrical conductivity studies of liquid and hybrid electrolytes. *Journal of Power Sources* **81-82,** 739-747 (1999).

Chapter 3

Nanoporous Aramid Nanofiber Separators for Non-Aqueous Redox Flow Batteries

3.1 Background and Approach

Redox flow batteries (RFB) have been identified as promising candidates for use in grid scale energy storage applications.[1] These systems offer significant advantages over other large-scale storage options, including flexibility as a consequence of long lifetimes, decoupled power and energy densities, and facile thermal management.[2,3] RFBs store energy in liquid electrolytes that contain redox-active species and supporting electrolyte dissolved in a solvent. During charge and discharge the electrolyte is circulated through porous electrodes on either side of a flow cell assembly.[4] Electrically insulating separators or ion exchange membranes (IEM) are used to isolate the positive and negative electrolytes while allowing counter ion transport to maintain overall charge neutrality.[5] Maintaining active species separation is critical to limiting self-discharge and achieving high coulombic efficiencies.

Commercial RFBs utilize aqueous solutions of transition metal salts,[3,6] however, maximum energy densities for aqueous RFBs are limited by the relatively narrow electrochemical window of water (~1.2-1.6 V).[7–9] An attractive approach to address this limitation involves the use of non-aqueous solvents.[10] Non-aqueous solvents offer improved voltage windows (>4 V)[11] and with the recent development of highly soluble active species, [12,13] non-

aqueous RFBs (NAqRFBs) present an opportunity to increase energy and power densities beyond those of aqueous systems.[5,8] However, one of the major challenges in NAqRFB development is the lack of suitable ion exchange membranes or separators. A variety of IEMs are available for use in aqueous RFBs,[5,8,14,15] but they are relatively ineffective in non-aqueous media. For example, the ionic conductivity of Nafion is five orders of magnitude lower for acetonitrile based electrolytes compared to aqueous electrolytes.[16,17] In addition, a number of promising NAqRFB chemistries use anions such as tetrafluoroborate (BF_4^-) or hexafluorophosphate (PF_6^-) as charge carriers,[9,10,18–23] necessitating anion exchange membranes (AEM). Several AEMs including Neosepta AHA (ASTOM, Japan), [9,10] UltrexTM AMI-7001 (Membranes international Ltd., USA),[24] and FAP4 (FuMa-Tech Co.)[22] have been used in H-type and flow battery configurations. These AEMs, which were designed primarily for water treatment,[25] are subject to long term incompatibility issues when contacted with organic solvents,[8] In developing novel membrane/separator materials suitable for use in NAqRFBs, the goal is a membrane/separator that provides high selectivity by allowing facile transport of supporting electrolyte ions while prohibiting the transport of active species. Additionally, this material should exhibit chemical and mechanical stability, along with low manufacturing costs.

Only a few IEMs have been developed for NAqRFBs. Kim et al. described the fabrication of a composite material consisting of a porous polyolefin separator infiltrated with a quaternized poly(styrene-divinylbenzene-vinylbenzyl chloride) copolymer.[26] Maurya et al. synthesized an AEM via the simultaneous polymerization and quaternization of 4-vinyl pyridine and subsequent film casting into a thin membrane.[27] More recently, Won has

demonstrated a simple approach by coating a porous Celgard 2400 support with poly(diallydimethylammonium chloride) and urushi composite to form a selective composite membrane. Urushi, or oriental lacquer, is a natural polymeric material with a high durability and toughness that has been used for centuries Asian lacquerware. These works have demonstrated lower permeability of the active species as a result of the cross-linked polymer chains and markedly improved mechanical stabilities.[28] However, concerns have been raised regarding cost and incompatibilities with the organic solvents and active materials in NAqRFBs.[8]

In response to concerns regarding membranes, nanoporous separators have been investigated for use in NAqRFBs. Nanoporous separators achieve selectivity by taking advantage of size differences between the redox active species and the supporting electrolyte ions. The major advantages associated with these separators are simplicity of design and low cost when compared to IEMs.[29] Nanoporous silica,[30] polyacrylonitrile[31] and composite[32] membranes have been successfully demonstrated in aqueous RFBs. This concept was also demonstrated for polysulfide blocking in lithium-sulfur flow batteries using a polymer with intrinsic microporosity.[33] In NAqRFBs, size-selectivity was recently reported by utilizing a redox active polymer with pore sizes on the same order of magnitude as Celgard 2325, a commercial polyolefin separator with pore size of 28 nm.[34] However, many of the active species under consideration for NAqRFBs are significantly smaller in size. For a practical nanoporous separator, pore sizes on the order of a few nanometers are required. Many approaches have been employed to create nanoporous separators, including the use of ordered templates,[35] carbon nanotubes,[36] and various composite nanofibers.[37–40] However, applications are typically for aqueous solutions used in biomolecule separation

and water treatment.[41,42] Recently, Tung et al. described an aramid nanofiber based composite produced using a layer-by-layer technique for lithium ion batteries.[43] Pore sizes in these materials are tunable and separators with nanoporosity approaching the pore sizes required for NAqRFB applications were demonstrated. The aramid nanofibers also offer high strength and could provide ultrathin separators with minimal resistance.

In this chapter, we explore the feasibility of using aramid nanofiber (ANF) based films as separators in NAqRFBs. Films with pore sizes relevant for use in NaqRFBs are fabricated using a spin coating assisted layer-by-layer (LBL) technique. The permeability, conductivity, stability, and flow cell performance of the ANF separators are compared to those for Celgard 2325 and Neosepta AHA (Neosepta), an anion exchange membrane. A polyelectrolyte layer-by-layer coating based on poly(diallydimethylammonium chloride) and poly(styrene sulfonate) is also evaluated as potential surface modification technique to further increase the selectivity of these ANF separators. For this work, vanadium acetylacetonate ($V(acac)_3$), a well-studied metal coordination complex for NAqRFBs[10,18,23,24,27,44], is used as a model active species with acetonitrile as the solvent. Although $V(acac)_3$ is unattractive for implementation, it was selected due to its commercial availability and more importantly its similar size to a variety of other promising active species, ensuring the results can be easily translated to more advanced active species system as they emerge. Overall, this works offers a strategy for the development of size-selective nanoporous separators for more efficient RFBs and presents a surface modification approach that can be used to further enhance the performance of nanoporous separators.

3.2 Material and Methods

This section describes the materials and experimental techniques used in this work.

3.2.1 Preparation of ANF separators

A 1 wt% ANF dispersion was prepared following the protocol developed by Ming et al.[45] For the neat ANF separators, 1 mL of the ANF dispersion was spin coated onto a glass slide at 1000 rpm for 30 seconds. The coated glass slide was then dipped into a water bath to remove the DMSO and KOH from the dispersion, thus forming a thin ANF hydrogel on the glass. The sample was then dried at 70 °C for 30 minutes. This process was repeated 20 times in order to build up a 8.5 μm film. Free-standing samples were obtained by chemically etching the glass slide using 0.5% HF solution. The samples were washed extensively in ethanol and then DI water until the rinse water pH was neutral.

3.2.2 Surface Modification of ANF separators using polyelectrolytes

1% Poly(diallydimethylammonium chloride) solution (20wt% in water, average Mw 400,000 – 500,000, Sigma Aldrich) and 1% Poly(Styrene Sulfonate) solution (average Mw ~1,000,000, Sigma Aldrich) are prepared using DI water. ANF separators are first dipped in the 1% PDDA for 5 mins, rinsed in DI water for 1 min, air dried and then dipped into the 1% PSS for 5 min. The sample then again rinsed in DI water and air dried. This cycle is repeated for 5 times for $(PDDA/PSS)_5$ on ANF and 20 times for $(PDDA/PSS)_{20}$ on ANF. Free standing samples were then obtained using the same glass etching procedures as the neat ANF samples. All PDDA/PSS coated samples are soaked in 0.1M $TBABF_4$ ACN solution for at least 10 days before testing. This is to remove the Na^+ and Cl^- ions from the samples.

3.2.3 Pore Size Evaluation

Mercury intrusion porosimetry was conducted using a Micromeritics AutoPore IV 9500 Series mercury intrusion porosimeter. N_2 physiosorption was conducted using a Micromeritics ASAP 2020 Accerlerated Surface Area and Porosimetry System. The pore size presented are estimated from the N_2 desorption curve.

3.2.4 Ionic Conductivity Experiments

Ionic conductivity was determined using electrochemical impedance spectroscopy (EIS). 20 mm diameter samples were soaked in 0.1 M $TBABF_4$ (≥ 99.0%, Sigma Aldrich) in acetonitrile (ACN) (99.9+%, Extra Dry, AcroSeal™, ACROS Organics™), solution for at least 72 hours before measurement. The samples were assembled into an EL-Cell (ECC-Std, EL-CELL® GmbH) with 100 µL 0.1M $TBABF_4$ in ACN. The assembly is allowed to equilibrate for 30 min before a measurement. EIS results were fitted with a basic semi-circle fit, where the high-frequency intercept was taken as the solution resistance. The solution resistance was used, along with electrode area and sample thickness, to calculate the ionic conductivity.

3.2.5 $V(acac)_3$ Permeability Experiments

The samples were assembled into an H-Cell setup (Adam & Chittenden Scientific Glass). 7 mL of 0.05 M $V(acac)_3$ (Strem Chemical Inc.) and 0.1 M $TBABF_4$ ACN solution was placed in one compartment of the cell and 7 mL of 0.1 M $TBABF_4$ ACN solution was placed in the other compartment. The cell was constantly stirred with micro magnetic stir bars. The $V(acac)_3$ concentration in the pure supporting electrolyte side was monitored over time using UV-Vis spectroscopy. The permeability of the separator was then calculated using the equation below:

$$V\frac{dC_t}{dt} = A\frac{P}{L}(C_0 - C_t) \quad (1)$$

Where *V*, *A*, *L* and *P* are the volume of the cell, separator area, separator thickness and $V(acac)_3$ permeability of the sample, respectively.

The permeability for A-TEMPO and Ferrocene was conducted with the same experimental conditions with the concentration monitored using the square wave voltammetry (SWV). The concentration of the active materials in the pure supporting electrolyte side was calculated from the peak height from SWV using the following equation.

$$\Delta i_p = \frac{nFAD_0^{1/2}C_0^*}{(\pi t_p)^{1/2}}\Delta\Psi_p \quad (2)$$

Where $\Delta\Psi_p$ is set to 0.9281 based on the operating parameters recommended in literature. F, A, n, are the Faraday constant, electrode area, and number of electrons transferred respectively.

3.2.6 ANF Stability experiments

The tip of a glassy carbon (GC) electrode (area 0.07cm^2, BASi) is coated with a 1% ANF dispersion. The GC electrode is then dipped into water to remove the DMSO and KOH, leaving a layer of ANF hydrogel on the tip. The samples are then dried at 80 ˚C overnight to remove any water. PDDA, PSS and PDDA/PSS are later added on top of the dried ANF coating using a layer-by-layer technique. The coated electrodes are soaked in 0.1 M $TBABF_4$ in ACN solution for at least 72 hours before use. At the start of the stability measurement, the coated electrodes are inserted into a 3 electrode electrochemical cell with a 0.0 1M $V(acac)_3$ and 0.1 M $TBABF_4$ in ACN electrolyte. The electrode and solution are kept in contact for 10 days before the CV is conducted.

3.2.7 Charge/Discharge Experiments in H-Cells

The samples were assembled in an H-Cell setup (Adam & Chittenden Scientific Glass) and controlled using a Maccor battery tester. For the symmetric $V(acac)_3$ experiments, 5 mL of 0.05 M $V(acac)_3$ and 0.3 M $TBABF_4$ ACN solution were added to each side of the cell. Graphite plate electrodes (pretreated at 500 ˚C for 10 hours under nitrogen to remove any surface oxygen groups) were used and electrode sizes were measured before each run to ensure a current density of ~ 0.25 mA cm^{-2} at C/5. An Ag/Ag+ reference electrode was placed next to the positive electrode to provide accurate voltage cutoffs. Voltage cutoffs were based on the positive electrode voltage and were set at 0.5 V on charge and 0.02 V on discharge. An additional state of charge cutoff was set at 50 %. The electrolytes were constantly stirred during the charge/discharge experiment.

3.2.8 Charge/Discharge Experiments in Flow Cells

Custom flow cells with interdigitated graphite flow fields and polypropylene backing plates are used for all cycling experiments.[46] Carbon paper is used as the electrode (SGL Group, 29 AA), with two pieces inserted on either side of Neosepta, Celgard 2325, ANF, or coated ANF. Polytetrafluoroethylene gasket tape (GORE PTFE Sealant, Gallagher Fluid Seals Inc.) is used to seal the cell at ~20% electrode compression. During cycling, two glass 10 mL reservoirs are filled with electrolyte (0.05M $V(acac)_3$/0.5M TBABF4/ACN) and the fluid is pumped through the cell using a peristaltic pump at 10 mL/min. The cell is cycled at C/5 (~1mA/cm^2) with voltage cutoffs at 1.4 V and 2.2 V, and a coulombic limit of 80% SOC. The voltage cutoffs were determined from the cyclic voltammogram of $V(acac)_3$.

3.3 Results

This section describes the properties found in the nanoporous ANF separators.

3.3.1 Fabrication and Structure

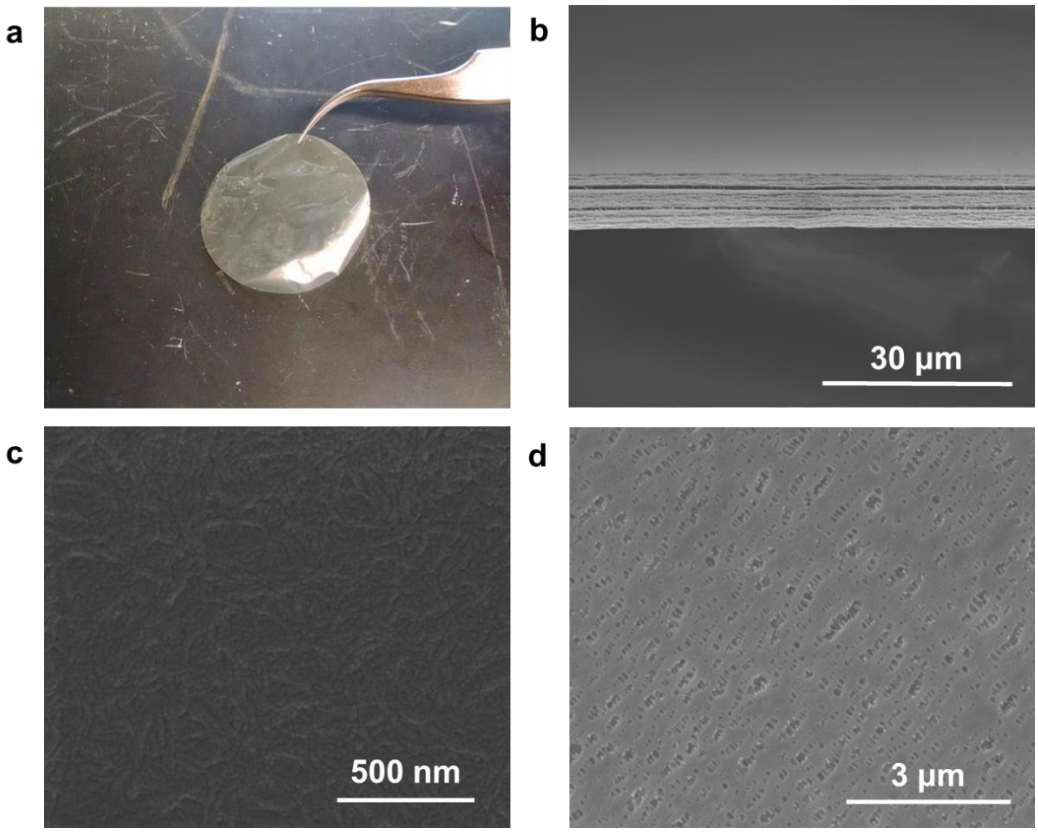

Figure 3-1 (a) Optical Image of a ANF separator; (b) Cross sectional SEM image of the ANF Separator; (c) SEM image of the surface of an ANF Separator;(d)) SEM image of the surface of Celgard 2325

A spin coating assisted layer-by-layer (LBL) technique is used to fabricate the ANF separators. Composites made using LBL have previously shown exceptional uniformity and mechanical performance.[47] By utilizing spin coating in conjunction with LBL, films with varying pore sizes can be quickly assembled while maintaining the uniformity and control that LBL provides.[48] An 8.5 µm thick free-standing film is obtained by assembling 20 layers of ANF. Each layer of ANF deposited is estimated to be 425 nm thick. Layers of ANF, or ANF mats, are stacked together to form the separator. This multilayer structure, in conjunction with the dense network of nanofibers comprising each layer, reduces the effective pore size of the separator while maintaining networks of pores for ionic

conductivity. The transparency and smoothness indicate the homogeneity of the samples (Figure 3-1a). Their uniform thickness and the homogeneity can be further observed using scanning electron microscopy (Figure 3-1b). In Fourier transform infrared (FTIR) spectra of the ANF separator, the molecular structure matches that of previously reported ANF work (Figure 3-2). Nanosized pores are observed on the surface of the separator using SEM (Figure 3-1c), while N_2 physisorption and mercury intrusion porosimetry estimate the average pore size to be 5 nm (Figure 3-3). These pores are considerably smaller than the 28 nm pores present for Celgard 2325 (Figure 3-1d) and as a result are expected to significantly reduce the transport rates of nanosized active species. To quantify the effect of these morphological differences, relevant physical properties, including permeability and conductivity, were measured.

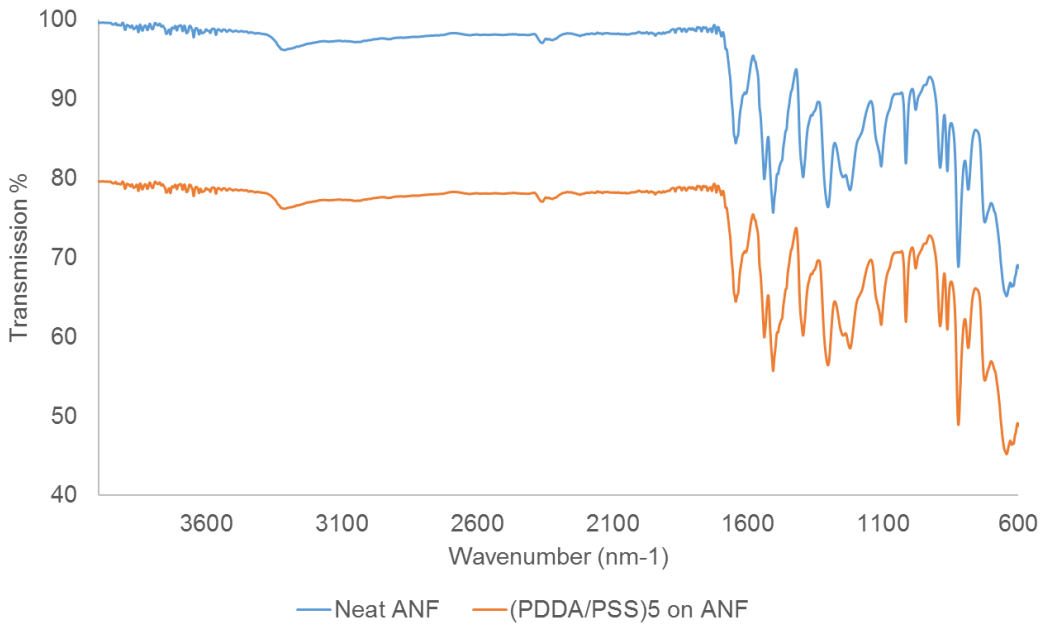

Figure 3-2 FTIR Spectra of Neat ANF and $(PDDA/PSS)_5$ on ANF

3.3.2 Permeability and Conductivity

A H-type cell is used to determine the permeability of $V(acac)_3$ through the separators by measuring the concentration of $V(acac)_3$ in each of the cell chambers as a function of time using UV-Vis spectroscopy. The ANF and Celgard 2325 materials do not appear to interact with $V(acac)_3$ as the absorbance peaks (298 and 343 nm) are identical (Figure 3-2). The concentration versus time plots are obtained by monitoring changes in the absorbance of the peak at 298 nm (Figure 3-4 insert). The two chambers separated by Celgard 2325 completely equilibrated within 5 hours, while the ANF separated chambers took more than 12 hours to equilibrate. This significant improvement in the crossover rate is reflected in the permeability of $V(acac)_3$ (equation provided in the experimental), which is an order of magnitude lower for ANF than for Celgard 2325 (Table 3-1). For Neosepta, complete equilibration was never observed even after 5 days (120 hrs), however, later results will demonstrate the incompatibility of Neosepta with acetonitrile.

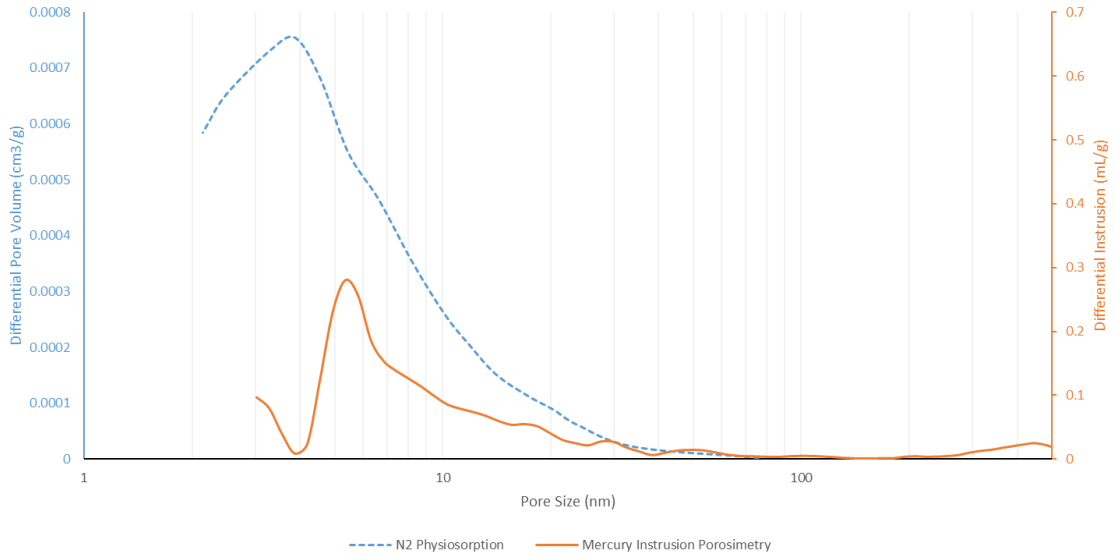

Figure 3-3 Pore size distribution of Neat ANF Separator using N2 physiosorption and Mercury Intrusion Porosimetry

For RFB applications, it is important to allow transport of the supporting electrolyte ions while preventing active species crossover. For the purposes of this work, tetrabutylammonium tetrafluoroborate ($TBABF_4$) is used as the supporting electrolyte and the ionic conductivities of the various separators/membranes are measured using electrochemical impedance spectroscopy. All of the samples were soaked in 0.1 M $TBABF_4$/acetonitrile solution for 10 days prior to the conductivity measurements. No evidence of swelling is observed for either material, indicating their dimensional stabilities. The ANF separator exhibits an ionic conductivity of 0.10 mS/cm, five times less than that for the Celgard 2325 separator (Table 3-1). This result is not unexpected given the reduced pore size, which impedes ion mobility.

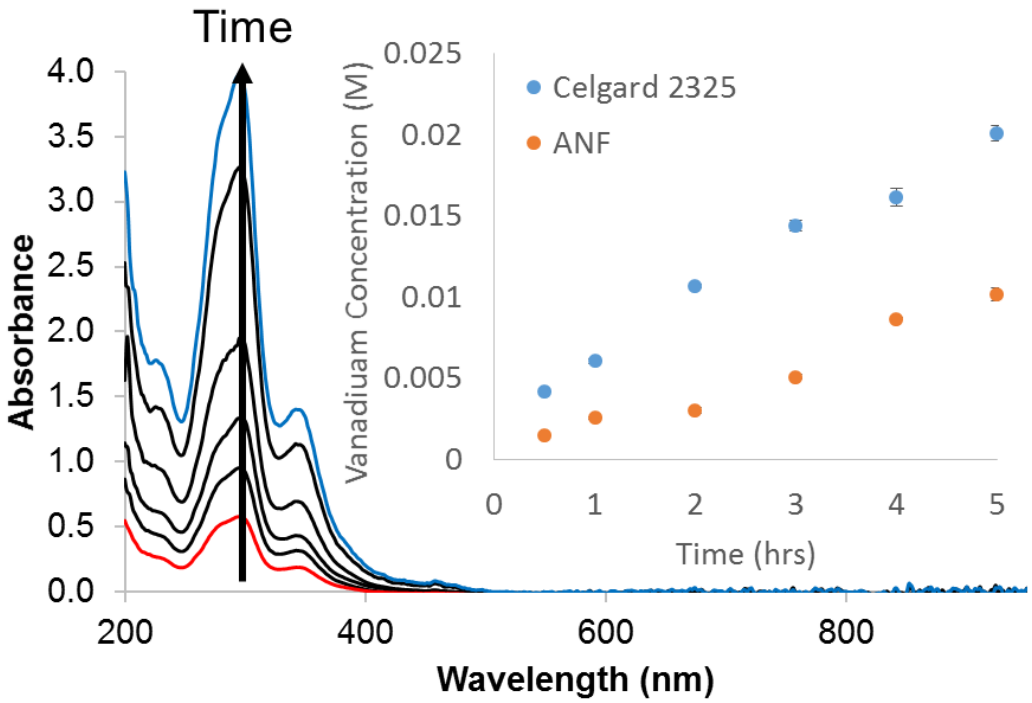

Figure 3-4 UV-Vis Spectra of $V(acac)_3$ crossover in Celgard 2325 H-Type Cell; Insert: Concentration over time curve of Celgard 2325 and ANF

ANF is also compared to Neosepta, a commonly used NAqRFB AEM (Table 1). In comparison, ANF exhibits a 5 times higher ionic conductivity and an order of magnitude higher permeability. This difference in performance is due to the ionic conducting mechanisms in separators versus membranes. In separators, like ANF, ionic conductivity is achieved through the liquid electrolyte impregnated in its nanosized pores. In membranes, like Neosepta, ions are conducted in the solid phase via channels formed by charged pendant group on the polymer chains. Therefore, ANF offers higher ionic conductivity as a result of liquid ion conduction and Neosepta offers lower permeability due to its solid polymeric structure. In this case, high conductivity and low permeability would seem to be contradicting properties, where a gain in the conductivity would imply an increase in permeability and vice versa. However, motivated by theoretical studies in nanofluidic transport[49], we believe that addition of highly charged surface functional groups can further lower permeability without sacrificing conductivity.

Table 3-1 Permeability and Conductivity of Celgard 2325, Neospeta AHA, ANF and Coated ANF samples.

Sample	Permeability ($x10^{-7}$ cm^2s^{-1})	Conductivity (mS/cm)
Celgard 2325	7.22	0.59
Neosepta AHA	0.03	0.02
ANF	0.82	0.10
$(PDDA/PSS)_5$ on ANF	0.003	0.10
$(PDDA/PSS)_{20}$ on ANF	0.003	0.04

3.3.3 Polyelectrolyte Surface Modification

While we observed decreased permeability of $V(acac)_3$ using the neat ANF separator, the permeability remains insufficient for a practical RFB. Studies in nanofluidic transport have suggested that surface charges [E(y)] play an important role in the transport of the solute

through a nano-sized channel[49]. The equation below describes the solute partition coefficient Φ, the ratio between the concentration of solute within a nanopore, <c> and that in the bulk solution, c_0.

$$\Phi = \frac{\langle c \rangle}{c_0} = \frac{1}{h}\int_0^{h-r} \exp(-E(y)/kT)dy \quad (3)$$

If only steric exclusion is considered [E(y) = 0], the equation reduces to Φ=(1-r/h), where r is the radius of the solute and h is the radius of the pore. If we considered the size of the pores in the neat ANF (h_{ANF}=25Å) , Celgard 2325($h_{Celgard2325}$=140Å) and V(acac)$_3$ ($r_{V(acac)3}$ = 5Å), we can see that Φ_{ANF} = 0.8 while $\Phi_{Celgard\ 2325} \approx 1$. While this result explains the decreased permeability observed in the neat ANF compared to Celgard 2325, it also reveals an opportunity where incorporating strong surface charges in ANF may further decrease the solute partion coefficient Φ.

Poly(diallydimethylammonium chloride) (PDDA), a strong polycation, and poly(styrene sulfonate) (PSS), a strong polyanion and polyethyleneimine (PEI), a branched weak polycation are identified as potential candidates to add additional charge selective group to the ANF material, forming a composite. The concept of highly charged selective surface layers for flow batteries has been proposed by Shin et al. [8] , and has been demonstrated in Aq RFBs using nafion membranes[50] and NAqRFBs using polyolefin microporous separators[28] as substrates. Different ANF/polyelectrolyte composites were constructed with PDDA, PSS and PEI. The polyelectrolytes were either incorporated throughout the bulk of the composite, as a surface coating or as a layer-by-layer coating on the surface. Figure 3-5 summarizes the permeability and conductivity of the samples made.

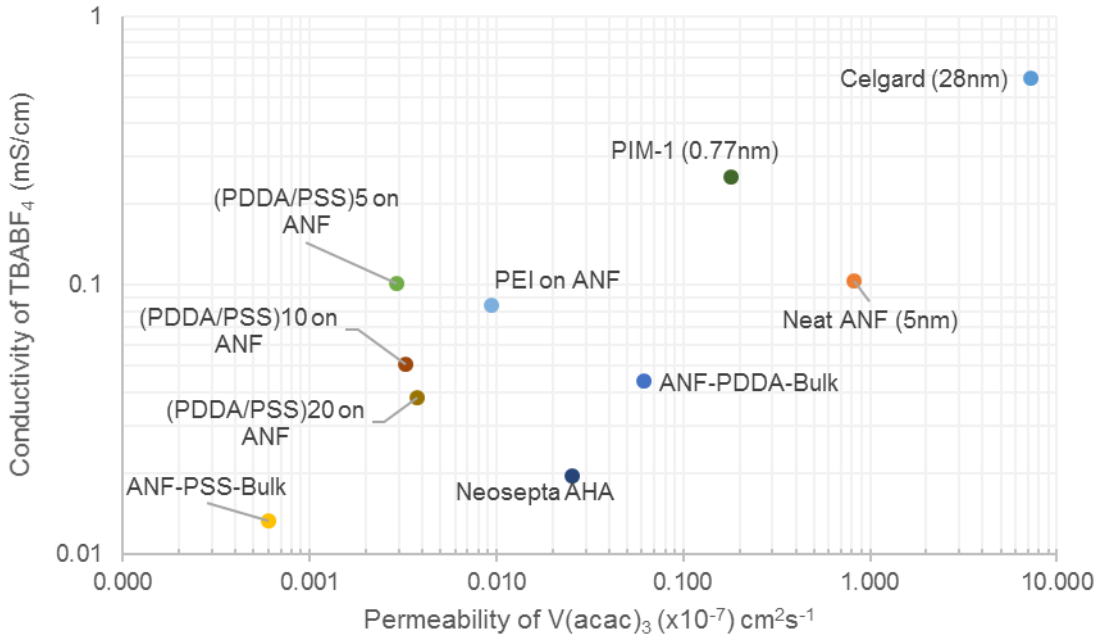

Figure 3-5 Permeability and conductivity summary of ANF Composites made, compared to Celgard, PIM-1, and Neosepta AHA

Bulk addition of PDDA (ANF-PDDA-Bulk) and PSS (ANF-PSS-Bulk) with ANF yielded the most dramatic effect on the permeability (Figure 3-5). However, with the decreased permeability of $V(acac)_3$, the conductivity also suffered. Surface coatings such as PEI on ANF, or layer-by-layer coatings of $(PDDA/PSS)_n$ exhibited much better independent control over permeability with minimal effects on conductivity. It is worth noting that we were able to obtain PIM-1 membranes, which were described in the polysulfide-blocking application[33], from our collaborators and tested them in our $V(acac)_3$ acetonitrile system. While the reported pore size of the PIM-1 membrane would suggest very effective $V(acac)_3$ separation, the membrane only exhibited slightly lower permeability compared to neat ANF. This is most likely due the swelling observed of PIM-1 in acetonitrile, causing the pores to swell beyond the reported pore size value. After surveying the various samples, layer-by-layer coatings of $(PDDA/PSS)_n$ on ANF were identified as the most promising

candidates for further investigation since it exhibited the lowest permeability while retaining conductivity comparable as neat ANF.

SEM imaging of the coated surface shows a smooth morphology (Figure 3-6a) compared to neat ANF (Figure 3-1c) and EDAX elemental analysis shows Na, S and Cl signals, which can be attributed to PDDA and PSS (Figure 3-6b), confirming the deposition of coating. FTIR measurements of $(PDDA/PSS)_5$ on ANF, with the subscript denoting 5 bilayers of PDDA/PSS deposited onto an ANF separator, yield an identical signal as the neat ANF (Figure 3-2). This illustrates that the deposited amounts are relatively small and do not alter the bulk of the ANF separator, although it is also due in part to the overlap between the characteristic vibrations for ANF, and PSS and PDDA. For example, sulfonate (-SO3) stretching vibrations from PSS overlap with the Ph-N vibrations from ANF.

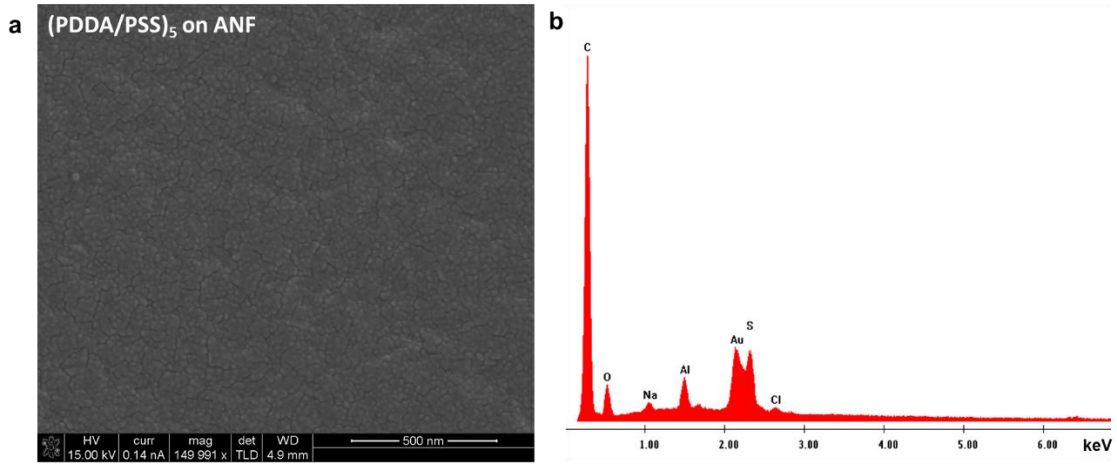

Figure 3-6 (a) SEM image of the surface of $(PDDA/PSS)_5$ on ANF; (b) EDAX Spectra of the surface of $(PDDA/PSS)_5$ on ANF

By depositing five bilayers of PDDA/PSS coating on the surface of the ANF separator the permeability of $V(acac)_3$ is reduced by two orders of magnitude compared to neat ANF, while the conductivity of $TBABF_4$ remains relatively the same at 0.1 mS/cm. Increased

deposition of 20 PDDA/PSS bilayers showed a very similar $V(acac)_3$ permeability, but the conductivity is reduced by an order of magnitude (Table 1). This illustrates that there is an optimum number of PDDA/PSS bilayers required to effectively reduce the permeability of the larger $V(acac)_3$ molecules while retaining similar transport properties for the smaller $TBABF_4$ ions. When compared to the anion exchange membrane, Neosepta, $(PDDA/PSS)_5$ on ANF show 10x lower $V(acac)_3$ permeability while showing 5x higher conductivity. This reduction in permeability without sacrificing conductivity represents a powerful opportunity to increase efficiencies in RFBs without negatively affecting the power density.

3.3.4 Chemical Stability

To achieve extended cycling and long lifetimes, the active species, supporting electrolytes and separator materials should not interact irreversibly. The chemical stability of ANF in acetonitrile solutions of $V(acac)_3$ is evaluated using cyclic voltammetry (CV). Glassy carbon electrodes are coated with ANF, $(PDDA)_5$ on ANF, $(PSS)_5$ on ANF and $(PDDA/PSS)_5$ on ANF. These electrodes are then soaked in separate 0.01 M $V(acac)_3$/0.1 M $TBABF_4$/acetonitrile solutions. CV measurements are conducted after 10 days of contact (Figure 3-7). The CV for neat ANF showed typical features of $V(acac)_3$ with redox potentials at 0.4 V and -1.8 V. The redox couple at 0.6 V, which is attributed to $VO(acac)_2$, is also observed[10]. No new redox activity is observed indicating ANF is stable within the voltage window of $V(acac)_3$ and no interactions between ANF and $V(acac)_3$ can be observed electrochemically. Similarly for the $(PDDA)_5$, $(PSS)_5$ and $(PDDA/PSS)_5$ coated electrodes, no electrochemical instabilities are observed for either PDDA, PSS or the combination of both. This confirms that the components are stable within the operating

voltage window of the $V(acac)_3$ system. Slight changes in the peak heights are also observed for the coated electrodes, which is due to a difference in $V(acac)_3$ transport characteristics through the PDDA and PSS containing films. The decreased permeability of $V(acac)_3$ through the $(PDDA/PSS)_5$ separator results in a lower total current for the coated electrodes than for neat ANF as less $V(acac)_3$ can reach the glassy carbon surface through the coating.

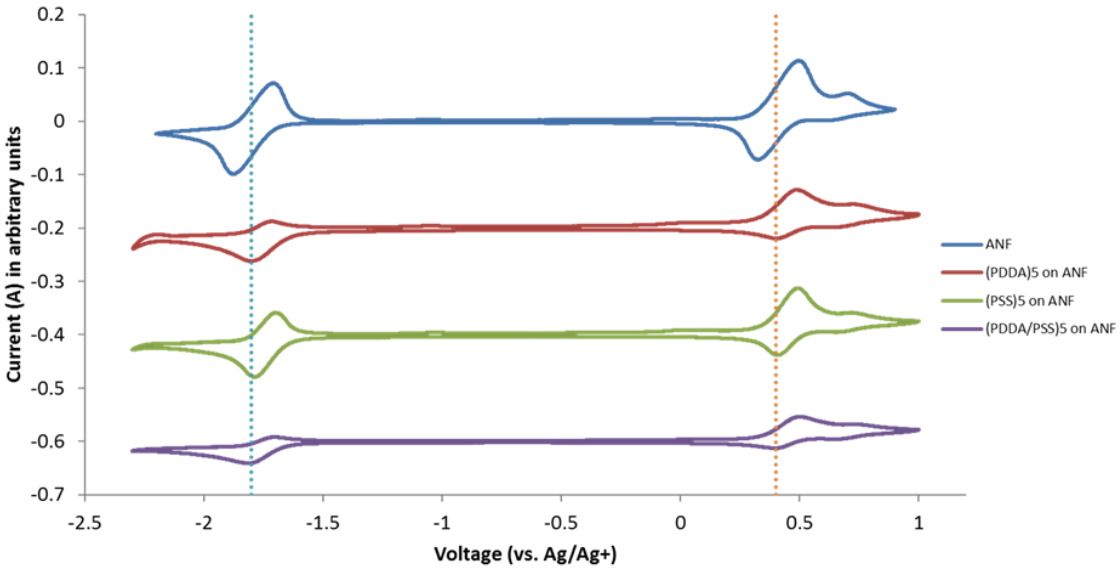

Figure 3-7 Cyclic Voltammagram of ANF Coated glassy carbon electrodes after soaking in 0.01M $V(acac)_3$ 0.1M $TBABF_4$ ACN Solution for 5 days. 100mV/s, 5th cycle shown.

3.3.5 Charge/Discharge Experiments in H-Cells

The performance of the ANF separators was compared to that for Celgard using charge/discharge experiments performed in H-type cells. $V(acac)_3$ exhibits two reversible redox events at -1.8 V and 0.4 V vs. Ag/Ag+, making it a viable candidate for a NAqRFB.[18] The cells were cycled at C/5 ($0.25mA/cm^2$) which takes 2.5 hours to charge and discharge to 50% SOC.[1] A Ag/Ag+ reference was placed in the positive electrode chamber and used

to implement a cutoff voltage of 0.5V during charging to suppress $VO(acac)_2$ formation. This was coupled with a 50% SOC cutoff. A reference electrode was not needed in the anolyte chamber due to the relative stability of the negative couple.[51]

During charge/discharge, similar voltage profiles were observed for cells containing the ANF and Celgard separators (Figure 3-8a and Figure 3-8b, respectively). The average plateau voltage for both cells was 2.4V, which corresponds closely to the potential difference (2.2V) between the positive and negative redox couples of $V(acac)_3$. The observed overpotentials were primarily a result of the large separation (>4cm) between the negative and positive in the H-cell configuration. The slightly higher overpotentials observed for the ANF cell are likely consequence of its lower ionic conductivity.

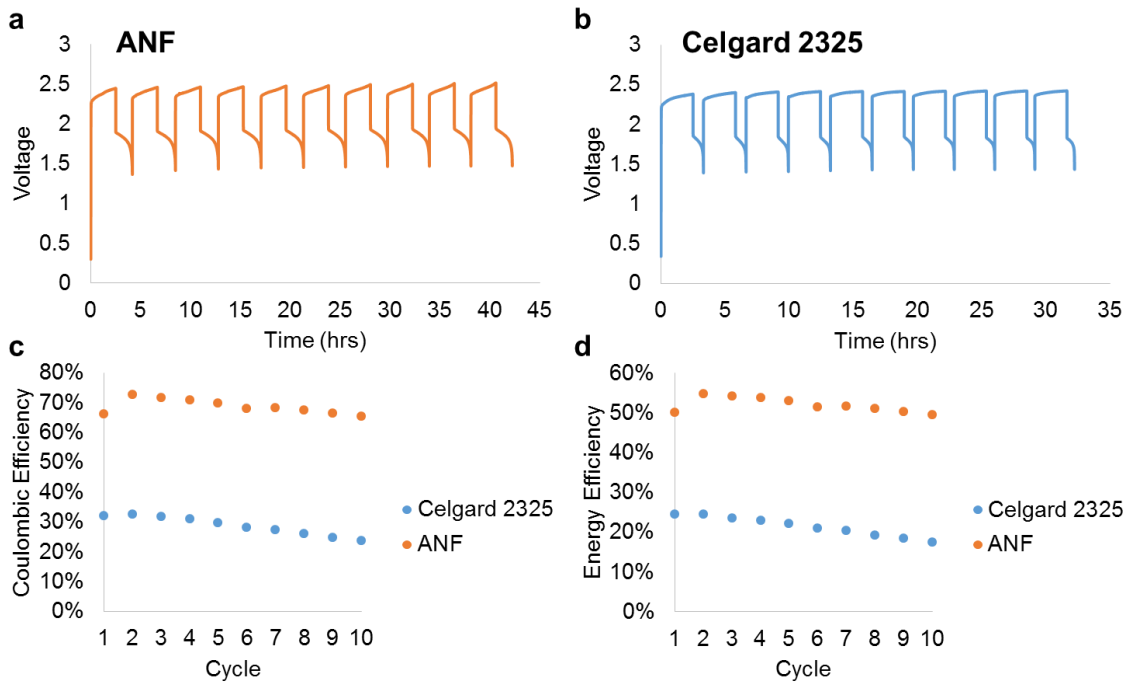

Figure 3-8 Voltage profiles for (a) Celgard 2325 and (b) ANF separators during charge/discharge experiments. (c) Coulombic efficiencies and (d) energy efficiencies as a function of cycle number for Celgard 2325 and ANF separators.

Coulombic efficiencies (CE) and energy efficiencies (EE) for the ANF and Celgard containing cells are illustrated in Figure 3-8c and d, respectively. Comparing the performance of the ANF separator to that of Celgard, the CE and EE were improved by 139% and 140%, respectively. The improvement in CE is due to the ANF separators smaller pore size and higher transport selectivity. Similarly, the EE was enhanced for the ANF separator due to the significant reduction in permeability, which outweighs the decreased ionic conductivity. These significant enhancements in performance were achieved despite a relatively low solute partition coefficient ($\Phi_{ANF} = 0.8$).

A gradual decrease in CE and EE is observed for the ANF and Celgard 2325 containing cells, which is the result of $VO(acac)_2$ formation.[23] The capacity retention is 90% and 72% of the maximum capacity (2^{nd} cycle) at the end of 10 cycles for ANF and Celgard 2325 cells. We believe the higher capacity fade observed for the Celgard 2325 cell is due to an increasing degree of crossover with cycling. The rate of crossover will increase when steeper chemical gradients are formed as the amount of charged species ($[V(acac)_3]^+$ and $[V(acac)_3]^-$) on each side of the separator accumulates with cycling. The capacity retention in the ANF cell is therefore better because of its lower $V(acac)_3$ permeability. The capacity fade is also a consequence of $VO(acac)_2$ formation. Overall, we believe the contribution of $VO(acac)_2$ formation on the separator to the capacity fade is minor compared to the increased crossover. This is supported by the higher capacity retention of ANF cells compared to Celgard 2325. The results indicate that the principal limitation of all-$V(acac)_3$ cells is the instability of the active species at the positive electrode, which can be addressed through the continued redox active molecule research.

Similar H-Cell experiments were also performed with the polyelectrolyte/ANF composites with markedly lower permeability. The CE were extracted from the charge/discharge experiments and plotted against the permeability of the sample (Figure 3-9). Neosepta AHA and ANF-PSS-Bulk samples exhibited significant overpotentials exceeding the limits of the Maccor battery tester and were therefore left out of the plot. PIM-1 membrane samples showed rapid capacity fade, developing brittleness and failure after short periods of cycling. It is likely that material incompatibility between $V(acac)_3$, ACN and the PIM material likely caused these observations and failures.

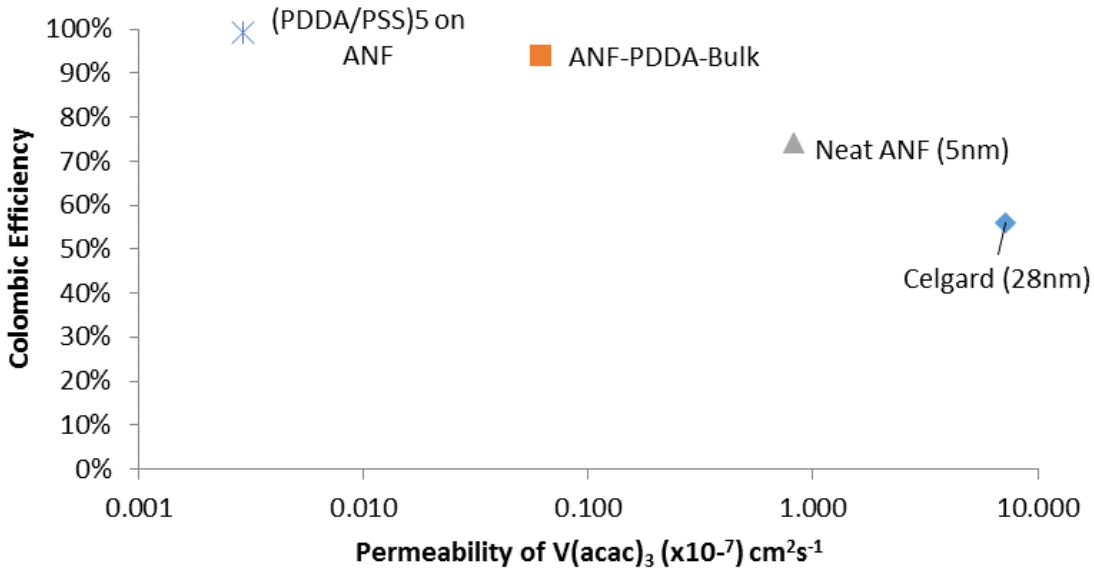

Figure 3-9 Coulombic Efficiency versus Permeability of Separator Samples tested in H-Type Cells. 0.05M $V(acac)_3$ 0.3MTBABF$_4$ acetonitrile catholytes and anolytes solutions. C/5 (~0.25mA/cm^2) charge/discharge rates used.

From Figure 3-9, we can observe a strong dependency between permeability and coulombic efficiency. The decreased permeability in ANF-PDDA-Bulk and $(PDDA/PSS)_5$ on ANF resulted in significant improvements in CE to 94% and 99%, respectively. However, the non-linear relationship between permeability and CE also suggests that

further improvements in CE will require multiple orders of magnitude of decrease in permeability.

3.3.6 Charge/Discharge Experiments in Flow Cells

To demonstrate the impact of the lowered permeability and increased stability of the ANF based separators, flow cells were assembled using Celgard 2325, Neosepta, neat ANF and $(PDDA/PSS)_5$ on ANF as the separator/membrane with $V(acac)_3$ serving as both the catholyte and anolyte active species. The cells were cycled to 50% state-of-charge at C/5 (~1mA/cm^2), providing sufficient time per cycle to observe crossover effects. At these conditions, with complete electrolyte separation, $V(acac)_3$ is expected to demonstrate stable cycling performance for over 20 cycles.[51] Crossover is expected to decrease this lifetime due to the irreversible formation of $VO(acac)_2$ in the catholyte chamber.

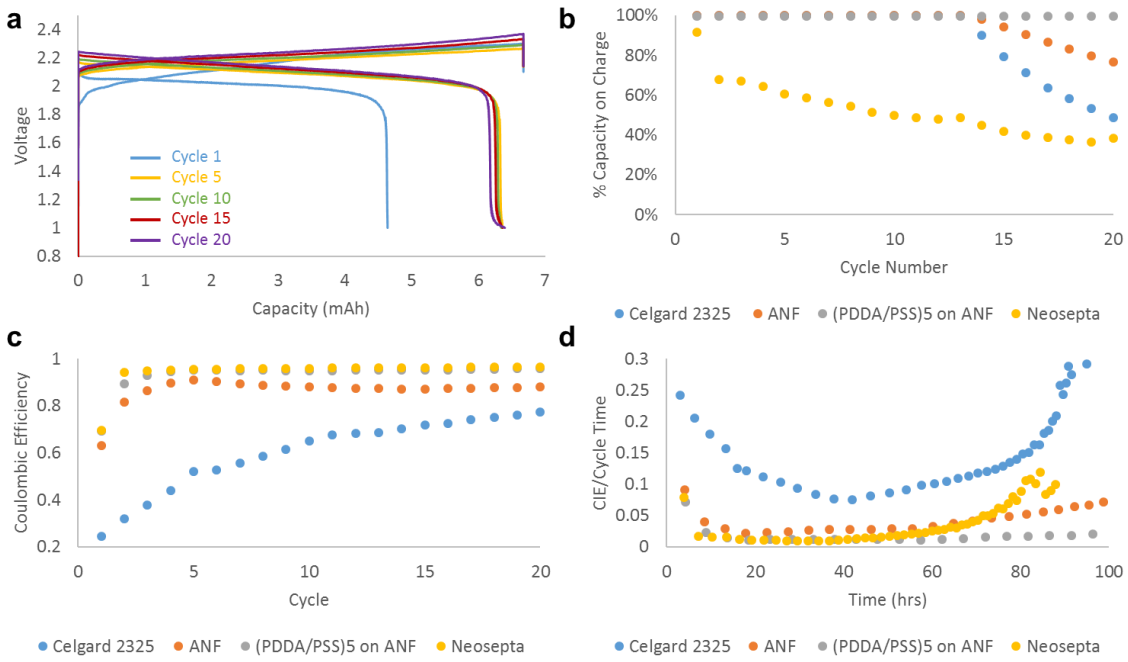

Figure 3-10 (a) Voltage profiles for an all-$V(acac)_3$ flow cell with (PDDA/PSS)5 on ANF as the separator; (b) charge capacity per cycle normalized to the capacity accessed in the first cycle for Celgard 2325, ANF, $(PDDA/PSS)_5$ on ANF and Neosepta; (c) coulombic efficiencies per cycle; (d)

CIE/cycle time plotted against total time comparing the degradation rates of each separator/membrane material.

Voltage profiles of $(PDDA/PSS)_5$ on ANF (Figure 3-10a), along with that of the other flow cells (Figure 3-11) show an average discharge plateau of 2.2V. This matches the expectation based on the cyclic voltammogram of $V(acac)_3$ (Figure 3-12). Figure 3-10b shows the charge capacity versus cycle number. For Celgard 2325, capacity fade reaches 80% of the initial capacity by cycle 15 while that for ANF separator occurs at cycle 19. Neosepta shows rapid capacity fade starting from the first cycle and is well below 80% initial capacity by the second cycle. Finally, for the $(PDDA/PSS)_5$ on ANF, capacity fade is not observed over the full 20 cycles, which corresponds to nearly 100 hours of continuous stable operation. This is a confirmation of the stability of the $(PDDA/PSS)_5$ on ANF observed in the coated electrode experiments. The capacity fade observed for bare ANF, and more severely for Celgard 2325, is due to accelerated degradation from $V(acac)_3$ crossover. The rapid fade seen with Neosepta is thought to be due to material incompatibility rather than crossover, due to its low permeability.

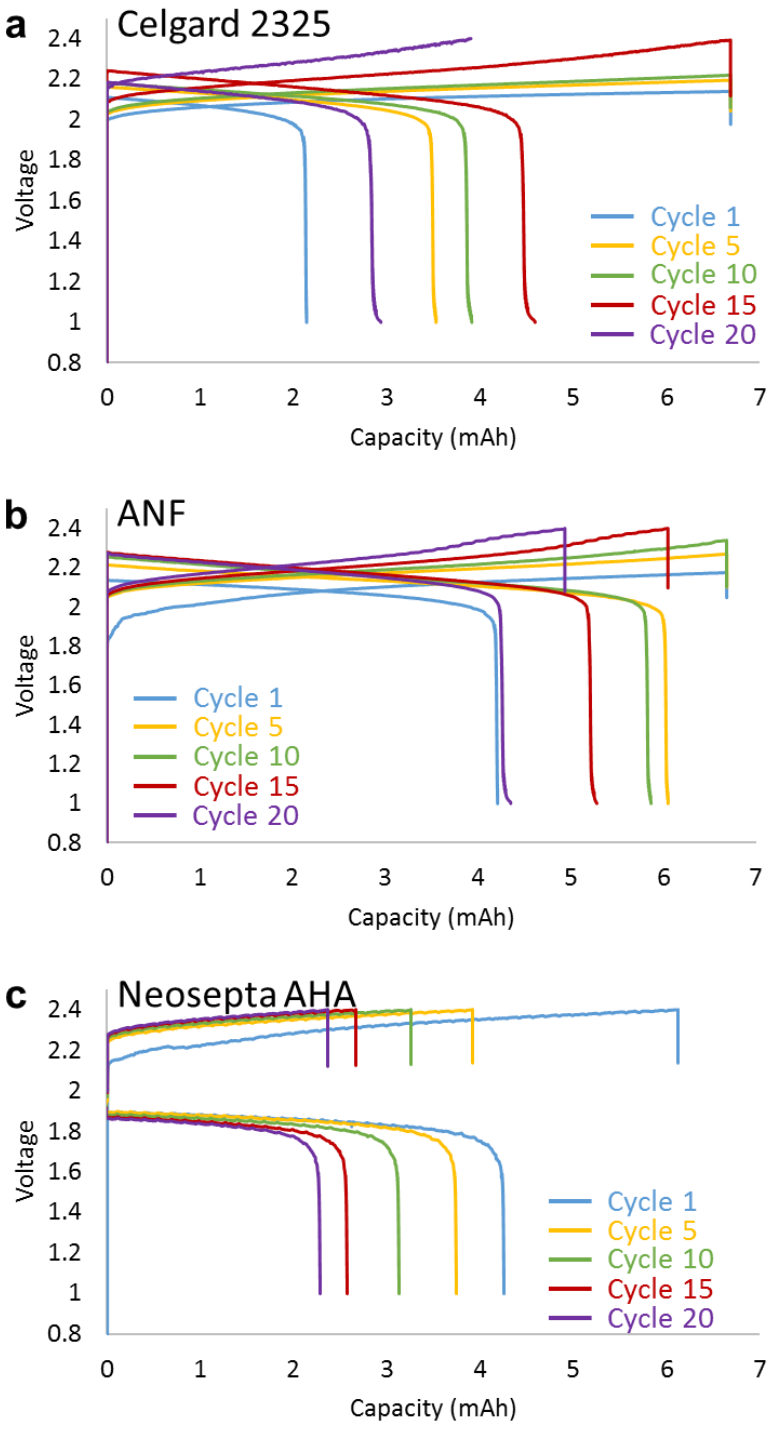

Figure 3-11 Voltage profile of flow cells with (a) Celgard 2325, (b) ANF, and (c) Neosepta AHA as separator/membrane.

The coulombic efficiency of the flow cells with Celgard 2325, Neosepta, ANF and $(PDDA/PSS)_5$ on ANF were found to be 55%, 70%, 88%, and 95% respectively when averaged over the cycles before 80% initial capacity (Figure 3-10c). Similar voltaic efficiencies were observed for all samples (82-87%), with the exception of Neosepta (76%), which was lower due to its thickness and poor conductivity (Table 2). While Neosepta exhibited a fairly high CE, note that it also showed the most dramatic capacity fade, suggesting incompatibility with the non-aqueous media. The CE for Celgard 2325 trended upwards over the 20 cycles as a result of continuous capacity fade, and therefore shortened cycling times, observed over the course of the experiment. Since crossover is a zero-order time dependent process, the amount of crossover in a single cycle decreases with shortened cycle time.

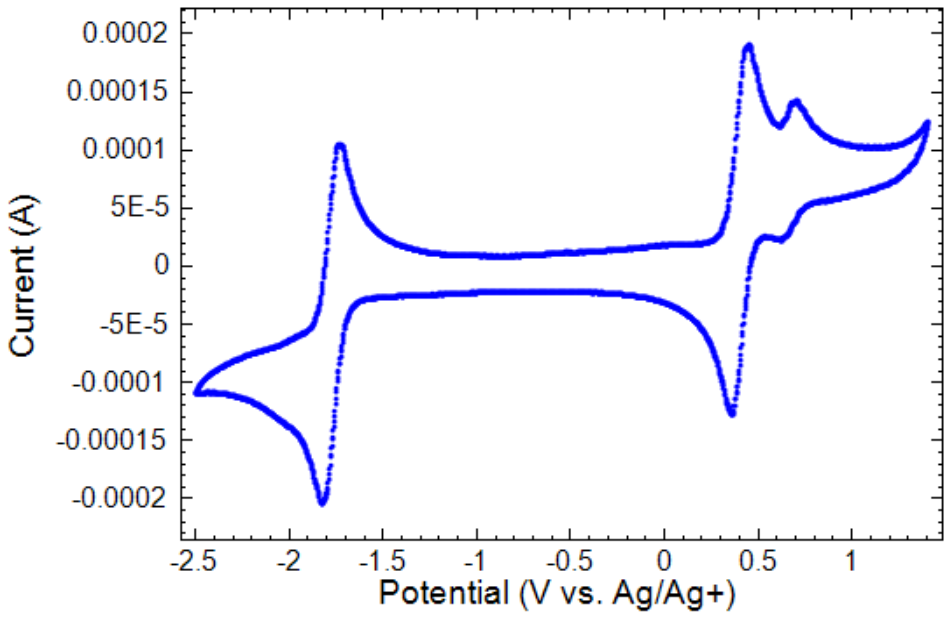

Figure 3-12 Cyclic Voltammogram of 10mM $V(acac)_3$, 500mM $TBFBF_4$ in Acetonitrile. 100mV/s. 5th Cycle shown

To remove the time contribution on the CE parameter and gain a better understanding of the crossover and degradation effects in the flow cells, the coulombic inefficiency (CIE = 1-CE) divided by cycle time is calculated. This parameter was originally used by Smith et al. to compare parasitic reaction rates in lithium ion batteries at different C-rates.[52] The CIE/cycle time metric can also be viewed as a zero-order cell degradation rate. For example, a crossover process with negligible degradation would be a zero-order reaction and therefore exhibit a constant CIE/cycle time versus time. While this metric cannot be used to identify the exact cause of degradation, it is useful in comparing the degradation rates between different cell materials. Over a total of 100 hours of cycling, $(PDDA/PSS)_5$ on ANF exhibited the lowest degradation rates followed by Neosepta, ANF and Celgard 2325 (Figure 3-10d). $(PDDA/ANF)_5$ on ANF also exhibited a constant CIE/cycle time over time, which is expected with a simple crossover process with negligible degradation. This also agrees with the minimal capacity fade observed in Figure 3-4a and b. On the other hand, Neosepta and Celgard 2325 cells experienced rapid increase in CIE/time (degradation rate) after 40 hours, which led to a premature termination of the cycling procedure. This is likely due to material incompatibilities for Neosepta and copious amounts of crossover for Celgard 2325. The ANF cell exhibited elevated CIE/cycle time compared to $(PDDA/PSS)_5$ on ANF, which is expected from its relatively higher permeability. However, it also showed signs of increasing CIE/cycle time after 60 hours but at a slower rate compared to Celgard 2325 and Neosepta. The degradation seen for ANF is likely a combination of crossover and gradual $V(acac)_3$ degradation.

Table 3-2 Summary of CE and VE of Flow Cells

Sample	Coulombic Efficiency (CE)	Voltaic Efficiency (VE)
Celgard 2325	55%	83%
Neosepta AHA	70%	76%
ANF	88%	87%
$(PDDA/PSS)_5$ on ANF	95%	82%

Averaged over cycles before 80% initial capacity

The degradation of $V(acac)_3$ to vanadyl acetylacetonate [$VO(acac)_2$] on the catholyte during cycling has been reported previously.[10,51] In higher permeability separators (Celgard 2325 and to some degree, ANF), degradation to $VO(acac)_2$ can occur in both the catholyte and anolyte reservoirs. Since $VO(acac)_2$ has only one cyclable redox couple at 0.6 V vs.Ag/Ag^{+}[51], capacity fade is observed due to the imbalance in redox events between the cathode and anode and likely the reason for the uptick seen for Celgard 2325 in Figure 3-10d. Conversely, with $(PDDA/PSS)_5$ on ANF as the separator, active species in the catholyte and anolyte remain relatively separated and therefore maintaining a balanced number of redox events even after $VO(acac)_2$ degradation occur in the catholyte. In this case, the cycle life is limited only by the stability of $VO(acac)_2$ and $V(acac)_3$. On the other hand, the situation of the Neosepta is entirely different where unknown degradation events are likely both in the solution and on the surface and bulk of the membrane, causing the rapid capacity fade and increase in CIE/cycle time. Overall, the stability and performance of $(PDDA/PSS)_5$ on ANF has exceeded our expectations and provided a unique opportunity to observe the extended operation of a flow cell with minimal crossover induced degradation.

3.4 Conclusions

In this chapter, we describe the fabrication of a nanoporous size selective separator based on aramid nanofibers (ANF) using a spin-coating layer-by-layer technique. Surface modification of the ANF separators using a layer-by-layer assembly of polyelectrolytes PDDA and PSS is also described as a strategy to increase selectivity. The permeability of $V(acac)_3$ and the conductivity of $TBABF_4$ supporting electrolyte in acetonitrile are measured and compared to those for Celgard 2325, a commercially available polyolefin separator and Neosepta AHA, a commercially available anion exchange membrane. The ANF separator exhibited an order of magnitude reduction in permeability of $V(acac)_3$ due to the reduction in pore size to 5 nm. Surface modification of the ANF separator demonstrated additional reduction in permeability by two orders of magnitude with minimal impact on ionic conductivity. Flow cell charge/discharge studies with realistic cycling times successfully verified the reduced permeability in ANF and $(PDDA/PSS)_5$ on ANF led to high coulombic efficiencies (95%). The exceptional stability exhibited by ANF and $(PDDA/PSS)_5$ on ANF over 100 hours of continuous operation is a testament to the stability of ANF in NAqRFB environments. We envision that with highly stable active materials and further optimization of the ANF separators, highly efficient (99.999%) and longer lasting (>20,000 cycles) NAqRFBs can be achieved.

References

1. Dunn, B., Kamath, H. & Tarascon, J. M. Electrical Energy Storage for the Grid: A Battery of Choices. *Science.* **334,** 928–935 (2011).

2. Alotto, P., Guarnieri, M. & Moro, F. Redox flow batteries for the storage of renewable energy: A review. *Renewable and Sustainable Energy Reviews* **29,** 325–335 (2014).

3. Darling, R. M., Gallagher, K. G. & Brushett, F. R. Environmental Science Pathways to low-cost electrochemical energy storage : a comparison of aqueous and nonaqueous fl ow batteries. *Energy & Environmental Science* **7,** 3459–3477 (2015).

4. Weber, A. Z. *et al.* Redox flow batteries: A review. *Journal of Applied Electrochemistry* **41,** 1137–1164 (2011).

5. Wang, W. *et al.* Recent progress in redox flow battery research and development. *Advanced Functional Materials* **23,** 970–986 (2012).

6. Wei, X. *et al.* Nanoporous Polytetrafluoroethylene/Silica Composite Separator as a High-Performance All-Vanadium Redox Flow Battery Membrane. *Advanced Energy Materials* **3,** 1215–1220 (2013).

7. Wang, W. *et al.* Recent progress in redox flow battery research and development. *Advanced Functional Materials* **23,** 970–986 (2013).

8. Shin, S. H., Yun, S. H. & Moon, S. H. A review of current developments in non-aqueous redox flow batteries: characterization of their membranes for design perspective. *RSC Advances* **3,** 9095 (2013).

9. Liu, Q. *et al.* Non-aqueous chromium acetylacetonate electrolyte for redox flow batteries. *Electrochemistry Communications* **12,** 1634–1637 (2010).

10. Shinkle, A. A., Sleightholme, A. E. S., Griffith, L. D., Thompson, L. T. & Monroe, C. W. Degradation mechanisms in the non-aqueous vanadium acetylacetonate redox flow battery. *Journal of Power Sources* **206,** 490–496 (2012).

11. Xu, K. Nonaqueous Liquid Electrolytes for Lithium-Based Rechargeable Batteries. *Chemical Reviews* **104,** 4303–4417 (2004).

12. Wei, X. *et al.* Towards High-Performance Nonaqueous Redox Flow Electrolyte Via Ionic Modification of Active Species. *Advanced Energy Materials* **5,** 1400678 (2015).

13. Wei, X. *et al.* TEMPO-Based Catholyte for High-Energy Density Nonaqueous Redox Flow Batteries. *Advanced Materials* **26,** 7649–7653 (2014).

14. Parasuraman, A., Lim, T. M., Menictas, C. & Skyllas-Kazacos, M. Review of material research and development for vanadium redox flow battery applications. *Electrochimica Acta* **101,** 27–40 (2013).

15. Vafiadis, H. & Skyllas-Kazacos, M. Evaluation of membranes for the novel vanadium bromine redox flow cell. *Journal of Membrane Science* **279,** 394–402 (2006).

16. Sachan, S., Ray, C. A. & Perusich, S. A. Lithium ion transport through nonaqueous perfluoroionomeric membranes. *Polymer Engineering and Science* **42,** 1469–1480 (2002).

17. Su, L. *et al.* An Investigation of the Ionic Conductivity and Species Crossover of Lithiated Nafion 117 in Nonaqueous Electrolytes. *Journal of The Electrochemical Society* **163,** A5253–A5262 (2016).

18. Shinkle, A. A., Sleightholme, A. E. S., Thompson, L. T. & Monroe, C. W. Electrode kinetics in non-aqueous vanadium acetylacetonate redox flow batteries. *Journal of Applied Electrochemistry* **41,** 1191–1199 (2011).

19. Sleightholme, A. E. S. *et al.* Non-aqueous manganese acetylacetonate electrolyte for redox flow batteries. *Journal of Power Sources* **196,** 5742–5745 (2011).

20. Matsuda, Y. *et al.* A rechargeable redox battery utilizing ruthenium complexes with non-aqueous organic electrolyte. *Journal of Applied Electrochemistry* **18,** 909–914 (1988).

21. Chakrabarti, M. H., Dryfe, R. A. W. & Roberts, E. P. L. Evaluation of electrolytes for redox flow battery applications. *Electrochimica Acta* **52,** 2189–2195 (2007).

22. Mun, J. *et al.* Non-Aqueous Redox Flow Batteries with Nickel and Iron Tris(2,2′-bipyridine) Complex Electrolyte. *Electrochemical and Solid-State Letters* **15,** A80 (2012).

23. Escalante-Garcia, I. L., Wainright, J. S., Thompson, L. T. & Savinell, R. F. Performance of a Non-Aqueous Vanadium Acetylacetonate Prototype Redox Flow Battery: Examination of Separators and Capacity Decay. *Journal of the Electrochemical Society* **162,** A363–A372 (2014).

24. Zhang, D., Liu, Q., Shi, X. & Li, Y. Tetrabutylammonium hexafluorophosphate and

1-ethyl-3-methyl imidazolium hexafluorophosphate ionic liquids as supporting electrolytes for non-aqueous vanadium redox flow batteries. *Journal of Power Sources* **203,** 201–205 (2012).

25. Xu, T. Ion exchange membranes: State of their development and perspective. *Journal of Membrane Science* **263,** 1–29 (2005).

26. Kim, D. H. *et al.* Pore-filled anion-exchange membranes for non-aqueous redox flow batteries with dual-metal-complex redox shuttles. *Journal of Membrane Science* **454,** 44–50 (2014).

27. Maurya, S., Shin, S. H., Sung, K. W. & Moon, S. H. Anion exchange membrane prepared from simultaneous polymerization and quaternization of 4-vinyl pyridine for non-aqueous vanadium redox flow battery applications. *Journal of Power Sources* **255,** 325–334 (2014).

28. Cho, E. & Won, J. Novel composite membrane coated with a poly(diallyldimethylammonium chloride)/urushi semi-interpenetrating polymer network for non-aqueous redox flow battery application. *Journal of Power Sources* **335,** 12–19 (2016).

29. Arora, P. & Zhang, Z. J. Battery separators. *Chemical reviews* **104,** 4419–62 (2004).

30. Zhang, H., Zhang, H., Li, X., Mai, Z. & Wei, W. Silica modified nanofiltration membranes with improved selectivity for redox flow battery application. *Energy & Environmental Science* **5,** 6299 (2012).

31. Zhang, H., Zhang, H., Li, X., Mai, Z. & Zhang, J. Nanofiltration (NF) membranes:

the next generation separators for all vanadium redox flow batteries (VRBs)? *Energy & Environmental Science* **4,** 1676 (2011).

32. Wei, X. *et al.* Polyvinyl Chloride/Silica Nanoporous Composite Separator for All-Vanadium Redox Flow Battery Applications. *Journal of the Electrochemical Society* **160,** A1215–A1218 (2013).

33. Li, C. *et al.* Polysulfide-Blocking Microporous Polymer Membrane Tailored for Hybrid Li-Sulfur Flow Batteries. *Nano letters* **15,** 5724–5729 (2015).

34. Nagarjuna, G. *et al.* Impact of Redox-Active Polymer Molecular Weight on the Electrochemical Properties and Transport Across Porous Separators in Nonaqueous Solvents. *Journal of American Chemical Society* 16309–16316 (2014).

35. Wan, L. S., Li, J. W., Ke, B. B. & Xu, Z. K. Ordered microporous membranes templated by breath figures for size-selective separation. *Journal of the American Chemical Society* **134,** 95–8 (2012).

36. Hinds, B. J. *et al.* Aligned multiwalled carbon nanotube membranes. *Science.* **303,** 62–5 (2004).

37. Peng, X. & Ichinose, I. Green-Chemical Synthesis of Ultrathin β-MnOOH Nanofibers for Separation Membranes. *Advanced Functional Materials* **21,** 2080–2087 (2011).

38. Zhang, Z. *et al.* Polyacrylonitrile and Carbon Nanofibers with Controllable Nanoporous Structures by Electrospinning. *Macromolecular Materials and Engineering* **294,** 673–678 (2009).

39. Wu, S., Li, F., Wu, Y., Xu, R. & Li, G. Preparation of novel poly(vinyl alcohol)/SiO(2) composite nanofiber membranes with mesostructure and their application for removal of Cu(2+) from waste water. *Chemical Communications* **46,** 1694–6 (2010).

40. Lin, J., Ding, B., Yu, J. & Hsieh, Y. Direct Fabrication of Highly Nanoporous Polystyrene Fibers via Electrospinning. *ACS applied materials & interfaces* **2,** 521–528 (2010).

41. Hilal, N., Al-Zoubi, H., Darwish, N. A., Mohammad, A. W. & Abu Arabi, M. A comprehensive review of nanofiltration membranes: Treatment, pretreatment, modelling, and atomic force microscopy. *Desalination* **170,** 281–308 (2004).

42. Wang, X. L., Shang, W. J., Wang, D. X., Wu, L. & Tu, C. H. Characterization and applications of nanofiltration membranes: State of the art. *Desalination* **236,** 316–326 (2009).

43. Tung, S. O., Ho, S., Yang, M., Zhang, R. & Kotov, N. A. A dendrite-suppressing composite ion conductor from aramid nanofibres. *Nature Communications* **6,** 6152 (2015).

44. Suttil, J. A. *et al.* Metal acetylacetonate complexes for high energy density non-aqueous redox flow batteries. *Journal of Materials Chemistry A* **3,** 7929–7938 (2015).

45. Yang, M. *et al.* Dispersions of Aramid Nanofibers : A New Nanoscale Building Block. *ACS Nano* 6945–6954 (2011).

46. Milshtein, J. D., Barton, J. L., Darling, R. M. & Brushett, F. R. 4-acetamido-2,2,6,6-tetramethylpiperidine-1-oxyl as a model organic redox active compound for nonaqueous flow batteries. *Journal of Power Sources* **327,** 151–159 (2016).

47. Podsiadlo, P. *et al.* Ultrastrong and stiff layered polymer nanocomposites. *Science.* **318,** 80–3 (2007).

48. Li, Y., Wang, X. & Sun, J. Layer-by-layer assembly for rapid fabrication of thick polymeric films. *Chemical Society reviews* **41,** 5998–6009 (2012).

49. Sparreboom, W., van den Berg, A. & Eijkel, J. C. T. Principles and applications of nanofluidic transport. *Nature Nanotechnology* **4,** 713–720 (2009).

50. Xi, J. *et al.* Self-assembled polyelectrolyte multilayer modified Nafion membrane with suppressed vanadium ion crossover for vanadium redox flow batteries. *Journal of Materials Chemistry* **18,** 1232 (2008).

51. Kucharyson, J. Structure-Function Relationships of Metal Coordination Complexes for Non-Aqueous Redox Flow Batteries. (University of Michigan, Ann Arbor, 2017).

52. Smith, A. J., Burns, J. C. & Dahn, J. R. A High Precision Study of the Coulombic Efficiency of Li-Ion Batteries. *Electrochemical and Solid-State Letters* **13,** A177 (2010).

Chapter 4

High Performance Pillared Vanadium Oxide Cathode for Lithium Ion Batteries

4.1 Background and Approach

Rechargeable lithium-ion batteries (LIBs) have, due to their relatively high energy densities, enabled a new generation of personal electronics and expanded deployment of electric vehicles (EVs) and hybrid electric vehicles (HEVs).[1,2] Energy density is the key consideration for most applications, however, the rate capability, cyclability, and safety are also important considerations.[3] All of these features need to be improved to enable next generation EVs and HEVs. Two approaches have been taken to enhance the energy and power densities of LIBs: (1) modifying the electrode architecture,[4] and (2) altering the nanoscale structure of the active electrode materials.[5] The structural and thermal stabilities of the active materials are key determinants for LIB cyclability and safety;[6–8] consequently efforts to demonstrate high rate capability, cyclability, and safety have focused on carefully engineering the nanoscale structure of the active electrode materials.

Layered lithium metal oxides are widely used in the cathodes of LIBs. Despite their proliferation in batteries for small electronics, the use of these materials in vehicle applications has been limited due to their relatively poor structural and thermal stabilities. For example, lithium cobalt oxide is only stable up to ~170 °C, at which point oxygen

liberation is observed.[9] This is especially problematic in the event of thermal runaway, where the temperature of a battery rises uncontrollably leading to explosion and fire with flammable electrolyte solvents acting as fuel.[10] Furthermore, repeated intercalation and de-intercalation of the lithium ions during the normal charge and discharge process causes mechanical fatigue of the lattice structure.[8] Structural collapse leads to capacity fade as lithium host sites are lost.

In attempts to enhance the stability of layer structured cathode materials, nano-scale pillars[11,12] have been inserted between the layers to provide structural support. Intercalation of pillaring agents into various layered materials (e.g. smectite clays, MnO_2) has been demonstrated to increase the interlayer spacing in the crystallites.[11–16] Additionally, Keggin ion pillared Na-bentolite clays show improved thermal stability, to >500 °C in some cases.[12] Pillaring MnO_2 with alumina nanoparticles has also been reported to increase the mesoporosity and overall surface area.[11,14] This enhancement in surface area improves access of lithium ions to adsorption sites. In terms of electrochemical performance, an alumina pillared clay electrode has been reported to show an increase in redox activity for the $Fe(bipy)_3^{2+/3+}$ redox couple,[12] and pillaring MnO_2 resulted in an increase in lithium insertion.[11]

Research described in this chapter explores the effects of nanopillaring on the thermal and electrochemical properties of vanadium pentoxide (V_2O_5) xerogels. Despite a high theoretical capacity (up to 562 mAh g^{-1} based on 4 Li transfer), V_2O_5 has not been used in battery applications due to its poor structural stability, slow electrochemical kinetics, and low electronic conductivity.[17] One strategy to increase capacity is exfoliation of the V_2O_5 layers. An et al., found that complete exfoliation

of V_2O_5 into ultrathin 2D nanosheets yielded very high surface area and increased rate capabilities over prolonged cycling, however it is not clear if the nanosheets are able to withstand thermal abuse.[18] Other efforts have focused on improving the electronic conductivity of V_2O_5 to improve performance, both through the incorporation of Cu^{2+} ions into the lattice,[19] and by creating a composite of V_2O_5 and reduced graphene oxide.[20] V_2O_5 xerogels and aerogels, in which the V_2O_5 layers are swollen with water and subsequently dried, demonstrate improved lithium intercalation kinetics, yet remain susceptible to poor structural stability and thermal stability (only stable up to 300 °C).[21] We have demonstrated that the insertion of aluminum Keggin ions between layers in V_2O_5 xerogels results in enhanced rate capability, cyclability, and structural and thermal stabilities. This approach could also be used to enhance the properties of other layered compounds.

4.2 Material and Methods

This section describes the material and methods used in this work.

4.2.1 Xerogel Preparation and Pillaring

To prepare the V_2O_5 xerogel, 3 g of crystalline V_2O_5 powder (Sigma Aldrich, St. Louis, MO) was dissolved in 300 mL of a 10% hydrogen peroxide solution (Fisher Scientific, Waltham, MA) with constant stirring at room temperature. After 18 hours of continuous stirring, the solution was then dried at 50 °C under vacuum overnight to obtain dark red flakes of the V_2O_5 xerogel. The flakes were then crushed to obtain a fine V_2O_5 xerogel powder.

The Al_{13} Keggin solution was prepared by combining 50 mL of an aqueous aluminum chloride solution ($AlCl_3$) and 100 mL of an aqueous sodium hydroxide solution (NaOH) in a 1:2.1 molar ratio[22] (both obtained from Sigma Aldrich, St. Louis, MO). The sodium hydroxide solution was added to the $AlCl_3$ solution dropwise, and then the resulting mixture was aged for 3 days with continuous stirring. Once the Al_{13} Keggin solution was prepared, 1 g of the V_2O_5 xerogel powder was added and the resulting mixture was stirred for 3 days at room temperature to enable the pillaring process. The pillared V_2O_5 powder was collected via centrifugation and washed repeatedly with de-ionized water. The sample was then dried under vacuum at 50 °C overnight. Selected samples of the pillared V_2O_5 material were heat treated at 350 °C in either air or nitrogen for 2 hours.

4.2.2 Material Characterization

X-ray diffraction (XRD) was carried out using a Rigaku rotating anode X-ray diffractometer. Transmission electron images were obtained using a JEOL 3011 HRTEM microscope. The TGA experiments were performed in a TA instruments Discovery Thermogravimetric analyzer. Approximately 5 mg of sample was used in each measurement. The measurements were carried out under nitrogen, with a 5 °C min^{-1} heating rate to a final temperature of 500 °C. The same heating rates were used in the TPD measurements with nitrogen flow. The TPD was performed using a Micromeritics Autochem 2910 Automated catalyst characterization system. Surface area measurements were performed using a Micromeritics ASAP 2020 Surface Area and Porosity Analyzer.

4.2.3 Electrochemical Measurements

For electrochemical characterization, electrodes were prepared using a slurry with a dry composition of 70% active material, 20% Super P Li carbon (TIMCAL, Switzerland), and

10% polyvinylidene fluoride (Kynar, owned by Arkema, Colombes, France) as a binder. The solvent used in the slurry was n-methyl pyrrolidone (Sigma-Aldrich, St. Louis, MO). A high-speed FlakTech mixer (Landrum, SC) was used to ensure that the slurry was well mixed. The slurry was doctor bladed onto clean aluminum foil current collectors, then dried for two hours under air at 110 °C, then under vacuum at 110 °C overnight. The active material loading was determined by the weight after drying.

Cyclic voltammetry, capacity, and charge/discharge measurement were performed using 2032 coin cells assembled in an argon filled glovebox. Lithium metal discs were used as the anode, with a Celgard 2500 separator (Celgard, Charlotte, NC). The electrolyte consisted of a mixture of ethylene carbonate and dimethyl carbonate (1:1 v/v) with 1 M $LiPF_6$ as the supporting electrolyte, and was obtained from SoulBrain (Northville Township, MI). Galvanostatic charge-discharge experiments were performed using a Maccor Series 4000 multichannel battery test stand. Cyclic voltammetry was performed using a Metrohm Autolab potentiostat, with the lithium metal counter electrode serving as a Li/Li^+ quasi reference electrode. The second cycle for each material is reported.

4.3 Results

This section describes the results and compares performance between pillared and un-pillared materials.

4.3.1 Interlayer Spacing of Pillared Xerogels

The X-ray diffraction patterns for the as-prepared (V_2O_5G) and Al_{13} Keggin ion pillared (V_2O_5-Al_{13}) V_2O_5 xerogels are provided in Figure 4-1. The V_2O_5G material exhibited diffraction peaks at 7.8, 23.2, 30.8 and 38.7°, corresponding to the (001), (003), (004), and

(005) reflections.[23] For the Al_{13} Keggin pillared material, the position of the (001) reflection shifted, and two new peaks emerged in addition to the peaks observed for V_2O_5G (Figure 4-1b). These peaks at 13.2, 20.0, 26.9, 33.7, and 40.7° are likely due to a combination of diffraction from the Al_{13} Keggin ions and from the (003), (004), and (005) planes in the V_2O_5 xerogel. It is possible that the Al_{13} Keggin ions are distorting the tight bilayer structure of the xerogel, causing the negative shift observed for the higher angle peaks.[23] Additionally, the interlayer spacing for the (001) planes (7.8° for V_2O_5G) increased from 11.4 to 13.2 Å, consistent with the reported size of the Al_{13} Keggin ions (10 to 20 Å).[22] Elemental analysis using inductively coupled plasma spectroscopy (ICP) shows that 9 wt% Al was incorporated into the V_2O_5 xerogels.

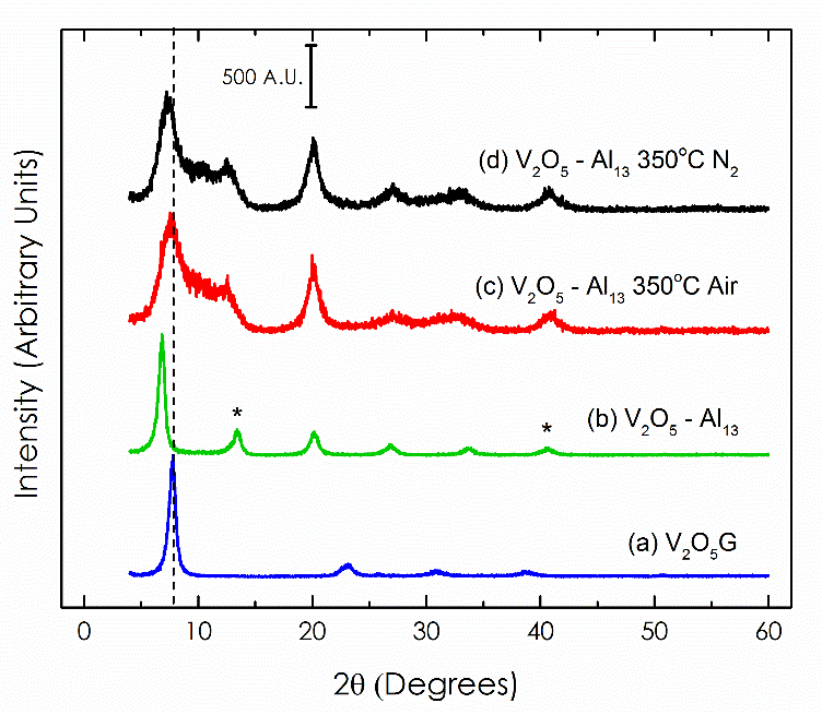

Figure 4-1. X-ray Diffraction patterns for (a) V_2O_5 xerogel (V_2O_5G), (b) Al_{13} Keggin intercalated V_2O_5 xerogel (V_2O_5G-Al_{13}), and V_2O_5G-Al_{13} following treatment at 350 °C in (c) air, and (d) nitrogen. The dotted line is intended as a guide for the eye, and corresponds to an interlayer spacing of 11.4 A in the (001) plane. The * marks correspond to new peaks observed in the V_2O_5-Al_{13} material, due to the incorporation to the Keggin ions.

High-resolution transmission electron microscopy (HRTEM) was used to image morphologies of the V_2O_5G and V_2O_5-Al_{13} samples. The micrograph for the V_2O_5G material shows a layered nanoribbon structure with lattice spacings of ~11.4 Å (Figure 4-2a). This observation is consistent with the (001) spacing determined from the diffraction patterns (Figure 4-1) as well as previously published results.[24] The interlayer spacing is increased for the V_2O_5-Al_{13} material due to intercalation of the Al_{13} Keggin ions (Figure 4-2b). For the V_2O_5-Al_{13} materials treated in air or nitrogen at 350 °C (Figure 4-2 c and d, respectively), the crystallite sizes are distinctly smaller as indicated by the broadened diffraction peaks while the (001) interlayer spacings are similar to those for the untreated V_2O_5G material.

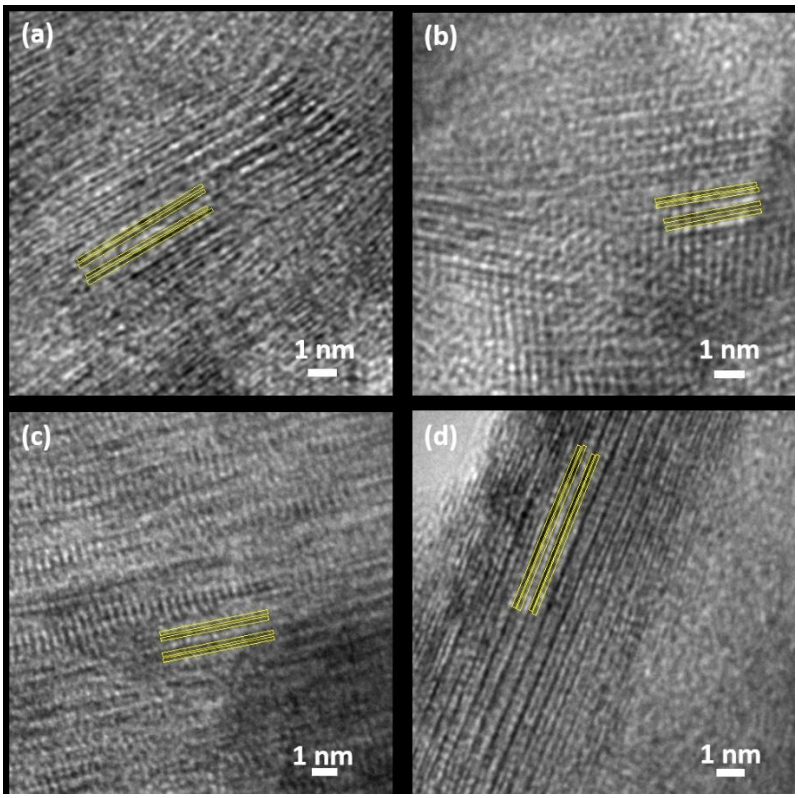

Figure 4-2. High resolution TEM micrographs for (a) V_2O_5 xerogel (V_2O_5G), (b) Al_{13} Keggin intercalated V_2O_5 xerogel (V_2O_5G-Al_{13}), and V_2O_5G-Al_{13} following treatment at 350 °C in (c) air, and (d) nitrogen. The yellow lines indicate the V_2O_5 layers.

4.3.2 Thermal stability

Temperature programmed desorption (TPD) and thermal gravimetric analysis (TGA) were used to characterize the removal of water and thermal stabilities of the V_2O_5G and V_2O_5-Al_{13} materials. There was good correspondence between the TPD and TGA results with water loss tracking with overall mass loss. At 350 °C, all of the water was removed from the V_2O_5G material (Figure 4-3a and c) and the material was converted to crystalline V_2O_5 as indicated by the diffraction pattern (Figure 4-4). For the pillared V_2O_5-Al_{13} material, only

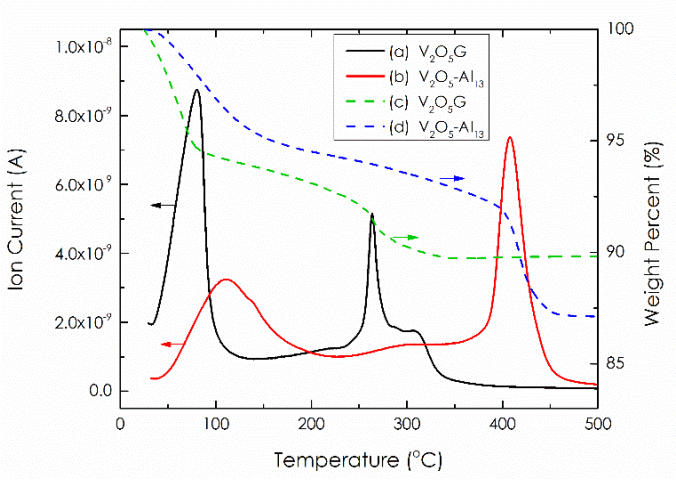

Figure 4-3 Ion current for H_2O during temperature programmed desorption and thermal gravimetric analysis for (a) V_2O_5 xerogel (V_2O_5G) and (b) Al_{13} Keggin intercalated V_2O_5 xerogel (V_2O_5G-Al_{13}).

about half of the initial water was removed by 350 °C (Figure 4-3 b and d). Complete removal of water from the V_2O_5-Al_{13} material required temperatures of ~400 °C. At this temperature, a reaction occurs between the Keggin ions and V_2O_5, resulting in a new, non-layered aluminum-vanadium oxide phase (the diffraction pattern is shown in Figure 4-5).

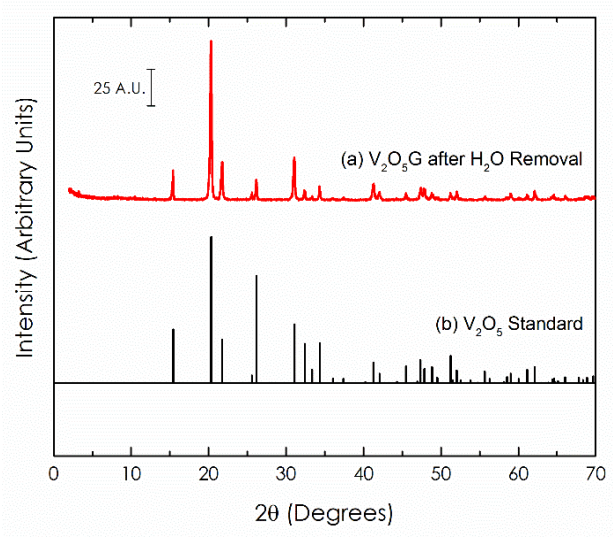

Figure 4-4. Diffraction patterns for a) V_2O_5 xerogel after heat treatment at 350 °C in air, as compared to b) crystalline V_2O_5 standard. The unpillared V_2O_5 xerogel reverts back to crystalline V_2O_5 when heat treated at 350 °C in nitrogen.

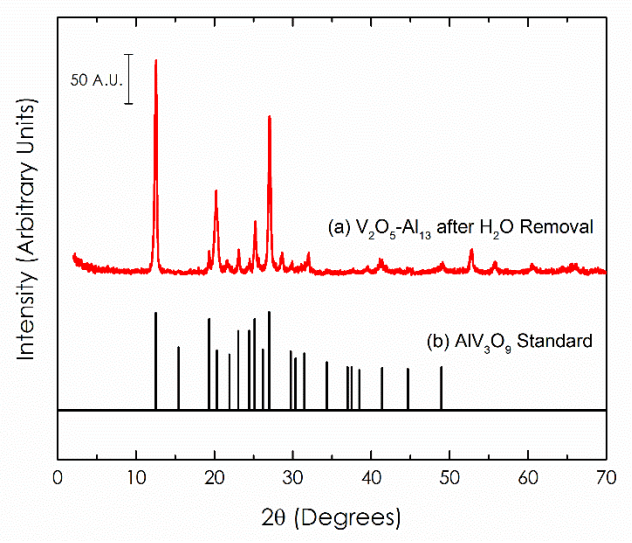

Figure 4-5 Diffraction patterns for a) V_2O_5-Al_{13} after heat treatment at 400 °C in nitrogen as compared to b) an AlV_3O_9 standard. A new, non-layered phase containing both vanadium and aluminum is observed after heat treatment of pillared V_2O_5 xerogel at 400 °C.

4.3.3 Electrochemical Characterization

Electrochemical properties of the V_2O_5G and V_2O_5-Al_{13} (untreated and heat treated) materials were characterized using cyclic voltammetry and charge/discharge experiments in coin cells. A lithium metal anode served as a quasi Li/Li^+ reference electrode for the cyclic voltammetry experiments, which were conducted at 0.1 mV s^{-1} between 2.0 and 3.8 V vs. Li/Li^+ (Figure 4-6). The cyclic voltammetry for the V_2O_5G material is consistent with those reported in the literature.[25,26] Two redox couples are observed, at half-peak potentials of approximately 2.6 and 2.9 V versus Li/Li^+. The CV for the V_2O_5-Al_{13} materials were similar to that for V_2O_5G, although the peak current for the couple at 2.9 V was higher than that for the couple at 2.6 V. In addition, there was a decrease in peak separation when comparing the V_2O_5G and V_2O_5-Al_{13} materials. This indicates that the kinetics for lithium ion intercalation were improved with addition of the Al_{13} Keggin pillars.

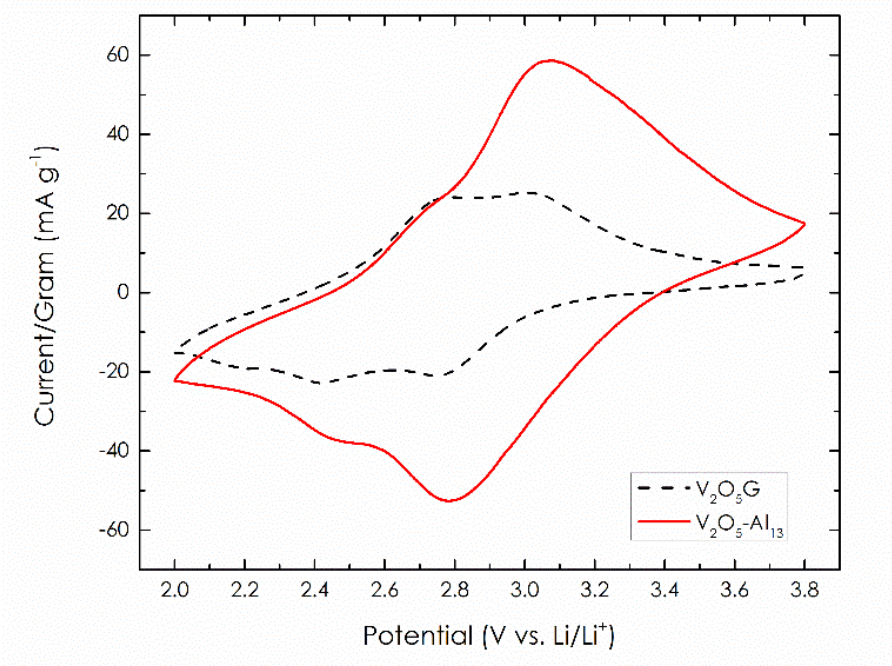

Figure 4-6. Cyclic voltammetry associated with Li intercalation for the V2O5G and V2O5-Al_{13} cathode materials. Cycled at 0.1 mV s^{-1}.

Cyclic voltammetry for the V_2O_5-Al_{13} materials treated at 350 °C in N_2 and in air are presented in Figure 4-7. Both redox couples are observed, however, the cyclic voltammograms have several small shoulders present on the second redox couple. These shoulders are reproducible on subsequent cycling, and may be due to the more amorphous nature of the heat-treated materials. The improvement in kinetics on introducing the pillaring agent is further exemplified in results from the charge-discharge experiments.

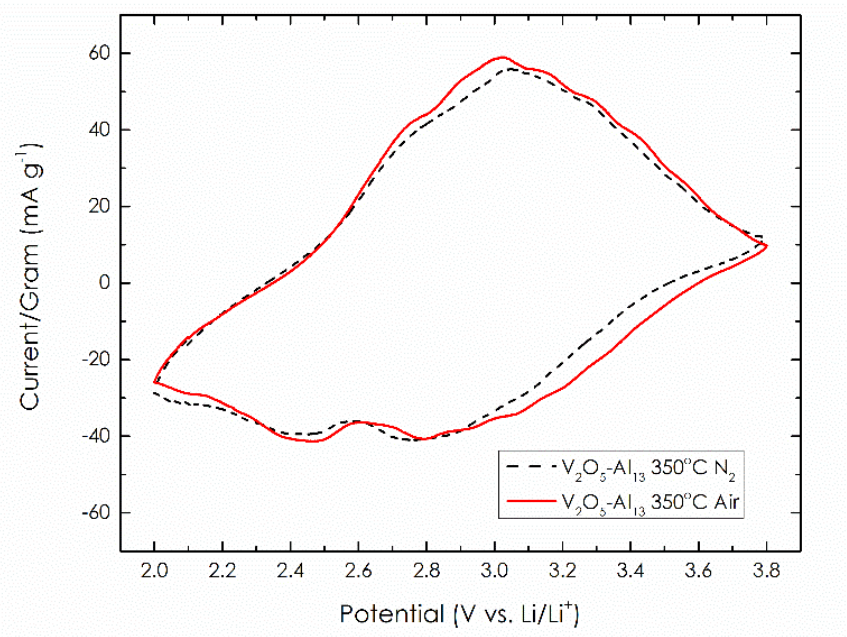

Figure 4-7. Cyclic voltammetry associated with Li intercalation for the V_2O_5-Al_{13} 350°C N_2 and V_2O_5-Al_{13} 350°C Air cathode materials. Cycled at 0.1 mV s^{-1}.

4.3.4 Cycling Performance in Coin Cells

The unpillared and pillared V_2O_5 xerogel materials were cycled in coin cells to assess their performance and rate capabilities. In Figure 4-8, charge/discharge profiles for the cathode materials are shown. The cell potentials are similar for each cathode material, cycling at ~2.8 V on average with a smooth voltage profile. Although the voltage is somewhat lower than that reported in the literature for V_2O_5 xerogels, the voltage profile is fairly

consistent.[25] The V_2O_5-Al_{13} cell has a slightly lower capacity than the V_2O_5G cell; the heat treated pillared materials both show up to a 60% increase in capacity over the V_2O_5G cell. Additionally, the heat treated pillared materials discharged at higher voltages than the cells containing V_2O_5G and V_2O_5-Al_{13}. It is possible that this increase in capacity and voltage could be further improved by using a more crystalline sample of the heat treated pillared V_2O_5 (the diffraction patterns in Figure 4-1 showed a slight loss in crystallinity after heat treatment).

Rate capability was assessed by performing experiments at C/10, C/2, C/10, 2C, and then C/10, for 10 cycles at each rate. The experiments served two purposes. Tests at C/2 and 2C enabled an assessment of the high rate performance of the cells. Tests at C/10 were designed to determine the capacity retention of the material; these experiments included returning the cell to the low rate (C/10) after cycling at high rates. The discharge capacities for each cycle are plotted as a percentage of the low rate (C/10) capacity in Figure 4-9 (the unnormalized data is provided in Figure 4-10). Capacity for the V_2O_5G containing cell faded quickly, falling to 81% of its initial capacity by the 10th cycle at C/10. By the 50th cycle, the capacity of the V_2O_5G cell leveled off at ~60% of its initial capacity at C/10. The V_2O_5-Al_{13} and V_2O_5-Al_{13} 350 °C Air materials demonstrated improved capacity retention relative to the V_2O_5G materials, retaining 90% of their low rate capacities. Furthermore, the cell containing the V_2O_5-Al_{13} materials showed higher capacities than the V_2O_5G material at higher discharge rates. At C/2, the V_2O_5-Al_{13} 350 °C N_2 material retained 60% of its low-rate capacity, whereas the V_2O_5G material retained only 36%.

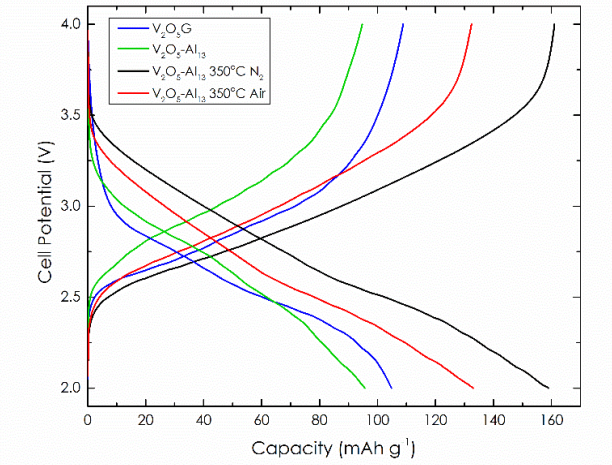

Figure 4-8 Charge/discharge curves for coin cells containing V_2O_5G, V_2O_5-Al_{13}, V_2O_5-Al_{13} 350°C N_2, and V_2O_5-Al_{13} 350°C Air cathode materials. Cycled at C/10.

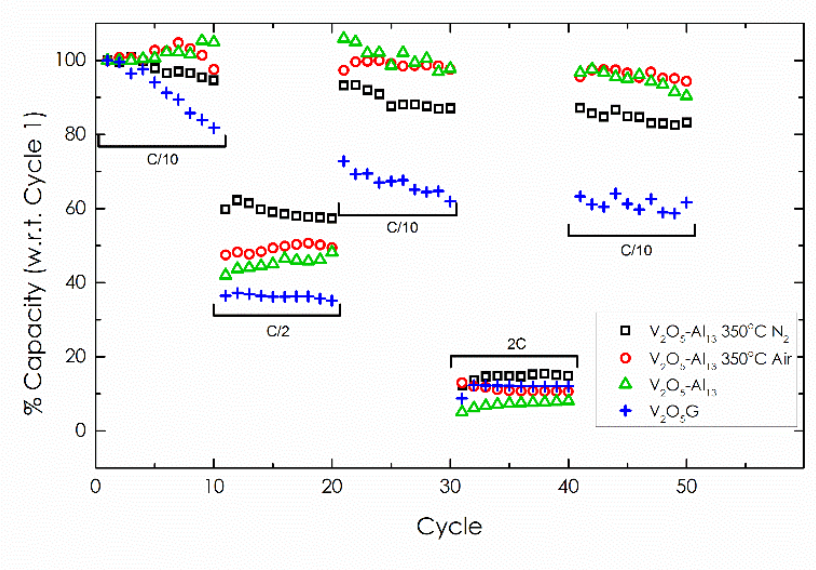

Figure 4-9. Discharge capacities with respect to the capacity at C/10 for V_2O_5G, V_2O_5-Al_{13}, and V_2O_5-Al_{13} heat treated at 350 °C in either air or nitrogen. Experiments were performed at each C rate for 10 cycles.

The increased capacities and perhaps the improved rate capabilities may have been a consequence of changes in the surface area on introducing the pillaring species. Surface areas for the V_2O_5G and V_2O_5-Al_{13} (untreated and heat treated) materials are listed in Table 4-1, along with discharge capacities measured at C/10 and C/2. The surface area of the

V_2O_5-Al_{13} material is approximately twice that of the V_2O_5G material; however, the discharge capacity at the low and high rates are similar. It should be noted that although the capacities for both materials are similar, the V_2O_5-Al_{13} material retains more of its capacity at a variety of C rates, as shown in Figure 4-9. Heat-treatment of the V_2O_5-Al_{13} material did not significantly affect the surface area, while the measured capacities of the V_2O_5-Al_{13} material treated at 350 °C in N_2 are much higher than those for the V_2O_5G and untreated V_2O_5-Al_{13} materials (171 mAh g^{-1} vs. ~100 mAh g^{-1} at C/10, respectively). Therefore, the results indicate that changes in the electrochemical properties were not due to changes in the surface areas.

Long term stability at high discharge rates is a challenge for LIBs.[6] The V_2O_5G, V_2O_5-Al_{13}, and heat treated V_2O_5-Al_{13} materials were cycled at C/2 for 100 cycles to investigate their long-term cyclability (Figure 4-11). Again, the capacity for the coin cell containing V_2O_5G faded quickly, and settled at ~47 mAh g^{-1} with respect to the active material. Cells containing the heat treated V_2O_5-Al_{13} materials started at higher capacities and maintained a higher fraction of their capacity throughout cycling. The coin cell containing V_2O_5-Al_{13} treated at 350 °C in N_2 had a capacity of 102 mAh g^{-1} for the first cycle, and 77 mAh g^{-1} for the 100^{th} cycle. While all of the reported capacities are somewhat low compared to those in the literature (capacities as high as 250 mAh g^{-1} at C/5 and 100 mAh g^{-1} at 20C have been reported for other modified V_2O_5 materials),[19] this represents a capacity increase of greater than 60% in the cell containing pillared heat-treated material over the cell containing V_2O_5G. The capacity retention demonstrated for the pillared V_2O_5 xerogels also represents significant improvements over performance characteristics for their unpillared V_2O_5 xerogel counterparts. With further development, and perhaps focus on other high

performing materials, pillared cathodes could lead to performance increases in lithium ion batteries.

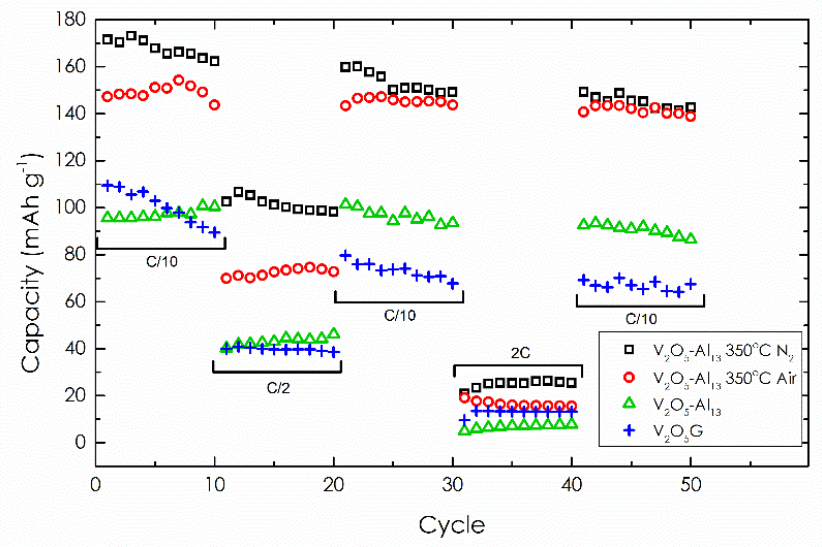

Figure 4-10. Discharge capacities for coin cells containing V_2O_5G, V_2O_5-Al_{13}, and V_2O_5-Al_{13} treated at 350 °C in either air or nitrogen as the cathode material. Experiments were performed at C/10, C/2, C/10, 2C, and C/10 for 10 cycles each.

Table 4-1. Surface areas and discharge capacities for V_2O_5G, V_2O_5-Al_{13}, and V_2O_5-Al_{13} 350 °C N_2 materials.

Material	Surface Area (m^2 g^{-1})	C/2 Capacity (mAh g^{-1})	C/10 Capacity (mAh g^{-1})
V_2O_5G	0.55 ± 0.01	67	109
V_2O_5-Al_{13}	1.04 ± 0.02	67	96
V_2O_5-Al_{13} 350°C N_2	1.14 ± 0.01	102	171

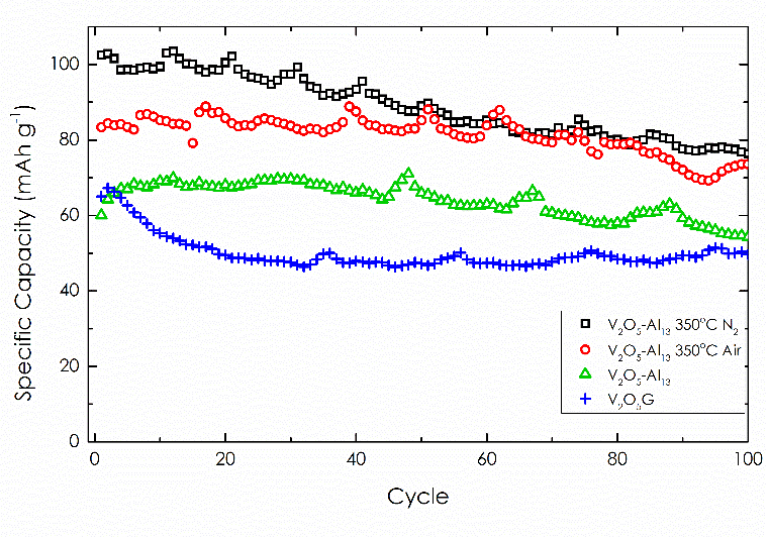

Figure 4-11. Specific capacities for V_2O_5 xerogel (V_2O_5G) and pillared V_2O_5 materials (V_2O_5-Al_{13}) prior to and after heat treatment. Experiments were performed at C/2 for 100 cycles.

4.4 Conclusions

Al_{13} Keggin ions were successfully introduced between the layers in V_2O_5 xerogels. X-ray diffraction indicated an increase in the lattice spacing ((001) planes) from 11 to 13 Å upon introduction of the Al_{13} Keggin ions, while the layered structure was maintained, as demonstrated by TEM. Treatment of the as-prepared materials at 350 °C in either air or nitrogen resulted in a reduction in the crystallite sizes; again the layered structure was maintained. The pillared V_2O_5 xerogels that were treated at 350 °C exhibited a significant increase in both capacity and capacity retention when compared to the unpillared materials. Furthermore, charge-discharge cycling with the pillared cathode materials at high rate over 100 cycles showed a higher degree of stability and capacity than the unpillared V_2O_5. This method of nanostructuring cathode materials may lead to significant increases in Lithium Ion battery capacity and rate capability with refinement of the material synthesis process and optimization of battery design.

References

1. Dunn, B., Kamath, H. & Tarascon, J. M. Electrical Energy Storage for the Grid: A Battery of Choices. *Science.* **334,** 928–935 (2011).

2. Armand, M. & Tarascon, J. M. Building better batteries. *Nature* **451,** 652–657 (2008).

3. Hayner, C. M., Zhao, X. & Kung, H. H. Materials for rechargeable lithium-ion batteries. *Annual review of chemical and biomolecular engineering* **3,** 445–71 (2012).

4. Zhang, H., Yu, X. & Braun, P. V. Three-dimensional bicontinuous ultrafast-charge and -discharge bulk battery electrodes. *Nature nanotechnology* **6,** 277–81 (2011).

5. Kang, K., Meng, Y. S., Bréger, J., Grey, C. P. & Ceder, G. Electrodes with high power and high capacity for rechargeable lithium batteries. *Science* **311,** 977–980 (2006).

6. Etacheri, V., Marom, R., Elazari, R., Salitra, G. & Aurbach, D. Challenges in the development of advanced Li-ion batteries: a review. *Energy & Environmental Science* **4,** 3243 (2011).

7. Fergus, J. W. Recent developments in cathode materials for lithium ion batteries. *Journal of Power Sources* **195,** 939–954 (2010).

8. Vetter, J. *et al.* Ageing mechanisms in lithium-ion batteries. *Journal of Power Sources* **147,** 269–281 (2005).

9. Baba, Y., Okada, S. & Yamaki, J. Thermal stability of LixCoO2 cathode for lithium

ion battery. *Solid State Ionics* **148,** 311–316 (2002).

10. Wang, Q. *et al.* Thermal runaway caused fire and explosion of lithium ion battery. *Journal of Power Sources* **208,** 210–224 (2012).

11. Wang, L., Sakai, N., Ebina, Y., Takada, K. & Sasaki, T. Inorganic multilayer films of manganese oxide nanosheets and aluminum polyoxocations: Fabrication, structure, and electrochemical behavior. *Chemistry of Materials* **17,** 1352–1357 (2005).

12. Petridis, D., De S. Kaviratna, P. & Pinnavaia, T. J. Electrochemistry of alumina pillared clay modified electrodes. *Journal of Electroanalytical Chemistry* **410,** 93–99 (1996).

13. Thomas, S. M. & Occelli, M. L. Effects of Synthesis Conditions on the Thermal Stability of a Texas Montmorillonite Expanded wtih $[Al_{13}O_4(OH)_{24}(H_2O)_{12}]^{7+}$ Cations. *Clays and Clay Minerals* **48,** 304–308 (2000).

14. Wang, L. Z., Ebina, Y., Takada, K., Kurashima, K. & Sasaki, T. A New Mesoporous Manganese Oxide Pillared with Double Layers of Alumina. *Advanced Materials* **16,** 1412–1416 (2004).

15. Zakharova, G. S. & Volkov, V. L. Intercalation compounds based on vanadium(V) oxide xerogel. *Russian Chemical Reviews* **72,** 311–325 (2003).

16. Khairy, M., Tinet, D. & van Damme, H. The synthesis of pillared vanadium oxide. *Journal of the Chemical Society, Chemical Communications* 856 (1990).

17. Whittingham, M. S. Lithium Batteries and Cathode Materials. *Chemical Reviews*

104, 4271–4302 (2004).

18. An, Q. *et al.* Supercritically exfoliated ultrathin vanadium pentoxide nanosheets with high rate capability for lithium batteries. *Physical Chemistry Chemical Physics* **15,** 16828 (2013).

19. Yu, H. *et al.* Cu doped V_2O_5 flowers as cathode material for high-performance lithium ion batteries. *Nanoscale* **5,** 4937–43 (2013).

20. Zhao, H., Pan, L., Xing, S., Luo, J. & Xu, J. Vanadium oxides–reduced graphene oxide composite for lithium-ion batteries and supercapacitors with improved electrochemical performance. *Journal of Power Sources* **222,** 21–31 (2013).

21. Chen, Z. *et al.* Effect of thermal treatment on the formation and transformation of Keggin Al_{13} and Al_{30} species in hydrolytic polymeric aluminum solutions. *Colloids and Surfaces A: Physicochemical and Engineering Aspects* **292,** 110–118 (2007).

22. Casey, W. H. Large aqueous aluminum hydroxide molecules. *Chemical Reviews* **106,** 1–16 (2006).

23. Petkov, V. *et al.* Structure of $V_2O_5 \cdot nH_2O$ Xerogel Solved by the Atomic Pair Distribution Function Technique. *Journal of the American Chemical Society* **124,** 10157–10162 (2002).

24. Mège, S., Levieux, Y., Ansart, F., Savariault, J. M. & Rousset, A. Electrochemical properties of a new V_2O_5 xerogel. *Journal of Applied Electrochemistry* **30,** 657–664 (2000).

25. Wang, Y., Shang, H., Chou, T. & Cao, G. Effects of thermal annealing on the Li^+

intercalation properties of V_2O_5 x nH_2O xerogel films. *The Journal of Physical Chemistry B* **109,** 11361–6 (2005).

26. Baddour, R., Pereira-Ramos, J. P., Messina, R. & Perichon, J. A thermodynamic, structural and kinetic study of the electrochemical lithium intercalation into the xerogel $V_2O_5 \cdot 1.6\ H_2O$ in a propylene. *Journal of Electroanalytical Chemistry and Interfacial Electrochemistry* **314,** 81–101 (1991).

Chapter 5

Scale up of ANF Separators for Lithium Ion Batteries

5.1 Background and Approach

As electric vehicles and renewable energy sources gain wide spread adoption, the low capacity and power of batteries represent a key bottleneck to wide spread adoption.[1] Lithium ion batteries (LIBs) and lithium metal polymer batteries (LMPBs) are the most advanced energy storage technology to-date[2,3], but the combined requirements of energy density, power density, cost, and safety for real applications has not been achieved (

Table **5-1**). While there has been great progress made on active materials to achieve higher power and energy densities, these improvements are often made at the expense of cost and safety. Significant improvement towards one of these requirements often compromises the others, and in fact, all high-energy density LIBs suffer from worrying safety records.[4] Safety concerns with these energy dense LIBs can be traced in large part to the growth of dendrites[5], and the flammability of the liquid ion-conducting electrolyte solution[6]. Dendritic deposits penetrate through traditional separators[7] and cause capacity fade, short circuits, overheating, and fires.[8]

Table 5-1 USABC EV Performance Targets

Performance Metric	End of Life Characteristics at 30°C Units Cell Level
Peak Discharge Power Density	1500 W/L, 700 W/kg
Useable Energy Density at C/3 Discharge Rate	750 Wh/L, 350 Wh/kg
Calendar Life	15 Years
DST Cycle Life	1000 Cycles
Selling Price	$100/kWh
Operating Environment	-30 to +52°C
Unassisted Operating at Low Temperature > 70% Useable Energy @ C/3 Discharge	-20°C
Survival Temperature Range, 24 hr	-40 to+ 66°C

The growth of dendrites is also the key roadblock for batteries with lithium metal anodes, which has promise to exceed the current state-of-the-art batteries in terms of capacity, power and weight.[9]As the energy and power densities of batteries increase, separators need to withstand harsh operating conditions (e.g., thermal stability), suppress the growth of dendrites, retain high porosity and strength, and possess minimal thickness.

Aramid nanofiber (ANF) represent a new nanoscale building block that has been shown to have superior strength and thermal stability.[10] The ANF composite with polyethylene oxide (PEO) made using a layer-by-layer technique, as was discussed in Chapter 2, has demonstrated mechanical strength to suppress lithium and copper dendrite growth and thermal stability up to 450°C while having a thickness of 3μm.[11] Although the work demonstrated the potential advantages of ANF as a suitable separator for batteries, it utilized a layer-by-layer technique that is difficult to scale to meet commercial demands in both quantity and quality. In a continuous roll-to-roll production, rolls of separator are typically used on the orders on millions of square meters per month. It is therefore essential to develop a continuous production method for an ANF separator if we hope to make an

impact on the LIB safety and demonstrate its feasibility in batteries larger than coin-type cells.

In this chapter, we explore a simple and scalable fabrication method, doctor blading, to produce ANF separators. Doctor blading, also referred to draw-down coating, is a commonly used method to produce LIB electrode coatings.[12] In addition to scalability, porosity and pore size control in the separator is critical in achieving high power density batteries. We incorporate different metal oxide nanoparticles to gain control over the pore size and porosity of the ANF separators and assess their stability in coin cell cycling experiments. We also present a proof of concept study for a novel separator on anode assembly, where we investigated the interfacial properties between the separator and anode, and its cycling behavior. Finally, we demonstrate the scalability of the doctor blading method with a benchtop prototype capable of producing continuous films of the ANF separator.

5.2 Material and Methods

This section describes the materials and experimental techniques used in this work.

5.2.1 Preparation of ANF Dispersion

ANF dispersions are prepare according to the process described by Ming et al.[10] Dimethyl Sulfoxide (ACS Reagent, 99.9%, Sigma Aldrich) is dried using molecular sieves for at least 24 hours before use. A 2% ANF solution (10 g Kevlar yarn in 500 mL DMSO) is prepared with 10g of KOH. The solution is stirred constantly for approximately 40 days or until all Kevlar yarn is fully dissolved.

5.2.2 Preparation of metal-oxide nanoparticles/ANF Composite Separator

Metal oxides nanoparticles (Al_2O_3, MgO, and TiO_2, SigmaAldrich) are weighed out and added into 2% ANF dispersion per the desire wt%. The mixture is mixed using a Flactek Speedmixer at 1500 rpm for 20 minutes. Spherical yittrium stabilized zirconia grinding bead are added to each mixture to ensure homogenous mixing. After a homogenous mixture is attained, the mixture is doctor bladed onto a clean glass plate at the desired thickness. The sample along with the glass plate is then submerged into a 95% ethanol bath for a 30 minutes' solvent exchange process. The sample is then gently remove from the glass plate and sandwiched between two Teflon sheets and glass plates. The assembly is then dried at 90°C under vacuum for 4 hrs.

5.2.3 Direct coating of the ANF/Al_2O_3 Composite Separators

Single sided carbon anodes coated on copper foil were purchase from MTI Corp. The anodes were cut into 2" x 3" strips and fixed onto a glass plate. The sample is gently smoothed using a piece of Kimwipe. Metal oxide nanoparticle/ANF dispersion is then doctor bladed onto the anode at 150μm. The samples are then submerged in 95% ethanol for 30 minutes and then vacuum dried sandwiched between two Teflon sheets and glass plates.

5.2.4 Coin Cell Assembly and Testing

Single sided lithium nickel manganese cobalt oxide (NMC) cathodes on aluminum foil were purchased from MTI Corp. Cathodes are then punched out with a 9/16 diameter arc hole punch. Similarly, anodes are punched out with a 5/8 diameter arc hole punch. Free-standing separators are punched into 20mm diameter circles. Coin cells are assembled into a CR2032 case in an argon filled glovebox. Special care is taken to make sure the cell

components are aligned and centered. The cells are consistently flooded with approximately 300µL of 1.2M $LiPF_6$ in EC/DMC 1:1 v/v.

Coin cell were tested on a MACCOR series 4000 battery tester. Voltage cutoffs are set to 4.2V and 2.7V. The capacity of the coin cells using the before mentioned electrode dimensions were calculated to be 3mAh per loadings given by MTI Corp. All cells were left to rest at open circuit voltage for at least 5 hours before cycling, then cycled at C/10 for 4 cycles to ensure complete wetting of all cell components and consistent SEI formation on the carbon anode.

5.3 Results

This section describes the results and challenges for the scale up process for ANF separators.

5.3.1 ANF Separator Fabrication and Characterization

ANF separators are fabricated using a simple doctor blading process where a viscous 2% ANF dispersion is spread evenly on a glass plate and then submerged into water bath for a solvent exchange process. Once a ANF hydrogel is formed, the sample is dried under vacuum at 90°C for 4 hours. Compared to the layer-by-layer work described in the Chapter 2, no polyethylene oxide is required since ionic conductivity is provided by lithium salt based carbonate electrolytes in a typical LIB.

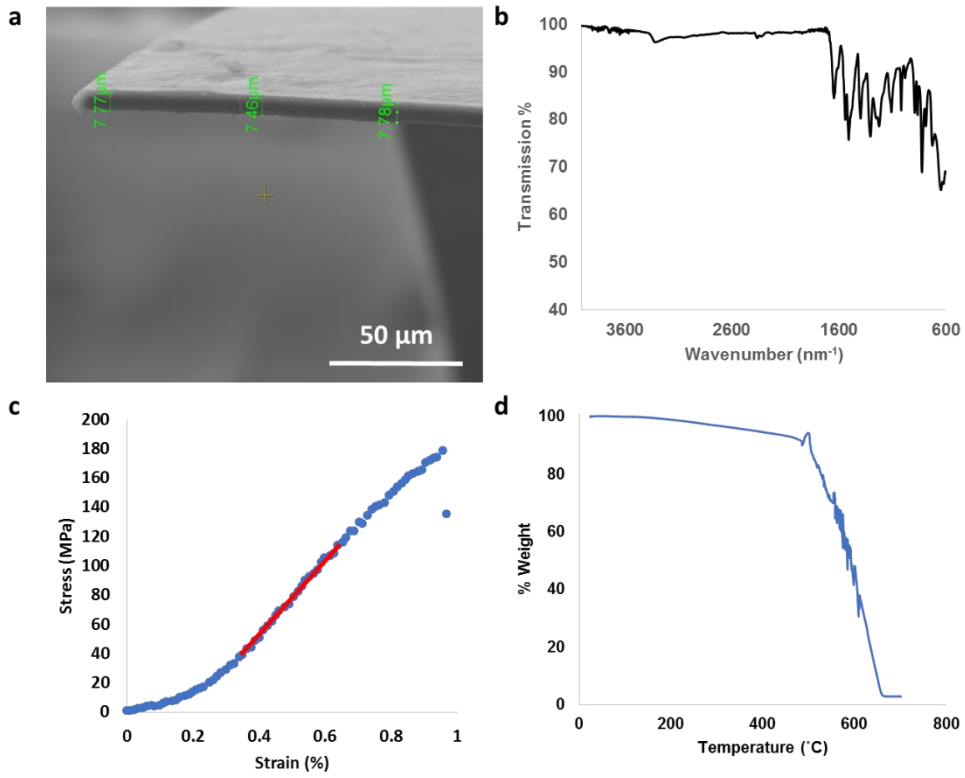

Figure 5-1 (a) Cross-sectional scanning electron micrograph (b) Fouier transformed infrared (FTIR) spectra; (c) Stress-Strain curve; (d) Thermal gravimetric analysis (TGA) of doctor bladed ANF separator

Using the doctor blading process, a uniform free-standing ANF separator is produced (Figure 5-1a). Fourier transformed infrared (FTIR) spectra of the ANF separator match those reported in literature[10] and confirms a complete solvent exchange and drying process since no significant -OH stretching that would suggest residual KOH or water (Figure 5-1b). The sample also exhibited 20 GPa Young's modulus and 180 MPa tensile strength (Figure 5-1c), which is critical for dendrite suppression. The favorable thermal stability observed in Chapter 2's ion conductor work was also retained, with thermal gravimetric analysis (TGA) suggesting thermal stability at about 500°C (Figure 5-1d).

Table 5-2 Gurley Numbers of Various Separators

Sample Material	Gurley Number
Celgard 2500 Single layer PP	200
Celgard 2325 Trilayer PP/PE/PP	600
W-Scope Single Layer	260
Aramid Nanofiber	Too high to measure

As mentioned before, typically the ionic conductivity of separators is provided by a liquid electrolyte. It is therefore important to characterize the pore size and porosity of the ANF separator. Using the Gurley number, which is defined as the time required for 100cm^3 of air to pass through 1in^2 sample area, we can quickly assess the porosity and pore size of a given separator. When compared to commercially available polyolefin separators like Celgard 2500, 2325 and W-Scope, the ANF separator's Gurley number was too high to measure (Table 5-2). This indicates that while the ANF separator possesses ideal mechanical and thermal properties, it lacked the suitable pore size and porosity for a separator. This was confirmed using mercury intrusion porosimetry where the ANF separator exhibited a narrow pore distribution with a peak at 5.8nm (Figure 5-2). The porosity was calculated to be 8.2%. It is this combination of low porosity and small pore size that prompted further investigation into strategies to control pore size and porosity.

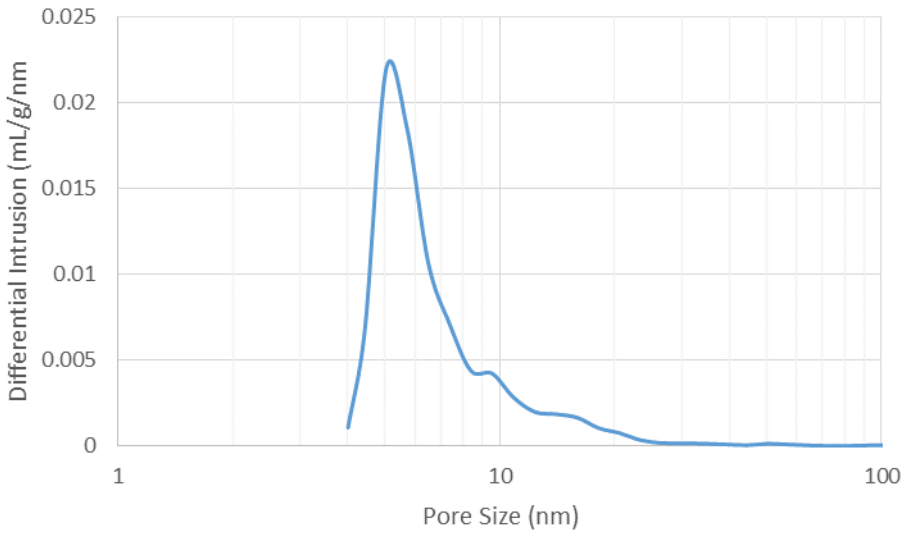

Figure 5-2 Pore size distribution of ANF separator determined by mercury intrusion porosimetry

5.3.2 Porosity control

Upon close examination of surface morphology of the ANF separator, a tightly aligned network of fibers can be observed (Figure 5-3). This is likely due to the hydrogen bonding between the C=O and N-H groups along the polymer chain of nanofibers. Similar tightly aligned structures have also been observed in the fabrication of cellulose fiber based separators[13]. Chun et al. hypothesized that the combination of the capillary forces during drying and tight hydrogen bonding promoted by water lead to the tightly aligned structure and by using a solvent bath with a higher isopropyl alcohol content, the cohesive forces were reduced. Similarly, for ANF separators, when a 95% ethanol bath was used in place of water, we observed an increase in surface pores under SEM (Figure *5-4*a). However, no appreciable improvement was observed when measuring the Gurley number. This indicates that fiber alignment while lowered, remains quite tight and leading to low pore size and porosity.

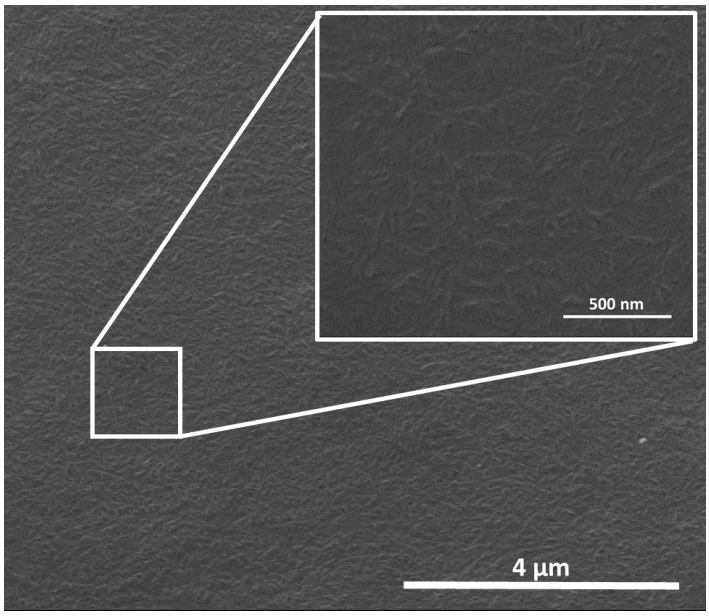

Figure 5-3 Surface SEM of ANF Separator

In order to induce larger pores and higher porosity, we hypothesized that the addition of the spherical metal oxide nanoparticles may disrupt the alignment of the aramid nanofibers during drying and act as "pillars" to prevent the nanofibers from irreversibly hydrogen-bonding. 50 nm aluminum oxide nanoparticles (Sigma Aldrich) were used as the model nanoparticle to test this hypothesis. Different amounts of Al_2O_3 nanoparticles were mixed into a 2% ANF dispersion using a high energy Flactek planetary mixer. We observed approximately an order of magnitude decrease in Gurley number for a 10wt% increase in Al_2O_3 (Figure *5-4*d). The Gurley number reaches a plateau at 750 at 70wt% Al_2O_3. Further increases in Al_2O_3 wt% yields a heterogeneous mixture, likely due ANF and Al_2O_3 phase separation. The observations of a critical weight fraction leading to phase separation has been similarly reported in mixtures of different shaped nanoparticles.[14]

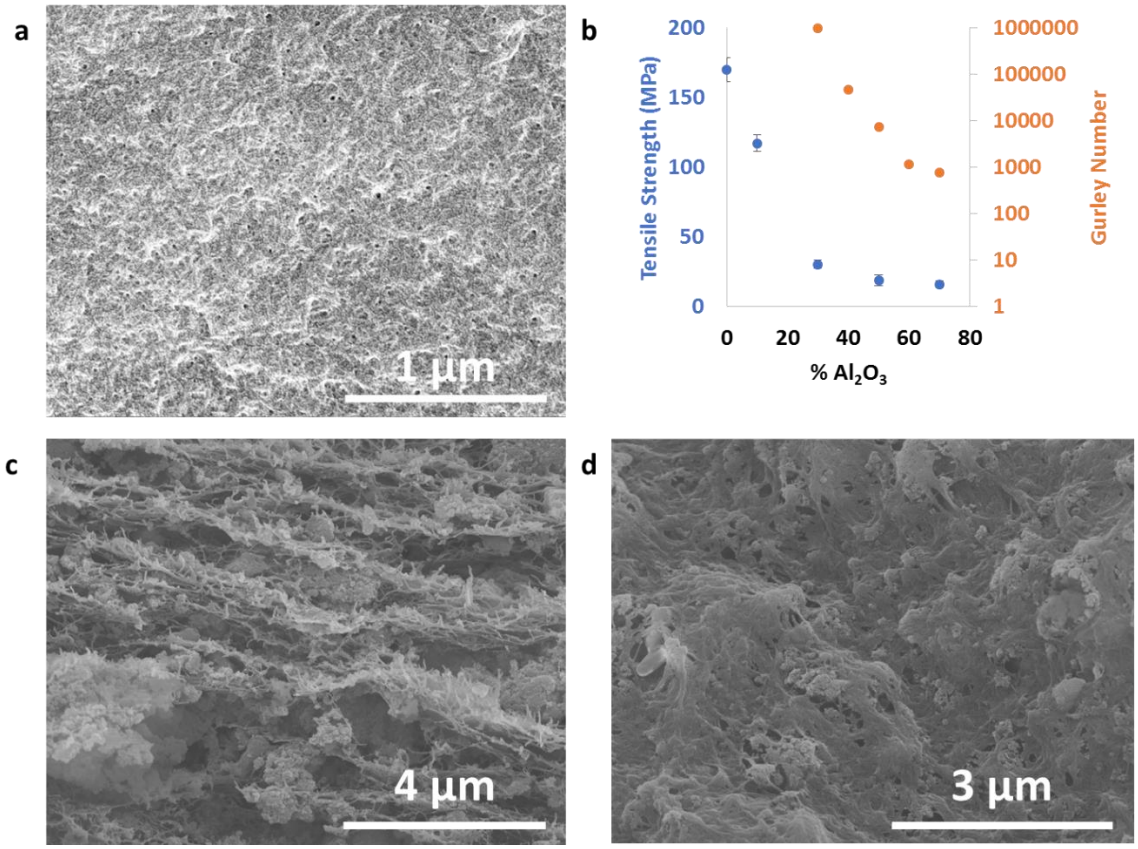

Figure 5-4 (a) Surface SEM of an ANF Separator made using an ethanol bath; (b) Gurley number and tensile strength relationship with %Al_2O_3 (c) Cross-sectional and (d) surface SEM of ANF Separator with 70% Al_2O_3

SEM images of the cross-section (Figure *5-4*c) and surface (Figure *5-4*d) of the 70wt% Al_2O_3 ANF separator show that Al_2O_3 nanoparticles are homogenously incorporated in the sample. Some stratification is observed and is an indication of minor phase separation. More importantly, many pores are observed on the surface and a porous structure is visible throughout the cross-section of the sample. MIP analysis shows an overall increase in the porosity from 8.2 to 75%. A bi-modal pore size distribution was also observed with an average pore size of 54 nm (Figure *5-5*).

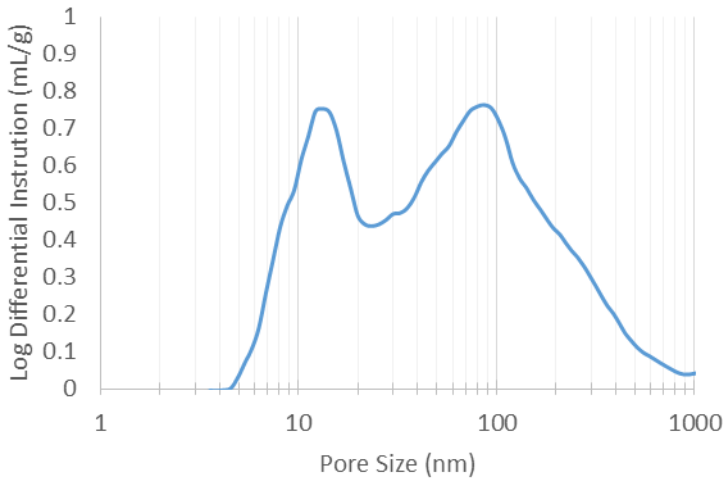

Figure 5-5 Pore Size Distribution of ANF Separator with 70% Al_2O_3 determined using mercury intrusion porosimetery

5.3.3 Metal Oxide Nanoparticle Down-selection

Additionally, magnesium oxide and titanium oxide nanoparticles were also investigated for their use in the ANF/nanoparticle composite separator. Their performance were compared to that of the commercially available Celgard 2500 and Al_2O_3/ANF composite separator. All ANF separators used incorporated a consistent 70 wt% metal oxide nanoparticle verified using TGA. The samples were assembled into a $LiCoO_2$/Li half-cell and cycled at C/2 for 50 cycles to assess the separators long term stability. In Figure *5-6*, we can observe that both TiO_2 and MgO containing samples exhibited capacity fade, with TiO_2 samples fading as early as cycle 4. This is most likely caused by the reduction of TiO_2 to $LiTiO_4$ and consequent consumption of Li^+ ions from the electrolyte.[15,16] For MgO samples, where similar oxidation changes to Mg is unlikely[17], dissolution of Mg^{2+} and alloying and/or plating of Mg metal with Li metal could potentially explain the delayed failure observed during cycling.[18] On the other hand, a stable cycling behavior is observed for Al_2O_3 samples where the capacity retention is similar to that of Celgard 2500. In

conclusion, Al_2O_3 remains the most suitable metal oxide for the ANF composite separator and will be used in subsequent studies.

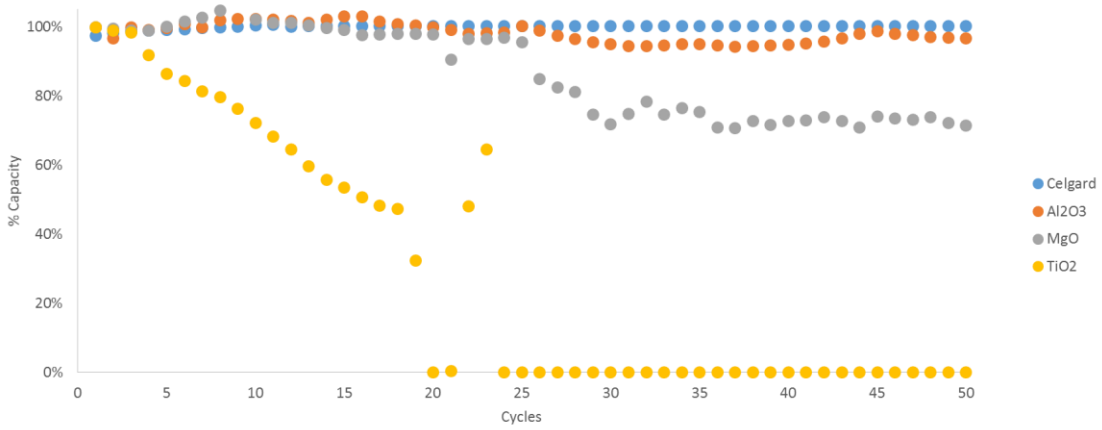

Figure 5-6 Capacity retention as a function of cycle for various ANF Separators with Al_2O_3, TiO_2 and MgO compared to Celgard 2500. Coin cells made up of $LiCoO_2$ cathode, lithium metal anode and 1M $LiPF_6$ in EC/DMC 1:1 v/v. Cycled at C/2.

5.3.4 Separator Coating on Carbon Anodes

While the addition of the metal oxide nanoparticles enabled us to enlarge the pore size and increase porosity, it presented an additional challenge in decrease tensile strength. For ANF separators to be incorporated in multi-layer pouch cells or cylindrical cell, sufficient tensile strength is required such that the separator can withstand the stresses of winding and z-folding processes commonly seen in cell assembly. However, with the addition of metal oxide nanoparticles and approaching usable Gurley number, the tensile strength of ANF separator decreased drastically from 170 MPa to 16 MPa (Figure *5-4*b). At such a lowered tensile strength, we devised that a separator directly applied on the carbon anode would not be required to bear the stress and tension that is applied to a conventional free-standing separator. Additionally, such a separator/anode assembly could potentially simplify the assembly process by reducing the number of components from three to two.

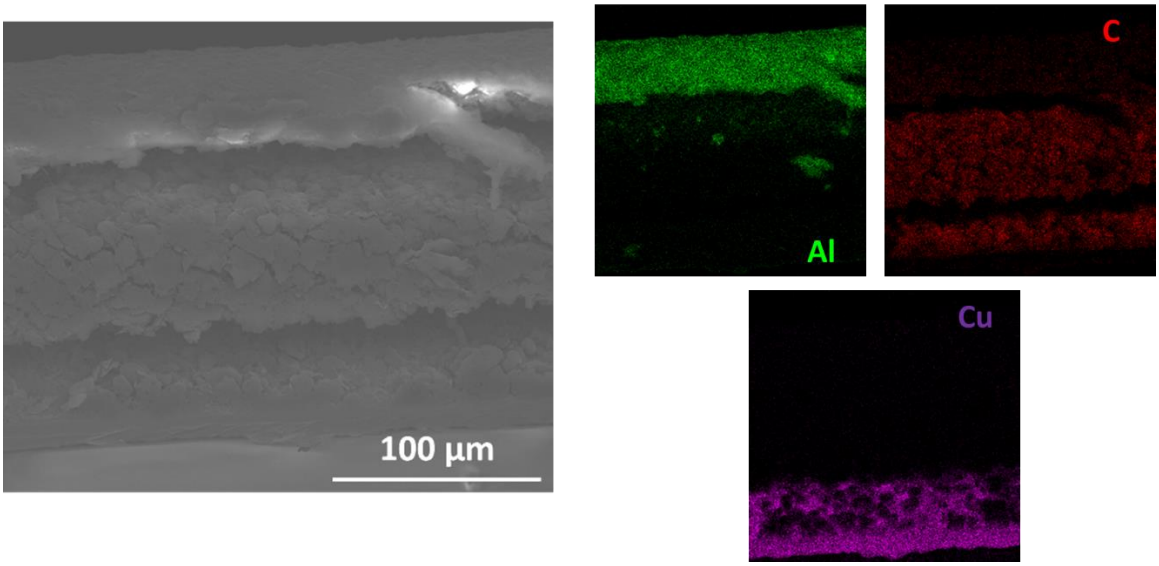

Figure 5-7 (left) SEM of carbon anode coated with 70% Al_2O_3 ANF separator; (right) EDAX elemental mapping of SEM image on the right.

To confirm the direct coating concept, the 70% Al_2O_3/ANF composite separator is coated onto a carbon separator using a doctor blading process. SEM imaging of the coated separator shows an identical morphology as the free-standing samples (Figure 5-7). EDAX elemental mapping of the cross section of coated anode shows a clear demarcation between the copper current collector, carbon anode and Al_2O_3/ANF separator (Figure 5-7). The Al_2O_3/ANF coated anode, an identical free-standing Al_2O_3/ANF sample and Celgard 2500 are then assembled into CR2032 cells to compare their rate performance. The cells are cycled at different C-rates from C/10, C/5, 1C, C/2, 2C to 3C (Figure *5-8*). All three cells showed stable cycling and similar capacity retention after high C-rate cycling. However, when comparing the cycling performance at 1C, 2C and 3C, the cell with the separator coated anode retained the highest capacity especially at 2C and 3C. This illustrates that the separator coated anode concept would not only simplify the assembly process but also increases the performance of the cell.

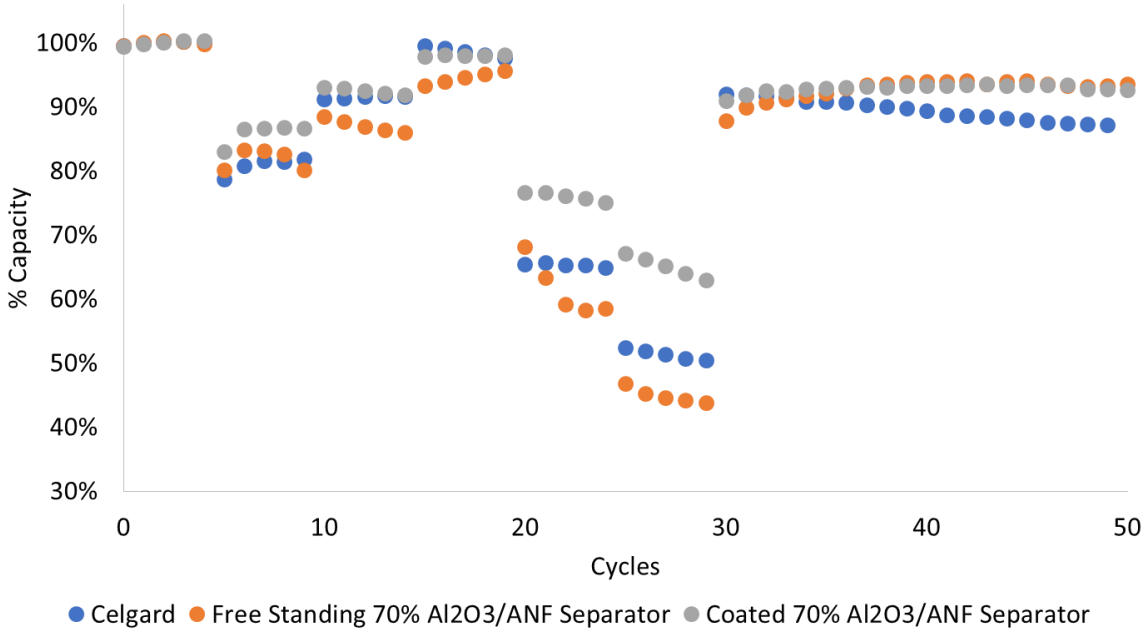

Figure 5-8 Capacity retention as a function of cycle number for Celgard 2500, free-standing Al_2O_3/ANF separator and coated Al_2O_3/ANF separator; comparing performance.

To further understand the increased performance for the separator-coated anodes, we performed electrochemical impedance spectroscopy (EIS) on CR2032 coin cells with the separator-coated anode and an identical cell but with a free-standing separator of the same composition. The EIS spectra plotted in the form of Nyquist plots reveal both a decreased solution resistance and charge transfer resistance for separator coated anode case (Figure *5-9*). This is because an improved interface between the separator and anode is obtained when the separator is coated onto the anode rather than simply placed onto the anode. The reduced contact resistance in the coated separator likely contributes to the decreased solution resistance while more uniform electrolyte wetting throughout the separator and anode reduces the charge transfer resistance.

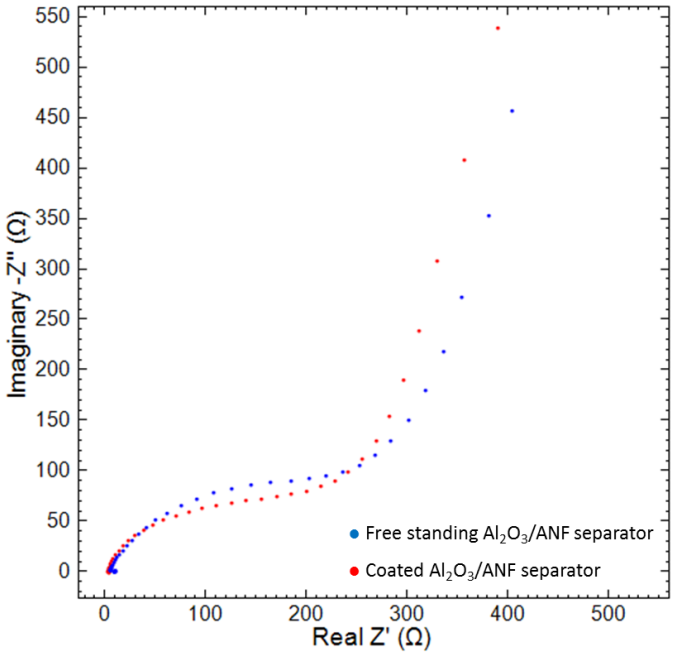

Figure 5-9 Nyquist plot comparing the interfacial properties of free-standing and coated Al_2O_3/ANF separator.

5.3.5 Scale-up Demonstration

To demonstrate the scalability of the doctor blading process and hence the ANF separator production process, a continuous conveyor belt driven prototype system was designed and built. The prototype consisted of 3 separate stages: (1) syringe pump driven ANF dispenser with a doctor blade attached to evenly coat the conveyor belt with ANF; (2) solvent exchange bath filled with water and extra shower heads to promote fast solvent exchange; (3) height adjustable parallel heating plates for sample compression and drying (Figure *5-10*a). All of the parts were designed using CAD and machined using the different machining facilities on campus. Corrosion resistant stainless steel (rollers, brackets) was selected for all parts in contact with solvent exchange bath while aluminum was used for all the other parts.

For the ANF dispensing stage, a special die attachment was designed to widen the dispensing path of typical syringes. The die was a three-part design with a top plate, bottom plate and syringe adapter ring (Figure *5-10*b). A reservoir with a 'coat-hanger' geometry, similar to that seen in slot die coaters, was designed into a top plate to ensure smooth delivery of the ANF dispersion. The overall slit has 2 inches width and a 0.1mm opening. This part was manufactured using 3D printing of stainless steel (Figure *5-10*c). The ANF dispersion was then dispensed onto the Teflon coated conveyor belt and passed under a doctor blade to further control the thickness of the separator produced.

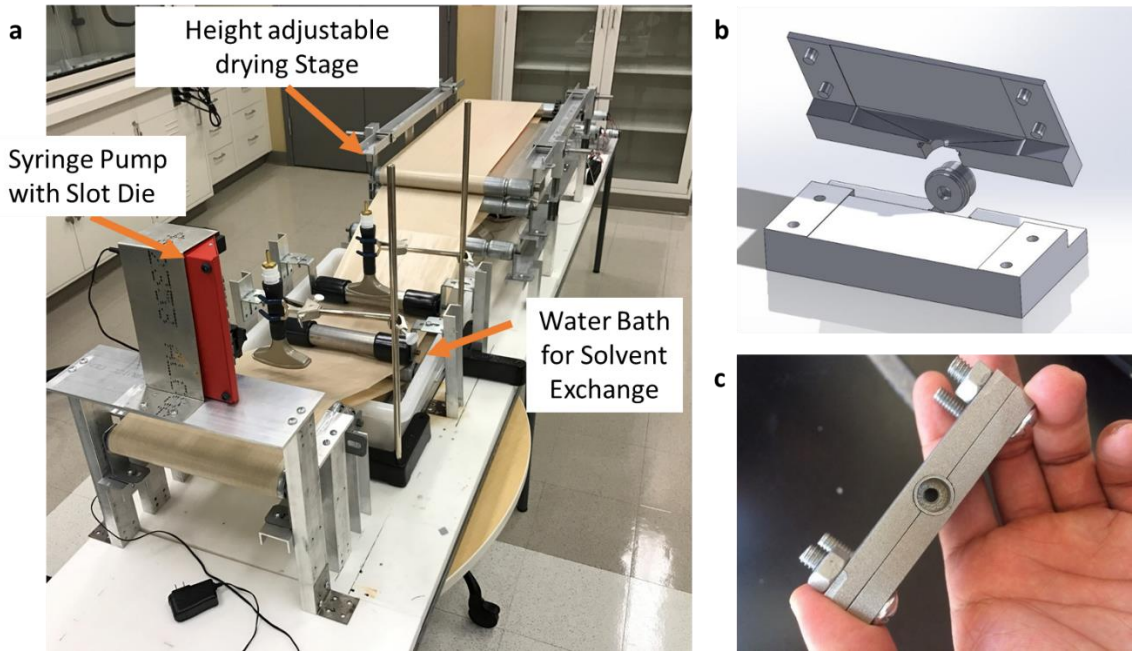

Figure 5-10 (a) Image of the assembled scale-up prototype; (b) CAD of die attachment; (c) Image of the 3D printed die attachment.

After a smooth layer of ANF was formed, the conveyor belt was passed through a water trough for the solvent exchange process. During this solvent exchange process, the KOH and DMSO were washed out and an ANF hydrogel was formed. The corrosive nature of KOH in water was taken into consideration as all parts in contact with the water trough

was made of corrosion resistant stainless steel. The length of the water trough was designed to provide approximately 8-12 minutes of residence time, which was experimentally determined to be sufficient for complete solvent exchange. The hydrogel was dried through the drying stage with parallel heated plate. Temperature controlled heat pad were attached to aluminum plates to form the heated area. The separation distance between the plates are adjusted to 4 micrometer heads. With trial and error, the optimized operating conditions (Table 5-3) are identified for the machine to produce a 2-meter-long, 4 inches wide continuous ANF film.

Table 5-3 Optimal operating conditions for the scale-up prototype

Operating Condition	Value
Conveyor Belt Speed	15 cm/min
Syringe Belt Speed	0.6 mL/min
Doctor blade height	380 µm
Heater Temperature	235˚F

The length of the ANF separator was limited to the amount of the ANF dispersion that can be stored in the syringe. Under the current syringe pump, only a 60mL syringe can be used, which limits the overall length of ANF film to be 2 m. Nevertheless, this prototype serves as a proof of concept in producing a continuous ANF film suitable for a separator application. We can also envision the replacement of the conveyor belt with a roll of carbon anode to perform a continuous coating of the separator onto the anode.

5.4 Conclusions

In conclusion, we fabricated an ANF separator using the doctor blade method. The sample retained the high mechanical strength and thermal stability from the work on the ANF/PEO

ion-conducting composite. However, the low pore size and porosity of the neat ANF separator made it impossible to use in high power battery applications. Metal oxide nanoparticles, along with a switch from water to an ethanol solvent exchange bath, disrupted the hydrogen bonding between the aramid nanofibers to produce a highly porous composite separator. Unfortunately, the gain in the porosity and higher rate cyclability came at a cost of mechanical strength. The lack of mechanical strength in the composite ANF separator inspired the idea of a separator directly coated on an anode assembly. When the separator was directly coated onto the carbon anode, we observed both a decrease in solution resistance and charge transfer resistance. This enabled rate performances that exceed that of commercial Celgard products. Finally, a bench top prototype was designed and successfully built to demonstrate a continuous production of a 2 meter long continuous ANF separator.

References

1. Dunn, B., Kamath, H. & Tarascon, J. M. Electrical energy storage for the grid: a battery of choices. *Science* **334,** 928–35 (2011).
2. Serrano, E., Rus, G. & García-Martínez, J. Nanotechnology for sustainable energy. *Renewable and Sustainable Energy Reviews* **13,** 2373–2384 (2009).
3. Lodhi, M. A. K. Photovoltaics and hydrogen: Future energy options. *Energy Conversion and Management* **38,** 1881–1893 (1997).
4. Daniel, C. Materials and processing for lithium-ion batteries. *JOM* **60,** 43–48 (2008).
5. Armand, M. & Tarascon, J. M. Building better batteries. *Nature* **451,** 652–657 (2008).
6. Wang, Q. *et al.* Thermal runaway caused fire and explosion of lithium ion battery. *Journal of Power Sources* **208,** 210–224 (2012).
7. Brissot, C., Rosso, M., Chazalviel, J.-N. & Lascaud, S. Dendritic growth mechanisms in lithium/polymer cells. *Journal of Power Sources* **81–82,** 925–929 (1999).
8. Adam Heller. The GS Yuasa-Boeing 787 Li-ion battery: test it at a low temperature and keep it warm in flight. *The Electrochemical Society Interface* 1 (2013).
9. Tarascon, J. M. & Armand, M. Issues and challenges facing rechargeable lithium batteries. *Nature* **414,** 359–367 (2001).
10. Yang, M. *et al.* Dispersions of Aramid Nanofibers : A New Nanoscale Building Block. *ACS Nano* 6945–6954 (2011).
11. Tung, S. O., Ho, S., Yang, M., Zhang, R. & Kotov, N. A. A dendrite-suppressing

composite ion conductor from aramid nanofibres. *Nature Communications* **6,** 6152 (2015).

12. Marks, T., Trussler, S., Smith, A. J., Xiong, D. & Dahn, J. R. A Guide to Li-Ion Coin-Cell Electrode Making for Academic Researchers. *Journal of The Electrochemical Society* **158,** A51 (2011).
13. Chun, S.J. *et al.* Eco-friendly cellulose nanofiber paper-derived separator membranes featuring tunable nanoporous network channels for lithium-ion batteries. *Journal of Materials Chemistry* **22,** 16618 (2012).
14. Jana, N. R. Shape Effect in Nanoparticle Self-Assembly. *Angewandte Chemie International Edition* **43,** 1536–1540 (2004).
15. Knauth, P. Inorganic solid Li ion conductors: An overview. *Solid State Ionics* **180,** 911–916 (2009).
16. Minami, T., Hayashi, A. & Tatsumisago, M. Recent progress of glass and glass-ceramics as solid electrolytes for lithium secondary batteries. *Solid State Ionics* **177,** 2715–2720 (2006).
17. Li, C. *et al.* Cathode materials modified by surface coating for lithium ion batteries. *Electrochimica Acta* **51,** 3872–3883 (2006).
18. Dey, A. N. Electrochemical Alloying of Lithium in Organic Electrolytes. *Journal of The Electrochemical Society* **118,** 1547 (1971).

Chapter 6

Conclusion

6.1 Summary and Overall Conclusions

The goal of the research in this dissertation was to investigate the potential of aramid nanofibers in energy storage applications and to develop design strategies to address challenges in battery separator/membrane engineering. Separator challenges in lithium ion batteries and non-aqueous redox flow batteries were identified and addressed using the various properties of aramid nanofiber based composites. Furthermore, pillaring layered oxide cathodes, with vanadium oxide as a proof of concept, was also presented as potential strategy to improve energy and power density in lithium ion batteries.

Dendrite growth has plagued the safety of the lithium ion batteries and the presented a significant roadblock to higher energy density lithium metal electrodes. While solid ceramic electrolytes that have identified as potential solution due its ultra-high modulus, they lacked the flexibility need to be integrated in existing roll-to-roll assembly lines. A PEO/ANF based solid ion-conducting composite was fabricated using layer-by-layer technique to address these challenges. The results composite $(PEO/ANF)_n$ with n=30-50, demonstrated a Young's modulus of 5 GPa and the ability to suppress hard copper dendrites and softer lithium dendrites. The layer-by-layer approach enabled hydrogen bonding between ANF and PEO which suppressed the crystallization of PEO, a long-time challenge for PEO based electrolytes. The amorphous PEO/ANF composite therefore

exhibited an ionic conductivity as high as 1.7 x 10^{-4} S/cm and was assembled into practical $LiCoO_2$/Li metal coin cell with minimal fade observed over 50 cycles. Along with thermal stabilities up to 450°C, the combination of flexibility, high ionic conductivity, and dendrite suppression capabilities in $(PEO/ANF)_n$ is difficult to achieve in other classes of materials and thereby providing a new approach to engineering solid ion conductors.

In the development of the non-aqueous redox flow batteries, the lack of suitable ion conducting membranes is significant yet often overlooked challenge. Active material crossover through the membranes allows for unwanted active material degradation and is therefore detrimental to the efficiency and longevity of these batteries. Nanoporous ANF based separators was fabricated using a spin assisted layer-by-layer method and was demonstrated as a size selective separator for reducing active material crossover. Compared to microporous Celgard 2325 separators and anion exchange membrane in Neosepta, the ANF separator presented an attractive combination of low permeability (10x lower than Celgard) and high ionic conductivity (10x higher than Neosepta). Modification studies using PDDA and PSS revealed that surface coatings of merely a few layers of PDDA and PSS could reduce permeability by two orders magnitude compared to neat ANF with minimal impact on ionic conductivity. Flow cells with the optimized (PDDA/PSS)5 on ANF separator operated for 100 hours with minimal capacity fade and consistent coulombic efficiencies at 95%. The seemingly contradicting ability to combine low active material permeability and high ionic conductivity, along with outstanding stability in real flow cell environments, demonstrated the potential of aramid nanofiber based separators and provided technological advancement toward more efficient and stable non-aqueous redox flow batteries.

While aramid nanofiber based separators for both lithium ion batteries and redox flow batteries have shown significant promise, manufacturability will ultimately dictate its impact on the industrial scale. A scale up study on using a doctor blading technique was presented to address this challenge. The relationship between porosity, tensile strength in ANF separators, along with its impact on cell performance was investigated. The significant sacrifice in tensile strength needed to achieve high porosity and therefore cell performance called for a separator coating on anode strategy. With the separator directly coated onto a carbon anode, both solution resistance and charge transfer resistance was reduced likely due to a lowered contact resistance and more continuous pore structures between the anode and separator. This resulted an appreciable enhancement in rate capability demonstrated using coin cells. Finally, a prototype machine was designed and the assembled to demonstrate a scaled-up continuous production of the ANF separators. Overall, this work presented a glimpse of what an industrial scale production of ANF separators might look like and a novel separator on anode approach that could increase the power densities of future lithium ion batteries.

Despite a major focus on battery separators, pillaring layered oxide cathode materials was also presented in this dissertation as an approach to increase lithium ion battery energy and power densities. Pillaring agents such as the aluminum keggin ions used, would provide additional structural support thereby increasing cycle life, and the increased layer spacing in the layered oxides would allow for more facile transport of Li ions during intercalation and therefore enhancing rate capability. Vanadium oxide xerogel cathode materials were synthesized and pillared with aluminium keggin ions as initial proof of concept. XRD and TEM was used to confirm a change in layer spacing of 2-3Å while thermal treatments were

used to remove excess water from the structure. In the end, a successful proof of concept was achieve when the pillared V2O5 xerogel treated at 350°C exhibited higher rate capability and cycle life than of the unpillared material.

6.2 Future Work

Lithium ion batteries and redox flow batteries represent two of the most promising energy storage technologies at vastly different stages of development. Lithium ion batteries have been commercially available since 1990s while redox flow batteries, especially non-aqueous system have only recently begun development with all its designs and materials in flux. Aramid nanofibers have shown considerable promise for both applications and should be pursued in the future. Several future directions are proposed in the section below.

6.2.1 Fiber diameter and pore size relationship

Dendrite suppression in LIBs and crossover reduction in NRFBs relied on pore sizes smaller than the dendrite growth areas and molecular sizes of the active material, respectively. Therefore, the ability to the tune pore sizes will be crucial for the development of ANF separators and should be considered as a high priority future work.

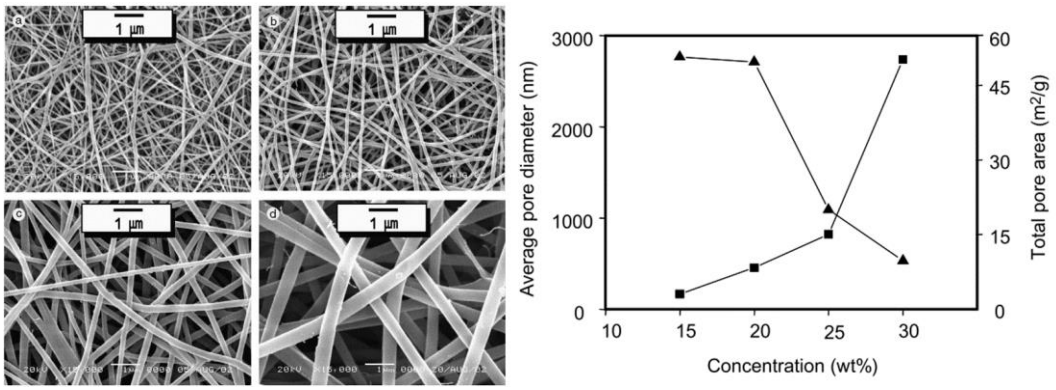

Figure 6-1 Scanning electron micrographs of electrospun nylon 6 nonwoven mats as a function of concentration. Solution concentration were (a)15, (b)20, (c)25, and (d)25 wt.%. (Right) Average pore

diameter and total pore areas of electrospun nylon 6 nonwoven mats as a function of polymer concentration. [1]

Prior research on electrospun fibers have shown that fiber diameters is an important metric in determining the transport properties of the mats formed.[2,3] In Figure 6-1, the pore size and pore areas were compared between nylon 6 fibers of different diameters. While no distinct correlation was drawn between fiber diameter and mat pore size, it can be concluded that pore size is influenced by fiber diameter. A similar phenomenon could be expected for aramid nanofibers and mats.

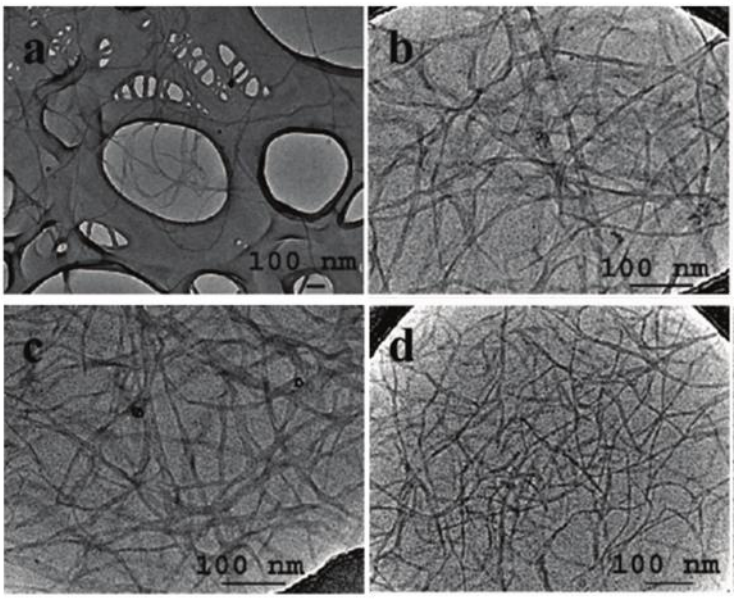

Figure 6-2 Transmission electron micrograph of ANFs in DMSO solutions with different water to DMSO volume ratios: (a) 0, (b) 1/200, (c) 1/100, (d) 1/40.[4]

In the original work by Ming et al describing the synthesis of aramid nanofibers[4], fiber diameter was shown to be a function of water content in the DMSO (Figure 6-2). These results can serve as starting point for controlling the nanofiber diameters and investigating its relationship to pore sizes. Immediate impact can be envisioned in the field all-organic

non-aqueous redox flow batteries, where the use of smaller organic molecules has become increasingly popular.

6.2.2 Dendrite suppression and polysulfide blocking in Li-S batteries

Lithium sulfur batteries have been heavily investigated as the replacement for the current lithium ion batteries due its superior capacity and low cost sulfur materials.[5,6] However, dendrite growth and the polysulfide crossover have emerged as two of the major roadblock to success.[7,8] Similar to RFBs, there are a limited choice of the suitable membranes with polysulfide blocking abilities for Li-S batteries. Membranes with pore sizes similar to that of polysulfide have been proposed and investigated, such as those made with polymer with intrinsic porosity.[9] Based on the dendrites suppressing and crossover reduction that this dissertation have described, ANF separators emerges as a logical choice for Li-S batteries with proven abilities address both challenges.

Table 6-1 Summary of conductivity and polysulfide permeability of Celgard 2325, ANF and PIM-1.

	Conductivity (mS/cm)	Permeability ($x10^{-7}cm^2/s$)
Celgard 2325	0.4	788
ANF	0.1	7.02
PIM-1	0.1<x<0.2 (from published graph)	2.39

Preliminary polysulfide blocking experiments have been conducted in a H-type cell with constant stirring. ANF separators made using the same method as that described for RFBs in chapter 3 were used and compared with Celgard 2325 and PIM-1 from ref. 9 (Table 6-1). ANF showed two orders of magnitude decrease in the lithium polysulfide permeability compared to Celgard 2325. When compared to PIM-1, the ANF had a 3x higher permeability while retaining similar conductivity. Improvements to ANF can be expected with further optimization. These permeability results along with its dendrite suppressing

capabilities, ANF seems to be a unique and promising material for Li-S batteries and should be further investigated.

6.2.3 Tailored surface modifications for active materials in RFBs

The surface modification method was successfully demonstrated in a $V(acac)_3$ based flow cell, in which it increased coulombic efficiency and cycle life. While $V(acac)_3$ is a promising active material for RFBs, it is unlikely that it will be used in commercial NRFBs due to its limited cycle life and sensitivity to oxygen. As new classes of active materials for NRFBs continue to emerge, $(PDDA/PSS)_n$ coatings on ANF may even induce undesirable interactions. It is therefore important to understand the interfacial effects on the stability of active materials and tailor the separator surface modifications. Anti-fouling surface modification on nanofiltration filters[10,11] can potentially serve as inspiration to the development of these coatings. Furthermore, these modification strategies can be extended to electrode and other component surfaces to further enhance the stability of future flow cells.

References

1. Ryu, Y. J., Kim, H. Y., Lee, K. H., Park, H. C. & Lee, D. R. Transport properties of electrospun nylon 6 nonwoven mats. *European Polymer Journal* **39,** 1883–1889 (2003).
2. Gibson, P. W., Schreuder-Gibson, H. L. & Rivin, D. Electrospun fiber mats: Transport properties. *AIChE Journal* **45,** 190–195 (1999).
3. Huang, Z.-M., Zhang, Y.-Z., Kotaki, M. & Ramakrishna, S. A review on polymer nanofibers by electrospinning and their applications in nanocomposites. *Composites Science and Technology* **63,** 2223–2253 (2003).
4. Yang, M. *et al.* Dispersions of Aramid Nanofibers : A New Nanoscale Building Block. *ACS Nano* 6945–6954 (2011).
5. Bruce, P. G., Freunberger, S. A., Hardwick, L. J. & Tarascon, J.-M. Li–O2 and Li–S batteries with high energy storage. *Nature Materials* **11,** 19–29 (2011).
6. Nazar, L. F., Cuisinier, M. & Pang, Q. Lithium-sulfur batteries. *MRS Bulletin* **39,** 436–442 (2014).
7. Manthiram, A., Fu, Y. & Su, Y.-S. Challenges and prospects of lithium-sulfur batteries. *Accounts of chemical research* **46,** 1125–34 (2013).
8. Zhang, S. S. Liquid electrolyte lithium/sulfur battery: Fundamental chemistry, problems, and solutions. *Journal of Power Sources* **231,** 153–162 (2013).
9. Li, C. *et al.* Polysulfide-Blocking Microporous Polymer Membrane Tailored for Hybrid Li-Sulfur Flow Batteries. *Nano letters* **15,** 5724–5729 (2015).
10. Ng, L. Y., Mohammad, A. W. & Ng, C. Y. A review on nanofiltration membrane fabrication and modification using polyelectrolytes: Effective ways to develop

membrane selective barriers and rejection capability. *Advances in Colloid and Interface Science* **197–198,** 85–107 (2013).

11. Wang, X. L., Shang, W. J., Wang, D. X., Wu, L. & Tu, C. H. Characterization and applications of nanofiltration membranes: State of the art. *Desalination* **236,** 316–326 (2009).